High-resolution Imaging and Spectroscopy of Surface and Interface Structures in Solid-state Li-ion Battery Materials



Ruomu Zhang

Corpus Christi College

University of Oxford

A thesis submitted for the degree of
Doctor of Philosophy
Hilary 2024

Supervised by Prof. Peter D. Nellist
Prof. Sir. Peter G. Bruce

Abstract

Solid-state lithium-ion battery (SSLIB) is a promising candidate for the next generation of energy storage system due to their enhanced safety and higher energy density, However, the primary challenge for its commercialisation lies in ensuring a stable and low-resistance interface between the active materials and solid electrolyte. Scanning transmission electron microscopy (STEM) is the ideal tool for probing the interface problem, by delivering structural, compositional, and electronic structural information at high spatial resolution. However, its application is largely restricted by the challenges associated with preserving the highly air- and beam-sensitive characteristics of SSLIB materials to study their near-natural state.

This thesis investigates the interfacial redox reactions between cathode $Li(Ni_{0.6}Co_{0.2}Mn_{0.2})O_2$ (NMC622) and solid electrolyte Li_6PS_5Cl (LPSCl), using STEM techniques.

Firstly, an anaerobic sample transfer protocol is developed, with its efficacy demonstrated through studies on the air exposure effects on the morphology and chemistry of LPSCl. The electron beam damage of LPSCl is also explored.

Secondly, a workflow for preparing NMC622/LPSCl interface lamellae using cryogenic-plasma focused ion beam (cryo-PFIB) is established, effectively minimising ion beam-induced structural degradation to 2nm on NMC622, while successfully preserving the charged state of NMC622 against ion and electron beam damage.

Thirdly, electron energy loss spectroscopy (EELS) data acquisition and quantification methodologies are developed for valence state analysis in these beam-sensitive battery materials, allowing for precise measurements of the interfacial redox reaction layer.

Finally, the interfacial redox reactions between NMC622/LPSCl are systematically studied from the spontaneous redox reaction to electrochemical and chemical reaction at different states of charge. The reduction layer on NMC622 surface can extend up to 110nm when charged to 4.8V. By comparing to conventional liquid electrolyte, the significant penetration of the reduction layer on NMC622 induced by LPSCl is attributed to the O migration from cathode towards solid electrolyte.

Declaration of Originality

I, Ruomu Zhang, declare that this thesis is my own work and has not been submitted to another institution for any other degree or qualification. All contributions from collaborators have been appropriately referenced throughout the work.

Dedicated to my parents

who give me life and strength

Acknowledgements

I would first like to express my deepest gratitude to my supervisors, Peter Nellist and Peter Bruce, for their consistent mentoring and advice during my DPhil studies. The opportunity to work under such knowledgeable and dedicated scientific leaders has been a real privilege.

I would like to thank fellow members (past and present) of both research groups, the DCCEM facility staff and the ePSIC staff at Diamond Light Source for their help and support. In particular, I would like to thank Rebecca Nicholls and Sergio Lozano-Perez for the inspirational discussions of spectroscopy study. My thanks also go to Dr. Alex Sheader, Dr. Tianyi Chen, Dr. James Sode, Dr. Zezhong Zhang, Dr. Emanuela Liberti, Dr. Weixin Song, Dr. Ali Mostard, Dr. Longlong Wang, Zhiyuan Ding, Lechen Yang for their teaching and help on microscopes and batteries. I would like to thank Max Schart, Yvonne Chart, Tahmid Choudhury, Alex Zanre, Dr. Chen Huang for their helpful discussion on this thesis. Special thanks go to Joanne Etheridge, who led me into the field of electron microscopy and supported my dream in broadening horizon and pursuing further education.

To my friends Max Schart, Giulia Galatolo, Xinyue Zhao, Houzhi Liu, Yiming Zhang, Siyuan Liu, Qile Li, Jing Hou, Shobhan Dhir, Lijin An, thank you for the constant encouragement and accompany. All the laughs and tears we shared together has made my life complete.

To my parents, Lixin Zhang and Lingjiang Ouyang, thank you for your unwavering love and support through this long journey. Words fail to describe how lucky and proud I am to be your daughter.

List of Contributions from Collaborators

1. Dr. Emanuela Liberti has contributed to the energy dispersive spectroscopy and 300kV diffraction pattern data acquisition on Li_6PS_5Cl.
2. Dr. Weixin Song has contributed to the energy dispersive spectroscopy data acquisition on Li_6PS_5Cl.
3. Dr. Alex Sheader has contributed to the early stage of plasma focused ion beam H pattern milling of $Li(Ni_{0.6}Co_{0.2}Mn_{0.2})O_2$ / Li_6PS_5Cl interface.
4. Dr. Longlong Wang and Lechen Yang have contributed to solid-state battery cycling.
5. Lijin An has contributed to liquid-state battery cycling.

List of Publications

1. Zhang, R., *et al.* Anaerobic-transfer cryo-PFIB TEM lamellae workflow for solid-state battery materials. *In submission to Microscopy and Microanalysis.*
2. Zhang, R., *et al.* STEM-EELS Characterisation of Depth Dependant Interfacial Reaction between Solid-state Electrolyte and Cathode. *In submission to Nature communications.*
3. Zhang, R., *et al.* Interpretation of L edge postpeak in Ni metal and oxide. *In submission to Ultramicroscopy.*
4. Schart, M., *et al.* Non-aqueous synthesis of low-vacancy chromium hexacyanochromate. *In submission to Journal of The American Chemical Society.*
5. An, Li., *et al.* Distinguishing Bulk Redox from Near-Surface Degradation in Lithium Nickel Oxide Cathodes. *In submission to Energy & Environmental Science.*

Glossary

ABF	Annular bright field
BF	Bright-field
CEI	Cathode electrolyte interphase
COM	Centre of mass
CCD	Charge coupled device
CMOS	Complementary metal oxide semiconductor
CTEM	Conventional transmission electron microscopy
CBED	Convergent beam electron diffraction
Cryo-PFIB	Cryogenic-plasma focused ion beam
DF	Dark-field
DFT	Density functional theory
DPC	Differential phase contrast
dDPC	Differentiated differential phase contrast
DMC	Dimethyl carbonate
DED	Direct electron detector
EBSD	Electron backscatter diffraction
EDS	Energy dispersive spectroscopy
ELNES	Energy loss near-edge structure
EELS	Electron energy loss spectroscopy
EC	Ethylene carbonate
EV	Electric vehicle
EXELFS	Extended energy loss fine structure
ePIE	Extended ptychographic iteration engine
EXAFS	Extended X-ray absorption fine structure
FEG	Field Emission Gun
FIB	Focused ion beam
GIS	Gas injection system
GOS	Generalized oscillator strength
HAADF	High-angle annular dark field
HOLZ	High-order Laue zone
ICP	Inductively coupled plasma
iCOM	Integrated centre of mass
iDPC	Integrated differential phase contrast
NM622	$Li(Ni_{0.6}Co_{0.2}Mn_{0.2})O_2$
LAGP	$Li_{1+x}Al_xGe_{2-x}(PO_4)_3$
LLTO	$Li_{3x}La_{(2/3)-x}TiO_3$
LPSCl	Li_6PS_5Cl
LLZO	$Li_7La_3Zr_2O_{12}$
LIB	Lithium-ion battery
NMC	Lithium nickel manganese cobalt oxides
LAADF	Low-angle annular dark field
MRI	Magnetic resonance imaging
MAADF	Mid-angle annular dark field

NBED	Nano beam electron diffraction
NDP	Neutron depth profiling
NMR	Nuclear magnetic resonance
PTCF	Phase contrast transfer function
PEO	Polyethylene oxide
PET	Polyethylene terephthalate
PED	Precession electron diffraction
PCA	Principle component analysis
ROI	Region of interest
SEM	Scanning electron microscopy
STEM	Scanning transmission electron microscopy
SAED	Selected area electron diffraction
SNR	Signal-to-noise ratio
SSB	Single-side band
SEI	Solid electrolyte interphase
SE	Solid electrolytes
SSLIB	Solid-state Li -ion battery
TEM	Transmission electron microscopy
TM	Transition metal
WPOA	Weak phase object approximation
WDD	Wigner-distribution deconvolution
XANES	X-ray absorption near edge structure
XAS	X-ray absorption spectroscopy
XRD	X-ray diffraction
XPS	X-ray photoelectron spectroscopy

Table of Contents

Overview ***2***

Chapter 1 Solid-state Li-ion Battery ***4***

1.1 Introduction 4

1.2 Li-ion Batteries 4

1.2.1 Battery Performance Parameters 5

1.2.2 Cathode 6

1.2.3 Solid-state Li-ion Batteries 9

1.3 Solid-state Electrolytes 10

1.3.1 Inorganic 11

1.3.2 Polymers 16

1.4 Challenges at Cathode/Solid Electrolyte Interface 17

1.4.1 Mechanical Compatibility 17

1.4.2 Electrochemical Stability 18

1.5 Conclusions 20

Chapter 2 Characterisation Methods on Battery Interfaces ***22***

2.1 Introduction 22

2.2 X-ray Techniques 22

2.2.1 X-ray Diffraction (XRD) 22

2.2.2 X-ray Photoelectron Spectroscopy (XPS) 24

2.2.3 X-ray Absorption Spectroscopy (XAS) 24

2.3 Neutron Techniques 25

2.3.1 Neutron Reflectometry 26

2.3.2 Neutron Depth Profiling (NDP) 26

2.4 Magnetic Resonance Techniques 27

2.5 Conclusions 28

Chapter 3 (Scanning) Transmission Electron Microscopy Techniques ***29***

3.1 Introduction 29

3.2 CTEM and STEM configurations 29

3.3 Convention Transmission Electron Microscopy 31

3.3.1 Selected Area Electron Diffraction (SAED) 31

3.3.2 Dark-field (DF) and Bright-field (BF) Imaging 31

3.3.3 High-resolution Transmission Electron Microscopy (HRTEM) 32

3.4 STEM 34

3.4.1 Single Channel Detector Imaging 34

3.4.2 Diffraction 36

3.4.3 Coherent Diffractive Imaging 38

3.5 Spectroscopy 41

3.5.1 Energy Dispersive Spectroscopy 41

3.5.2 Electron Energy Loss Spectroscopy 43

3.6 In-situ Biasing STEM 46

3.7 Conclusions 47
Chapter 4 Air Exposure and Beam Damage Study of the Solid Electrolyte 48
4.1 Introduction 48
4.2 Anaerobic Transfer Workflow 48
4.3 Air Exposure Study 49
4.3.1 Morphology Change 50
4.3.2 Chemical Composition and Distribution Change 51
4.4 Beam Damage Study 53
4.4.1 Introduction 53
4.4.2 Results and Discussion 60
4.5 Conclusions 64
Chapter 5 TEM Specimen Preparation Methodology for Solid-State Batteries 65
5.1 Introduction 65
5.2 Manual grinding 66
5.3 Ball Milling 67
5.4 Focused Ion Beam 69
5.4.1 Introduction 69
5.4.2 PFIB Damage Study at Ambient and Cryogenic Temperature 72
5.4.3 Preserving Charged State of Cathode 81
5.5 Conclusions 86
Chapter 6 Electron Energy Loss Spectrum Fine Structure Quantification 88
6.1 Introduction 88
6.2 Example Dataset 89
6.3 Quantification of TM $L_{2,3}$ Edge 90
6.3.1 Chemical Shift 91
6.3.2 Model Based ELNES Quantification 93
6.4 O Covalency 108
6.5 Conclusions 110
Chapter 7 STEM-EELS study of NMC622/LPSCl Interfacial Redox Reaction 111
7.1 Introduction 111
7.2 Spontaneous Chemical Reaction Upon Mixing 113
7.3 Interfacial Electrochemical Reaction Upon Cycling 116
7.4 Comparison of Solid Electrolyte and Liquid Electrolyte 123
7.5 Element Migration at Interface 127
7.6 Conclusions 129
Chapter 8 Summary and Future Work 131
8.1 Summary 131
8.2 Future work 133
Reference 136

Overview

Solid-state Li-ion batteries (SSLIBs) hold the promise to revolutionise battery safety and energy density. However, significant challenges must be addressed to unlock their full potential. This thesis delves into the characterisation of interfacial redox reactions between cathode $Li(Ni_{0.6}Co_{0.2}Mn_{0.2})O_2$ (NMC622) and sulphide solid electrolyte Li_6PS_5Cl (LPSCl), a critical area for advancing SSLIBs technology.

Chapter 1 introduces the background of SSLIBs and discusses the importance of electrochemical and chemical reactions at the electrode/solid electrolyte interface. **Chapter 2** reviews several key characterisation techniques, including X-ray, neutron, and magnetic field analyses, and their applications in studying electrode/electrolyte interfaces in the literature. **Chapter 3** explores the diverse configurations of transmission electron microscopy (TEM) and scanning transmission electron microscopy (STEM) and their key roles in advancing SSLIBs research.

Chapter 4 focuses on the impact of air exposure on the chemistry and morphology of LPSCl, presenting the anaerobic transfer workflow developed for this air-sensitive SSLIB material. Additionally, the mechanisms of beam damage to LPSCl are discussed.

Chapter 5 discusses the establishment of an ambient-temperature lift-out and cryo-thinning procedure in PFIB to produce uniformly thin slices of NMC622 and LPSCl with a well-preserved sharp interface. The structure degradation and chemical reduction induced by PFIB damage are characterised by atomic-resolution ADF images and core-loss electron energy loss spectroscopy (EELS). The charged state of the delithiated NMC622 is successfully preserved, and the roles of each transition metal ion upon cycling are discussed.

Chapter 6 delves into the methodology of oxidation state quantification in core-loss EELS analysis. Three methods—chemical shift, white line ratio, and energy loss near-edge structure (ELNES) fingerprint—are discussed and compared. A tailored ELNES fitting quantification

method is proposed, which captures the subtle change in EELS fine structure change and correlate them to valence state. Additionally, an intriguing post-peak feature just above the Ni-L edge was observed, combined with the partial cross-section calculated from the Dirac-based general oscillation strength, prompting a deeper investigation into the complex alterations of atomic shells during inner-shell excitations.

Chapter 7 presents a systematic study of the interfacial redox reaction between the NMC622 and LPSCl. Starting from the spontaneous chemical reactions, and then proceed to the electrochemical and chemical reaction at different states of charge. The role of the solid electrolyte in the interfacial redox reaction is highlighted through comparison to conventional liquid Li-ion batteries. Finally, the mechanism of the interfacial redox reaction is discussed through a study of elemental migration across the interface with EDS quantification.

Chapter 1 Solid-state Li-ion Battery

1.1 Introduction

Lithium-ion batteries (LIBs) have become the cornerstone of modern portable electronics due to their high energy density, fast charging rate and low weight. As the global narrative shifts towards reducing reliance on fossil fuels to combat environmental problems, LIBs play a key role. They enable the storage of renewable energy in electrochemical form and thereby emission-free energy consumption. This capability of LIBs is not only transformative for small-scale applications but also holds the potential to revolutionise large-scale energy storage such as electric vehicles (EVs) and the national grid. However, these broader applications impose new demands on LIBs, including better safety, higher energy density, enhanced charging rate, longer lifetime and lower costs. Addressing these challenges necessitates focused research on innovative materials and battery systems to overcome the limitations inherent in current LIB systems. Solid-state Li-ion batteries (SSLIBs) that replace conventional liquid electrolyte with solid electrolytes (SEs) have emerged as a promising candidate, though their path to commercialisation still faces challenges.

This introductory chapter aims to introduce the critical challenges currently limiting SSLIBs, starting with an overview of the transition from conventional LIBs to SSLIBs, and then proceeding to discuss the various types of SEs before highlighting the important role of the cathode/SE interface.

1.2 Li-ion Batteries

A conventional rechargeable Li-ion battery comprises four essential components: the cathode (positive electrode), the anode (negative electrode), and the electrolyte and the separator.

Battery operation involves alternate charging and discharging cycles. As illustrated in Figure 1.1, during charge, Li^+ ions migrate from the cathode through the electrolyte and separator, and are accommodated by the anode material's structure. Charge neutrality is maintained by the movement of electrons from cathode to anode with an applied external current, while only ionic transport is allowed to cross the electrolyte. The discharging process reverses these flows, with Li^+ ions migrating back to the cathode, where they are re-integrated into the material, and the electrons move through an external circuit and power a device.

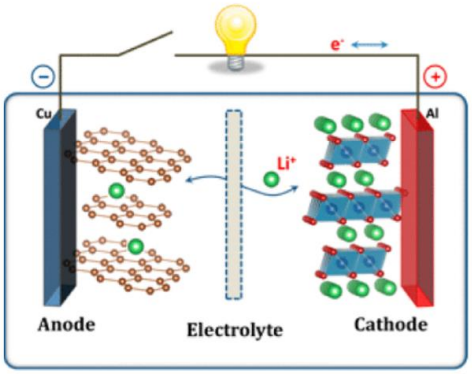


Figure 1.1: Schematic diagram of conventional Li-ion battery with graphite anode, layered transition metal oxide cathode and liquid electrolyte. [1] (Reprinted with permission from Goodenough JB, Park KS. Journal of the American Chemical Society. 2013 Jan 30;135(4):1167-76. Copyright 2013 American Chemical Society.)

1.2.1 Battery Performance Parameters

Some basic concepts of battery performance need to be presented for discussion later on. The specific capacity in $Ah \cdot kg^{-1}$ or $Ah \cdot L^{-1}$ quantifies the amount of charge that can be extracted from the battery upon discharge, based on the unit weight or volume, respectively, under specified current conditions over time. A higher capacity signifies a greater ability in hosting and releasing Li^+ ions within the electrodes.

Nevertheless, the practical capacity might be less than the theoretical maximum for some materials due to the incomplete extraction of Li. The cell voltage ΔE, difference between the

electrode potential between the cathode and anode, directly affects the energy available for electron transport. As shown in the formula below, the ΔG is the change of free energy and nF is the total change transferred in cycling.

$$\Delta E = -\Delta G/nF$$

Enhancing either the specific capacity or the cell voltage boosts the energy density of the battery. The amount of energy that can be stored in a battery, in $Wh \cdot kg^{-1}$ or $Wh \cdot L^{-1}$, is defined as the product of the capacity that can be reversibly transferred between both electrodes and the cell voltage.

The coulombic efficiency, reflecting the cycle life of the battery, is the ratio of discharge capacity to charge capacity within a cycle.

1.2.2 Cathode

Layered transition metal oxides are the most successful cathodes in commercial Li-ion batteries, among which, $LiCoO_2$ is still the most popular to date since it was proposed in 1980. [2, 3] The crystal structure of $LiCoO_2$ is formed by slabs of CoO_6 octahedra separated by Li-ions layers (Figure 1.2a). [4] The layered structure provides fast two-dimensional Li-ion diffusion pathways. However, the reversible specific capacity of $LiCoO_2$ is limited to 140 mAh/g at 4.2V vs. Li+/Li [5] which is significantly lower than its theoretical specific capacity of 274 mAh/g, due to the structural degradation when extracting more than 50% Li^+ ions during charging [6, 7] and detrimental side reactions on the surface. [8]

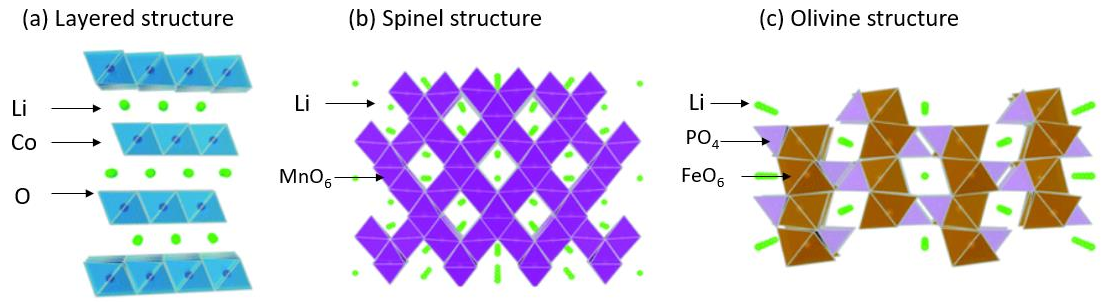


Figure 1.2: Crystal structures of three types of cathode materials. (a) layered structure, (b) spinel structure, and (c) olivine structure. [9] (Reprinted with permission of Royal Society of Chemistry, from He P, Yu H, Zhou H. Journal of Materials Chemistry. 2012;22(9):3680-95.; permission conveyed through Copyright Clearance Center, Inc.)

The spinel oxides (Figure 1.2b) with the chemical formula LiM_2O_4 were proposed aiming at cheaper and safer batteries. [10] However, their limitation is low practical capacity ($LiMn_2O_4$: 120 mAh/g at 4V vs. Li+/Li [11]) which fades severely upon cycling. Another type of cathode materials is the olivine phosphate oxide $LiFePO_4$ (LFP) (Figure 1.2c), which stands out for its low cost, low toxicity, good thermal stability with reasonable practical capacity of 160 mAh/g at 4 V vs. Li^+/Li. [12] However, the low operating voltage of $LiFePO_4$ at 3.4 V vs. Li^+/Li limits its energy density and therefore its widespread use in EVs. [13]

Specifically, for the layered oxide cathodes, implementation of alternative transition metals (TM) has been explored to improve the stability of the $LiCoO_2$. Firstly, the more cost-efficient Li_xNiO_2 was investigated. The Ni^{2+}/Ni^{4+} redox couple offers high capacity. However, it facilitates electrolyte decomposition, forming the thicker cathode electrolyte interphase (CEI) on the cathode surface. The CEI contains both inorganic components such as LiF, Li_2Co_3, MnO_x, CoO_x, NiO, and organic species such as carbonates and oligomers/polymers. The solid electrolyte interphase (SEI) formed between anode and electrolyte shares similar components but lacks the transition metal composites. [14-16] These products in CEI can obstruct Li ion migration across the electrode/electrolyte interface. Apart from the addition layer of interphase formed on cathode surface, the cathode's crystal structure near the surface also degrades due to the cation

mixing between Ni^{2+} (0.69 Å) and Li^{+} (0.76 Å) sites, which impede the diffusion pathway of Li^{+} ions during cycling. In addition, Li_xNiO_2 also suffers from weaker thermal stability as Ni^{3+} is more readily reduced than Co^{3+}. [17, 18] Therefore, rather than using single TM oxides such as $LiCoO_2$ and $LiNiO_2$, Ohzuku *et al.* proposed binary ($LiCo_{0.5}Ni_{0.5}O2$) and ternary ($LiCo_{0.33}Ni_{0.33}Mn_{0.33}O_2$) systems, optimising the balance of stability and capacity. [19] Mn has been introduced as the structure stabiliser, especially at a highly delithiated state. Ni has been included for better capacity. At the same time, Co is used to reduce the Li/Ni cation mixing. [20-23] As a result, Ni-rich layered transition metal oxide cathodes which offer high specific capacity tend to be the most promising candidates for LIBs. Increase the Ni content can improve the capacity however with the price of severe capacity fading during cycling. [24] As shown in Figure 1.3, $Li(Ni_{0.6}Co_{0.2}Mn_{0.2})O_2$ (NMC622) has been found to have the best combination of relatively high specific energy of 180 mAh/g at 4.3V vs. Li^{+}/Li and good tolerance to the high voltage cycling and thermal abuse condition. [25-27] Therefore, NMC622 was chosen for interfacial study in this thesis.

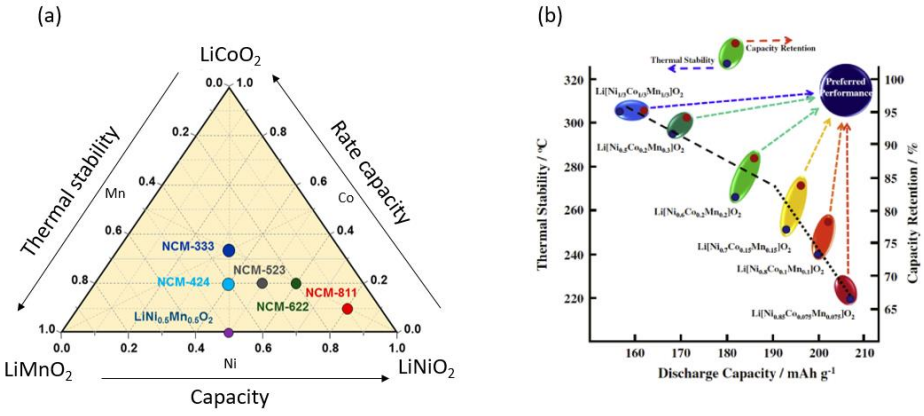


Figure 1.3: (a) Ternary diagram of transition metal ions contained in Li-ion batteries specified by their performance. [25] (Reprinted with permission from Chakraborty A, Kunnikuruvan S, Kumar S, Markovsky B, Aurbach D, Dixit M, Major DT. Chemistry of Materials. 2020 Jan 6;32(3):915-52. Copyright 2020 American Chemical Society.) (b) Schematic correlation of performance and safety with Ni content. [26] (Reprinted with permission from Zhang SS. Energy Storage Materials. 2020 Jan 1;24:247-54., Copyright 2020, Elsevier)

1.2.3 Solid-state Li-ion Batteries

Graphite, with its high Li diffusivity, high electrical conductivity and low manufacturing costs, is the predominant anode material in commercial Li-ion batteries. However, Li metal has gained extensive attention for its extraordinarily high specific capacity (3860 mAh/g, graphite: 372 mAh/g [28]), low density (0.59 g/cm^3), and the most negative electrochemical potential among anode materials (-3.04 V vs the standard hydrogen electrode). [29] However, Li metal's application in rechargeable batteries with typical liquid organic solvent-based electrolytes is hindered by challenges such as excessive solid electrolyte interphase (SEI) formation and dendrite growth, which lead to capacity fading and short-circuit of the battery and thermal runaway. Various strategies, including high salt concentrations [30, 31] and the addition of electrolyte additives, [32, 33] have been proposed to mitigate these issues, yet they often fall short at high charging rates.

SEs potentially enable the use of the Li metal anode, due to the possibility of bipolar stacking design, which would greatly increase the energy density of batteries. [34] SEs with good chemical stability against Li metal can reducing capacity fade by minimising Li consumption in the SE/anode reaction. Additionally, SEs act as a barrier that separates the electrodes and prevents the chemical interaction of dissolved active materials. Moreover, the conventional liquid electrolytes have the safety risk of catching fire and even exploding due to the highly flammable organic solvents used in liquid electrolytes. Using SEs will enhance battery safety, as electrolyte leakage can be completely avoided. Therefore, SSLIBs are regarded as one of the critical next-generation electrochemical energy storage technologies and have continued to attract enormous attention over recent years.

However, the use of SEs adds significant challenges, mostly in the production of dense and ionically conductive thin films, and in ensuring effective ionic conduction with cathode materials. In contrast to liquid electrolyte cells, where thin-film cathodes ensure maximal contact and

carbon additives enhance electron transport, solid-state cells require a thorough mixing of the cathode material with SE to ensure large contact area and form composite cathode. However, integrating electronic insulating SE into the cathode can hinder electron conduction, and volumetric changes in the cathode during charge and discharge cycles can lead to loss of contact. Additionally, the requirement for high-temperature sintering of some oxide SEs for enhanced ionic conductivity poses a risk of degrading cathode materials.

The following sections will delve into the various types of SEs developed to address these challenges, highlighting their unique properties and potential applications in solid-state Li -ion batteries.

1.3 Solid-state Electrolytes

An ideal SE should possess several key properties, including

- High ionic conductivity at room temperature (> 1 mS/cm).
- Negligible electronic conductivity to prevent self-discharge (< 10^{-7} mS/cm).
- Chemical and electrochemical stability with Li metal anode and common cathode materials; or formation of self-passivating and ionically conducting interphases.
- Mechanical toughness to resist the dendrites penetration.
- Mechanical pliability to accommodate volume changes at electrode/electrolyte interface.
- Robustness to air and moisture.
- Facile processability.

Various types of SE have been proposed and studied. They can be categorised into inorganic, polymer and composite materials, their advantages and limitations will be discussed.

1.3.1 Inorganic

Oxides

NASICON Li-ion conductors

These are Li analogues of sodium superionic conductors NASICON, characterised by a structure formula of $LiM^{IV}_2(PO_4)_3$, where M^{IV} includes Ti, Zr, Ge, or Hf. They feature a three-dimensional network formed by MO_6 octahedra connected to PO_4 tetrahedra, enabling fast Li-ion transport through interstitial channels. [35]

Enhancing ionic conductivity is achievable through doping. For instance, incorporating metals like Al, Cr and Si into $LiTi_2(PO_4)_3$ not only boosts its electrochemical stability but also raises its ionic conductivity significantly at room temperature. [36, 37] The substitution of Ti with Ge has also shown promising results. High ionic conductivity values in the order of 10^{-4} $S{\cdot}cm^{-1}$ have been reported for the glass-ceramic $Li_{1+x}Al_xGe_{2-x}(PO_4)_3$ (LAGP). [38, 39] Glass-ceramics benefit from having lower grain boundary resistances than pure crystalline ceramics due to the presence of a favourable amorphous phase between grains. [40] Nevertheless, stability issues remain as Ti and Ge are both easily reduced upon on contact with Li metal.

Perovskite-type Li-ion conductors

The perovskite-type conductor $Li_{3x}La_{(2/3)-x}TiO_3$ (LLTO) represents a class of Li-ion conducting materials, crystallizing into an ABO_3 perovskite structure. [41] LLTO distinguishes itself with a broad electrochemical stability window exceeding 8 V vs. Li^+/Li and exhibits remarkable stability in air, water, and extreme temperatures. The ionic conductivity of LLTO varies depending on the Li content, affecting the crystal symmetry and, consequently, the Li-ion conduction pathways. [42]

Although LLTO shows high bulk conductivities around 1 $mS \cdot cm^{-1}$, its grain boundary ionic conductivity may only attain values of up to 10^{-2} mS/cm. In addition, the tendency of reduction of Ti^{4+} to Ti^{3+} against Li metal induces side reaction and increases the interfacial resistance.

Garnet-type Li-ion conductors

Garnet-type materials, with the general formula $Li_7La_3M_2O_{12}$ where M includes Ta, Nb, Zr, are among the most promising candidates for oxide-based Li-ion conducting materials. For their wide electrochemical stability window, good ionic conductivity and compatibility with Li metal, [43, 44] garnet-type materials like $Li_7La_3Zr_2O_{12}$ (LLZO) have garnered extensive research interest. [45] The structure of LLZO facilitates Li-ion transport through a three-dimensional framework, which, depending on synthesis conditions, can crystallize in either cubic or tetragonal phases, with the cubic phase generally exhibiting higher ionic conductivities but requiring a much higher sintering temperature of 1200°C. [46] Al, Ga and Ta are commonly used to stabilise the cubic phase at room temperature. [47, 48]

Oxide SEs shows good stability with both Li metal and high voltage cathodes. However, this comes at the cost of requiring high sintering temperatures (above 1000°C), which degrades the cathode materials in the composite cathodes and necessitate more expensive processing. Additionally, the oxide solid electrolyte generally shows low ionic conductivities in the order 0.1 mS/cm. Furthermore, the mechanical property of oxides are stiff and brittle [49] which poses challenges in maintaining good interfacial contact as the cathode undergoes volumetric changes during cycling.

Sulphides

Thio-LISICON Li-ion conductors

The discovery of sulphur-based analogues to oxide-based LISICON materials, termed 'thio-LISICON,' has introduced a category of solid electrolytes with exceptional electrochemical properties. [50] These materials, such as $Li_{10}GeP_2S_{12}$ [51] and $70Li_2S{\cdot}30P_2S_5$ [52] glass-ceramic, demonstrate ionic conductivities surpassing those of traditional liquid electrolytes (>10 mS/cm).

The high ionic conductivity of sulphur-based Li-ion conductors is attributed to the larger anion size S^{2-} than an oxide ion O^{2-}, providing larger pathways for Li-ion conduction, and higher polarisation than O^{2-}, resulting in a weaker interaction between the Li^+ ions. [50] However, the challenges for the thio-LISICON type SEs are their instability with air, moisture, Li metal and also high-voltage cathode, together with the mechanical brittleness.

Argyrodite

Argyrodite Li_6PS_5X (X=Cl, Br, I) is based on the parent argyrodite structure Li_7PS_6, with one chalcogen replaced by one halogen atom and one fewer Li. The halide-substituted argyrodite has better structural stability and an ionic conductivity of 10^{-3} S cm^{-1} at room temperature. [53]

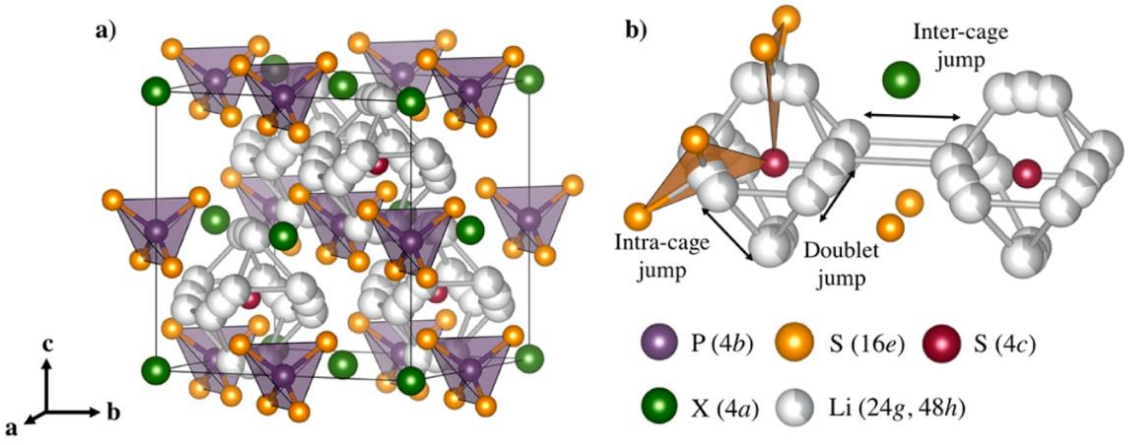


Figure 1.4: (a) Crystal structure of Li_6PS_5X (X=Cl, Br, I) (b) Structure of Li cage, a corner of PS_4^{3-} tetrahedra and a separated S^{2-} ion is used to illustrate 3 different types of Li diffusion paths[54] (Reprinted with permission from Kraft MA, Culver SP, Calderon M, Böcher F, Krauskopf T, Senyshyn A, Dietrich C, Zevalkink A, Janek J, Zeier WG. Journal of the American Chemical Society. 2017 Aug 9;139(31):10909-18. Copyright 2017 American Chemical Society.)

Deiseroth *et al*. [55] reported that Li argyrodite Li_6PS_5X has a similar crystal structure to Ag based argyrodite Ag_8GeS_6, comprising of a close-packed tetrahedral structure (Figure 1a). In Li_6PS_5X structure, halogen anions X^- form a face-centred cubic lattice (Wyckoff 4a) with PS^{3-} tetrahedra on the octahedral sites (P – Wyckoff 4b, S – Wyckoff 16e) and a separated S^{2-} anions in half of the tetrahedral voids (Wyckoff 4c) forming $(Li^+)_6(PS_4^{3-})S^{2-}X^-$.

Li atoms are randomly located on 48h and 24g Wyckoff sites in space group $F\bar{4}3m$. The 48h site refers to the equilibrium site that host the bulk of Li^+ ions, [56] and 24g site act as transition state when Li^+ ions hop between two equilibrium 48h sites. The two types of Li positions form cage-like polyhedra creating three pathways for Li diffusion (Figure 1.4b). [54]

The choice of halogen in argyrodite plays an important role in ionic conductivity. In nuclear magnetic resonance (NMR) spectra of Li_6PS_5Cl (LPSCl), Li_6PS_5Br, Li_6PS_5I, an increase in structural disorder can be observed when changing from I to Br and Cl. [55] The preferred substitution of S by Br/Cl over I can be rationalised by comparison of radii: S^{2-} has radii of 184 pm, while Cl^-, Br^- and I^- have radii of 181 pm, 196 pm, 220 pm respectively. Site disorder between halogen anions (4a Wyckoff position) and separated S^{2-} anions (4a Wyckoff position) significantly affects inter-cage jumping and therefore ionic conductivity. Chen *et al*. [56] reported ordered structures such as I-containing argyrodite have a higher migration barrier based on density functional theory (DFT) calculations. The calculated results align well with electrochemical impedance spectroscopy results which show that the ionic conductivity of Li_6PS_5I is several orders of magnitude lower. [57]

Despite the high ionic conductivity of LPSCl (1.33 mS/cm at room temperature) [58], ease of processability and low cost (compared to Ge-containing SE such as $Li_{10}GeP_2S_{12}$), [51] the poor stability limits its long-term application in SSLIBs. The instability involves two main reactions, the first is the chemical/electrochemical reaction with electrodes. The other one is the

decomposition at high potential. The decomposition of Li_6PS_5Cl at 2.2-3.0 V vs. Li^+/Li has been reported to form elemental sulphur, Li_2S, polysulphides, phosphates and LiCl, [58, 59] and at 2 V vs. Li^+/Li into Li_2S, Li_3P and LiCl have been reported. [60, 61]

In comparison with oxides, sulphide SEs exhibit higher ionic conductivity and are mechanically softer, enabling better contact with cathode particles. While high-temperature sintering is not required for sulphides, their sensitivity to air and moisture complicates the manufacturing process. Sulphides face challenges from poor stability against Li metal and high voltage cathodes, leading to degradation of the electrolytes. Notably, for some sulphides, such as Li_3PS_4 and Li_6PS_5Cl, degradation primarily happens during the initial charging cycle but then ceases in subsequent cycles, [49, 62, 63] which is in contrast to oxides like LLTO and LAGP, with which continuous degradation during extended cycling eventually results in cell failure. [64, 65] Thus, the stability concerns associated with sulphides can potentially be overcome with improved interfacial design.

Other inorganic solid-state electrolytes

Apart from oxides and sulphides which have been the most extensively investigated for their materials development and working mechanism, there are many other types of inorganic SEs such as Li nitrides, boron-based SEs and Li halides. The nitride SE such as Li_3N has been reported to reach ionic conductivity of 1 mS/c when doped with H^+. [66] It also shows promising stability with Li metal anode. However, its highly reducing nature necessities air- and water-free process environment. [67] Furthermore, high temperature sintering is required for high ionic conductivity in these ceramics. [68] Boron-based SEs such as borohydride $LiBH_4$, borane $Li_2B_2H_{12}$ and carboranes $Li_2(CB_9H_{10})_{0.7}(CB_{11}H_{12})_{0.3}$ [69-72] has attracted attention for their high room-temperature ionic conductivity of 10 mS/cm and excellent stability with Li metal anode.

However, their drawbacks of poor stability with high voltage cathodes have been reported. [73] Li halides Li_3MX_6 (X = Cl, Br) has emerged as promising SE materials recently. [74, 75] Halides have shown high oxidative stability window of over 4V vs. Li^+/Li and moderate ionic conductivities without the need of high temperature sintering. [76-78] Nevertheless, the primary limitation lies in the stability with Li metal anode. Riegger *et al.* observed metal (Y or In) interphase formation on Li_3YCl_6 or Li_3InCl_6 in contact with Li metal. [79] The electron conduction of the metal leads to continuation of the side reaction and also increase of interfacial resistance. Strategies such as element substitution [80] and addition of a sulphide SE as separator at interface forming hybrid halide-sulphide SEs [81, 82] have been proposed to address the challenge of halide SEs.

1.3.2 Polymers

Solid polymer electrolytes are composed of Li-ion conducting salts dissolved in polymers, commonly poly-ethylene oxide (PEO)-based and exhibit advantages including ease of film fabrication and lower costs due to established solution-based casting methods. [83-85] However, they typically have low room-temperature ionic conductivities lower than 10^{-2} mS/cm, necessitating operation at elevated temperatures. [83, 84, 86] They also face challenges with Li metal reactivity, forming resistive interlayers and dendrite growth. [84, 87] Compositing polymer electrolytes was proposed to add inorganic solid electrolytes to polymers to enhance their properties, though challenges remain in improving ionic conductivity and resistance to dendrite growth compared to dense inorganic solid electrolytes. [88, 89]

1.4 Challenges at Cathode/Solid Electrolyte Interface

Significant advancements in the ionic conductivity of SEs have been achieved. Compared to conventional liquid electrolytes (5–10 mS/cm for $LiPF_6$ and $NaPF_6$ in the liquid solvent ethylene carbonate : dimethyl carbonate (EC:DMC)), [90] many SEs have been reported to have comparable or even higher ionic conductivities. For instance, LGPS-type $Li_{9.54}Si_{1.74}P_{1.44}S_{11.7}Cl_{0.3}$ has reached an ionic conductivity of 32 mS/cm. [91]

Despite these high conductivities, the high impedance at the interface between the solid electrolyte and the electrode remains a significant challenge. This interfacial impedance can become the dominant factor in the internal resistance of a battery, particularly in SSLIBs that use sulphide electrolytes paired with high-voltage oxide cathodes. [92-94] In the following sections, the mechanical compatibility and electrochemical stability of the SE/cathode interface will be discussed further.

1.4.1 Mechanical Compatibility

In SSLIBs, the lithiation and delithiation of cathode materials during cycling cause volume changes which pose substantial challenges. The inherently poor wettability of SEs means they cannot easily accommodate the volume change of cathode active material particles. Consequently, significant mechanical stresses are induced during cathode expansion, potentially causing cathode particles to crack, leading to capacity fading and increased interfacial resistance. Furthermore, cracking of the SE can lead to short-circuit failure. [34] Similarly, contraction of cathode particles can result in contact loss with the SE, rendering a fraction of the active material inaccessible in subsequent cycles.

SEs with lower Young's modulus, such as Li thiophosphates, show a better ability to accommodate these volume changes, [34] compared to stiffer SEs such as LLZO and LLZTO,

which lack the required mechanical flexibility. [95] Strategies to mitigate these effects include applying external pressure, coating cathode particles with elastic materials, or incorporating polymer fillers to enhance the SE's flexibility.

1.4.2 Electrochemical Stability

Maintaining electrochemical stability at the cathode/SE interface is challenging due to the narrow electrochemical stability windows of many SEs, which can lead to self-decomposition at high voltages and reactivity with the electrode materials. Decomposition can generate phases at the interfaces with reduced ionic conductivity. Furthermore, interdiffusion and chemical reactions between the SE and cathode can create additional phases that obstruct ion conduction. [92, 96] Extensive research has been conducted on the additional phase between SE and cathode, CEI. It is typically a poor ionic conductor which adds significant resistance to the cell. [96] For example the oxidation of LGPS at 2.14 V vs. Li^+/Li yields GeS_2, S and Li_3PS_4, which can be further oxidised to S and P_2S_5 at 2.31 V vs. Li^+/Li. [97] Cycling causes irreversible thickening of the CEI, which triggers capacity fading. Electrochemical stability of the SE with the cathode is therefore highly desirable. There are known SEs (LATP and LAGP) that have greater electrochemical stability than LEs at high potentials. However, few SEs are currently known which can be used in direct contact with high voltage cathodes (> 5 V vs. Li^+/Li). An overview of electrochemical stability windows of SEs is plotted in Figure 1.5.

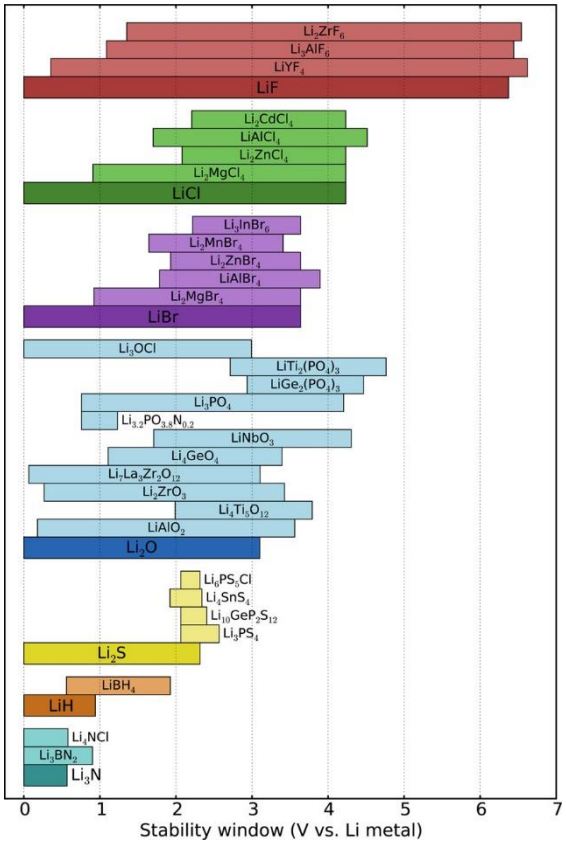


Figure 1.5: Computationally predicted electrochemical stability windows of solid-state electrolyte materials. [67] (Reproduced from Richards WD, Miara LJ, Wang Y, Kim JC, Ceder G. Chemistry of Materials. 2016 Jan 12;28(1):266-73. Under a Creative Commons Attribution license)

Sulphide SEs face large capacity loss right from the first cycle. [98, 99] This capacity loss in the initial cycle is associated with a substantial and irreversible increase in interfacial resistance at the cathode/sulphide SE interface. The primary reason of these degradations is the redox reaction occurring between the cathode and the sulphide SE, leading to detrimental interfacial changes.

The mechanism underlying this problem starts with the easy oxidation of S^{2-} ions, which results in the condensation of PS_4 units. This process significantly reduces the lithium content and can even lead to the formation of elemental sulphur at the interface, identified as a primary contributor to the substantial capacity loss observed during the initial cycle in high-voltage solid-state cells. [98] Furthermore, the interaction between oxide cathodes and sulphide SEs

introduces additional degradation pathways through the exchange of S^{2-} and O^{2-} ions. This exchange leads to the formation of PO_4^{3-} polyanions [62, 100] and transition-metal sulphides (e.g., Co_9S_8, [96] $CoNi_2S_4$, Ni_3S_4 [67]), resulting in impedance growth and further capacity loss.

Calculations suggest the driving force for the chemical reaction between sulphide electrolytes and oxide cathodes is substantial (>300meV/atom). [97] The formation of resultant compounds of transition-metal sulphides and various polyanions are energetically favourable due to the higher bond energy of P–O and TM–O bonds compared to P–S and TM–S bonds, respectively. [101] Experimental analyses using XPS [98] and Tof-SIMS [102] have confirmed species such as PO_x^{y-} and SO_x^{y-} at the interface after cycling.

A strategy to mitigate these side reactions involves applying an electronically insulating but ionically conducting electrode coating, such as $LiNbO_3$ or Li_2ZrO_3. [103, 104] The coating materials need to be stable across the electrode's voltage range and chemically inert with both the electrode and SE. However, the introduction of new interfaces between the electrolyte/coating and the coating/active material raises additional complexity. Imperfections in the coating can expose the electrode surface to the SE, risking unwanted interfacial reactions, yet these imperfections are necessary for electron transport. [103] A fundamental understanding of the coatings' functionality, materials properties and procedure is essential in achieving long-term stability.

1.5 Conclusions

In conclusion, better interfacial design for SE/cathode is highly desired to maintain electrochemical stability. While it is essential to obtain fundamental understanding of the parasitic redox reaction at their interface. In the following chapter, various characterisation tools used to study battery materials will be discussed. This discussion will include their applications

in investigating battery interfaces, transitioning to an introduction of the STEM technique and its specific relevance and application in the realm of battery research in the chapter 3.

Chapter 2 Characterisation Methods on Battery Interfaces

2.1 Introduction

The shift from liquid to solid electrolytes introduces new complexities in the material and interface properties, especially the electrode/electrolyte interface, necessitating advanced characterisation techniques. Understanding the microscopic and macroscopic properties of the interface is crucial for optimising performance and reliability. This chapter will briefly explore the advantages and limitations of several key characterisation techniques that use X-rays, neutrons, and magnetic fields, focusing on their applications in addressing the CEI problems. This discussion will set the stage for a detailed examination of electron microscopy techniques in the next chapter.

2.2 X-ray Techniques

X-ray has advantages of high penetration ability and sensitivity of periodicity in specimen. While convenient characterisation can be accessed using lab-based X-ray, synchrotron-based x-ray provides a high-intensity, highly collimated beam of X-rays with tunable wavelengths and minimal instrumental broadening.

2.2.1 X-ray Diffraction (XRD)

XRD is a powerful technique used to analyse the crystalline structure of materials, relying on the principle of constructive interference of X-rays by the crystal lattice planes within a sample.

The diffraction pattern is plotted as angle 2θ against absolute intensity. the interplanar spacing can be calculated from the peak position - angles θ through the Bragg's law below. λ is the

wavelength of the incident X-ray, d is the interplanar spacing, θ is the incident angle as labelled in Figure 2.1.

$$n\lambda = 2d \sin\theta$$

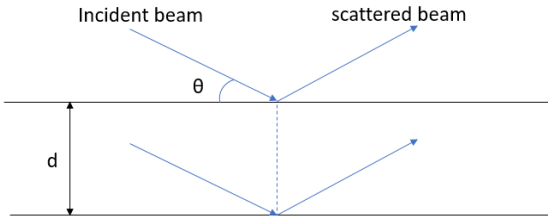


Figure 2.1: Bragg diffraction in a crystal with a d-spaced plane.

Therefore, XRD is helpful in characterising crystalline species generated from interfacial reactions. [105, 106] Vardar *et al.* used synchrotron-based XRD observed formation of $La_2Zr_2O_7$ between LLZO and $LiCoO_2$. [107]

Rietveld refinement is a methodology used for precise determination of crystal structures. This technique involves matching a calculated diffraction pattern generated from a model structure to the observed data through least-squares refinement, allowing for accurate determination of atomic positions and thermal parameters. [108] Rietveld refinement on synchrotron-based XRD results quantitatively identified the solid solution interphases formed between $LiFePO_4$ cathode and $Li_{3+x}P_{1-x}Si_xO_4$ solid electrolyte. [106]

Nevertheless, XRD characterisation falls short for poor crystalline samples. While the components in CEI are commonly amorphous, the application of XRD in CEI study are limited. Additionally, XRD only provide bulk characterisation.

2.2.2 X-ray Photoelectron Spectroscopy (XPS)

XPS is a surface analysis technique that quantitatively measures the elemental composition within the initial first 10 nm of the material's surface. The technique is based on the photoelectric effect, [109] where an X-ray beam irradiates the material's surface, causing the ejection of core-level electrons from its atoms as photoelectrons. The kinetic energy of these emitted photoelectrons is directly proportional to the binding energy of the electrons within the atom. Collection of the signal yields an XPS spectrum, where the relative intensities of the peaks provide information about the sample's elemental composition and chemical state.

For interface study, due to the surface sensitivity of XPS, XPS is ideal to perform depth profiling in coupling with ion sputtering technique. XPS and Ar^+ ion sputtering were used to identify the elemental distributions for Co, Li, O, La, Zr and C across the $LiCoO_2$/$Li_7La_3Zr_2OV$ interface. [107] Wang *et al.* highlighted the necessity of $LiNbO_3$ coating between $LiCoO_2$ and $Li_{10}GeP_2S_{12}$ in reducing the interfacial reaction by quantifying the oxidisation peak through S-2p, P-2p in XPS. [110]

The surface sensitivity gives XPS good spatial resolution at thickness direction (z dimension), but the signals are averaged over larger surface areas which limits XPS' spatial resolution in x, y dimension. In addition, the surface-limited resolution of XPS makes it susceptible to contamination and ion beam damage on the sample surface caused by ion sputtering techniques.

2.2.3 X-ray Absorption Spectroscopy (XAS)

XAS spectra collect X-ray absorption as a function of incident X-ray beam energy. XAS spectra exhibit characteristic features known as absorption edges, corresponding to the energy required to excite core-level electrons to unoccupied states. Area within 50 eV above the edge of absorption of an element is referred as X-ray absorption near edge structure (XANES) which

provides information about the oxidation state, coordination environment, and electronic structure. Beyond this, Extended X-ray Absorption Fine Structure (EXAFS) reveals details about the local atomic arrangement surrounding the absorbing atom, including bond distances, coordination numbers and disorder.

Depth resolution at nm-scale can be achieved in XAS by varying the emission angles. [111] Therefore, XAS is able to study the cationic redox reactions in electrodes from both surface and bulk perspective. The reduction of Co ion at interface between $LiCoO_2$ and $80Li_2S{\cdot}20P_2S_5$ was identified by Chen *et al.* using depth resolved XAS. They also highlighted the addition of Li_3PO_4 interlayer can suppress Co ion reduction and maintain a stable interface. [112] Li *et al.* revealed a metastable intermediate state of sulphide electrolyte at high voltage and parasitic reactions with cathodes during the charge/discharge process, which leads to the surface structural reconstruction of Ni-rich cathodes, through operando XAS XANES. [113]

2.3 Neutron Techniques

Unlike x-rays which primarily get scattered by electrons, neutrons get scattered by nuclei. Due to the low scattering probability of nuclei interaction, neutrons can travel further down beyond the sample surface before being scattered. Therefore, the neutron scattering is generally considered a bulk and non-destructive probe, which will benefit greatly in-situ / in-operando studies. Additionally, the scattering cross-section of neutrons does not simply scale with atomic number. Some light elements such as H, Li, O, and N exhibit relatively high neutron scattering cross-sections, even surpassing some heavy metals. This unique characteristic enables the direct determination of light element coordinates in crystalline structures and facilitates imaging of light elements against a background of heavier elements. These features have made neutron scattering useful to study light elements in Li-ion battery. The neutron reflectometry and

neutron depth profiling (NDP) are surface/interface probes, although their working mechanisms are quite different.

2.3.1 Neutron Reflectometry

NR is sensitive to subtle changes of the scattering length density as a function of depth. Therefore, NR has been used to study the CEI and lithium distribution. For example, the intercalation of Li in Li_2ZrO_3 surface modified $LiCoO_2$ was studied using NR, and the superior rate capability was attributed to the faster desolvation of Li compared to the unmodified $LiCoO_2$. [114] In-situ NR is commonly used to identify the changes in structure and composition of CEI layer such as on the surface of $LiCoO_2$, [114] $LiFePO_4$, [115] and $LiMn_{1.5}Ni_{0.5}O_4$. [116]

2.3.2 Neutron Depth Profiling (NDP)

NDP measures the distribution of certain elements based on depth. In an NDP measurement, a flux of cold neutrons coming out of a neutron guide pass through a Li-containing specimen and react with the isotope ^6Li to generate two highly energetic charged particles, $^6Li + n \rightarrow \alpha + {}^3H$. charged particles lose energy while traveling to the surface, while the energy loss depends on the travelled distance. The depth of the initial location of reaction can be retrieved by measuring the final energy of the particles, which leads to the distribution of the element of interest. Because the incoming energy of the neutron is negligible (< 4 meV) and the interaction rate is small, typically < 0.01% of the incoming fluence, the energy deposition is minimised and therefore specimen heating and damage can be avoided. In addition, the selective nature of nuclear activation ensures that Li spectra are clean, being free of interference from other elements. These differences represent a significant advantage of NDP for measuring the distribution and cycle of Li in thin-film batteries. [117] An overlithiated surface layer on

$LiMn_{1.5}Ni_{0.5}O_4$ induced by LiPON deposition was observed by NDP. [118] NDP has also been used to compare the effect of coating layer on the crystallographic defects concentration on $LiNi_{0.5}Co_{0.2}Mn_{0.3}O_2$ surface. [119]

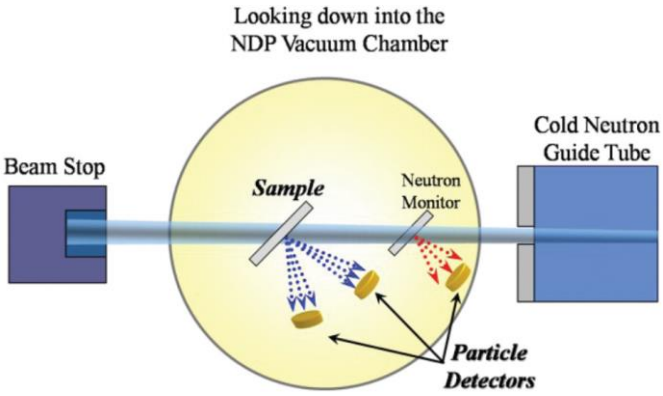


Figure 2.2: Schematic diagram of NDP setup. [117] (Reprinted with permission from Wang H, Downing RG, Dura JA, Hussey DS. 2012 (pp. 91-106). Copyright 2012 American Chemical Society.)

2.4 Magnetic Resonance Techniques

Nuclear magnetic resonance (NMR) spectroscopy is an element-specific, highly sensitive probe of the local environment, it measures the spin of atomic nuclei by collecting resonant electromagnetic signal when an external magnetic field is applied to the specimen. [120, 121] NMR provides detailed study of spontaneous lithium-ion transport across interfaces, as illustrated by Yu *et al.'s* research on interface between Li_6PS_5Br and Li_2S sulphide electrode, where two-dimensional lithium-ion exchange was mapped through NMR. [122]

Magnetic resonance imaging (MRI) complements NMR spectroscopy by providing spatial information of the chemical species under investigation in three dimensions. Chien *et al.* revealed Li depletion from the $Li/Li_{10}GeP_2S_{12}$ interfaces and increased heterogeneity of Li distribution upon electrochemical cycling through three-dimensional ^7Li MRI. [123]

NMR is not restricted by lack of crystallinity so it can be applied to highly disordered system. The major limitation of NMR is the poor sensitivity to signals and therefore large quantity of sample is required for distinct signals. [124]

2.5 Conclusions

In this chapter, a range of characterisation techniques based on X-ray, neutron scattering, and magnetic field sources have been explored, highlighting their contributions to research in interface study in SSLIBs based on their source features: superior energy resolution of synchrotron-based X-ray in probing the electronic structure; high sensitivity to detect light elements such as Li od neutron techniques, the non-invasiveness nature of NMR in studying Li ion transport. Among the various characterisation techniques, the modern analytical scanning transmission electron microscopy (STEM) stands out for its versatility at high spatial resolution. Unlike the depth profiling of X-ray and neutron techniques, where even nm-scale resolution can be achieved only in z direction, STEM can provide a wealth of information at highly localised area: STEM-electron energy loss spectroscopy (EELS) is able to provide the high energy resolution spectroscopy mapping at atomic resolution, structure and bonding information of light elements can be retrieved through phase imaging and EELS. This technique's profound impact on advancing our understanding of battery materials will be the focus of the next chapter.

Chapter 3 (Scanning) Transmission Electron Microscopy Techniques

3.1 Introduction

Among the advanced characterisation techniques, STEM stands out for providing invaluable insights into the structural, compositional, and electronic properties of materials at the atomic scale. Its unparalleled simultaneous high spatial and energy resolution has significantly advanced research in renewable energy, biological materials, and nanotechnology. In this chapter, techniques including diffraction, Z contrast imaging and phase contrast imaging, and spectroscopy of energy dispersive spectroscopy (EDS) and EELS and their application in battery materials study will be discussed.

There are two common instrumental configurations in transmission electron microscopy: conventional transmission electron microscopy (CTEM) and STEM, each offering unique capabilities for nano-characterisation. These configurations are discussed below.

3.2 CTEM and STEM configurations

In CTEM, electrons are emitted and accelerated by a high voltage, typically ranging from 80-300 keV. These electrons, with characteristic wavelengths of 2-4 pm, provide resolution significantly beyond the capabilities of optical microscopes. Instead of glass lenses used in optical microscopy, electromagnetic lenses are used in the TEM to deflect the negatively charged electrons via the Lorentz force. The strength of these lenses is finely tunable through current control, enabling a wide variety of experimental setups. However, achieving high resolution can be hampered by the inherent instability and aberrations associated with electromagnetic lenses.

Post-acceleration, the electron beam is shaped and magnified by a condenser lens system, usually comprising two or three separate lenses. As the schematic in Figure 3.1a shows, condenser lens 1 images the electron source onto the front focal plane of the condenser lens 2 which creates a broad parallel beam at the sample plane.

The electron beam then interacts with an electron-transparent sample, forming a real image of the sample and diffraction pattern via the objective lens. The objective lens can accept a wide range of angular scattering and is therefore susceptible to lens imperfections, especially the spherical aberration. These distorted high angle electrons can degrade the overall resolution - an objective lens aperture can be used to block scattering from high angles and reduce the effects of lens aberrations.

The intermediate and projector lenses magnify the diffraction pattern or image formed by the objective lens, projecting the electrons onto a pixelated detector such as a charge coupled device (CCD), complementary metal oxide semiconductor (CMOS) or direct electron detector (DED). When the intermediate lens is adjusted to project the image plane of the objective lens, the intensity captured on the detector translates into a highly magnified image of the sample. If the strength of the intermediate lens is instead adjusted to project the back-focal plane of the objective lens, then a diffraction pattern will be obtained on the detector.

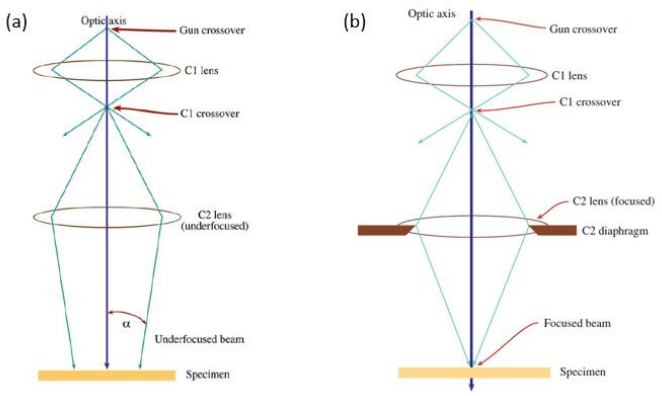


Figure 3.1: Schematic diagram of (a) CTEM and (b) STEM configuration. [125] (Reproduced with permission from Springer Nature)

3.3 Convention Transmission Electron Microscopy

3.3.1 Selected Area Electron Diffraction (SAED)

SAED provides detailed information about a material's crystal structure, orientation, and defects. In diffraction mode, by employing a selected area aperture at the image plane of the objective lens, SAED allows for examination of diffraction patterns from specific sample regions. This has been applied to identify phase transformations in battery materials, [126, 127] such as the layered to spinel structural transformation upon charging in lithium nickel manganese cobalt oxides (NMC) cathode materials. [128] Moreover, due to the low electron dose accumulated by using parallel beam illumination and the ability to select highly localised areas, SAED is particularly suited for analysing nano-phases [129-131] in beam sensitive battery materials.

3.3.2 Dark-field (DF) and Bright-field (BF) Imaging

Switching from diffraction to imaging mode can be easily achieved by adjusting the intermediate lens strength to project the image plane of the objective lens. The objective aperture on the

back focal plane can be used to select specific spots on the diffraction pattern to contribute to image formation. If a specific diffraction spot, corresponding to a particular set of lattice planes, is selected, it ensures that only electrons satisfying the Bragg equation with a specific diffraction angle contribute to image formation. Selecting spots other than the central spot results in a DF image that distinctly highlights specific crystallographic features within the imaged region. Conversely, selecting the central spot, forms a BF image. In BF image, location where diffraction takes place appears dark and the rest appears bright. The DF and BF imaging are useful in mapping the distribution of crystalline phases in the specimen, but the limitation is the relatively low resolution as the images are formed by diffraction contrast.

3.3.3 High-resolution Transmission Electron Microscopy (HRTEM)

Atomic resolution can be achieved in CTEM imaging in HRTEM. Unlike the DF/BF imaging, an objective aperture is usually not used in HRTEM. HRTEM relies on the phase contrast by using spherical aberration to cause coherent interference between transmitted and scattered electron beams to achieve high resolution. This high resolution, coupled with the low dose of the parallel electron beam and high dose efficiency – as every electron contributes to imaging formation when an objective aperture is not inserted – makes CTEM particularly valuable in providing crystallographic information at high resolution for beam-sensitive battery materials. For example, phase boundary migration and anisotropic lithium insertion in $FePO_4$ particles were observed via HRTEM. [132] Studies have also discussed the role of point defects in triggering phase transitions through direct visualisation in HRTEM, [133] offering a deeper understanding of material properties and reaction mechanisms at the atomic scale.

However, interpretation of HRTEM images is challenging due to contrast reversal and also the aberration-limited resolution. To explain this, the phase contrast transfer function (PCTF) of

HRTEM will be briefly discussed. Under weak phase object approximation (WPOA), the phase contrast transfer function $T_{eff}(u)$ of HRTEM can be seen as the product of an aperture function $A(u)$, envelope functions $E_c E_a$ and a phase-distortion function $\chi(u)$.

$$T_{eff}(u) = 2A(u) \sin \chi(u) \, E_c E_a$$

When the objective aperture is large enough, the aperture function can be approximated as equal to 1. The envelop functions are the chromatic aberration envelope E_c and the angular spread envelope E_a. They determine the "information limit" beyond which spatial information can no longer be transferred from the specimen to the image. The phase-distortion function is mostly affected by spherical aberration and defocus. As the phase-distortion function is based on the sine function, the numerical sign of PCTF flips multiple times before reaching the information limit. The flips of the PTCF from positive to negative cause contrast reversals in the image which complicates image interpretation. Therefore, the first crossover of the PTCF with the x axis is referred to as the instrumental resolution limit because intuitive image interpretation is only possible for spatial frequencies below this limit; interpretation of higher spatial frequencies can only be achieved with post-processing or image simulations.

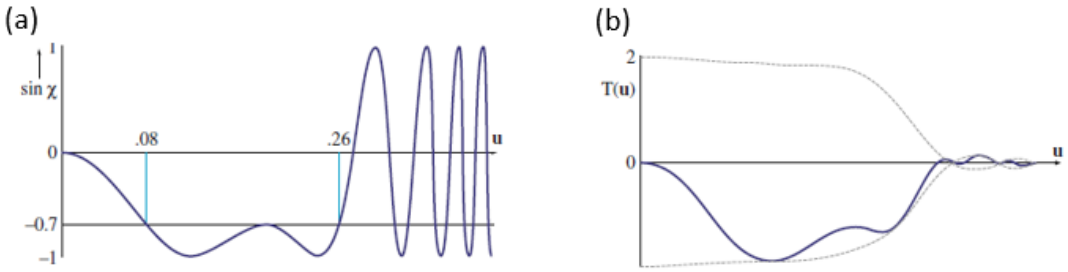


Figure 3.2: (a) $\sin \chi(u)$ versus u without envelope function (b) $T(u)$ versus u modified by envelope function (dashed line) Δf = -100nm, C_s = 2.2nm [125] (Reproduced with permission from Springer Nature)

The introduction of aberration correctors and field emission guns allows for spherical aberration correction and source coherency improvement, thus a flatter phase contrast transfer function

and a higher resolution can be achieved. Nevertheless, the accessibility of aberration corrected TEM is limited by its high cost.

3.4 STEM

In the STEM configuration, the electron beam is focused onto the sample by adjusting the strength of condenser lens 2, as shown in Figure 3.1b Scanning coils are used to raster scan this convergent electron beam across the sample. To achieve atomic resolution, a probe diameter of ~0.1 nm is commonly used to ensure sufficient sampling. A set of single-channel detectors with various collection angle such as high-angle annular dark field (HAADF) detector, annular bright field (ABF) detector can be used to collect scattered electrons, enabling the formation of detailed images where each scanned point corresponds to an intensity value. Additionally, a pixelated detector can be used to record the diffraction pattern at every probe position, forming a 4D dataset, which has many applications such as strain mapping, phase imaging, and the mapping of electric and magnetic fields.

3.4.1 Single Channel Detector Imaging

HAADF imaging is incoherent and lack of contrast reversals. Its detector is designed to collect high-angle Rutherford scattered electrons, predominantly emphasising atomic number (Z) contrast while suppressing diffraction contrast. [134-136] This technique eliminates misinterpretations arising from interference artefacts and enables the simultaneous acquisition of inelastic EELS signals. The HAADF contrast, approximately proportional to $Z^{1.7}$,[137, 138] enables the quantification of contrast from atomic column. For the layered cathode material which consists of alternating slabs of light Li and O, and heavy transition metal (TM) ions, HAADF

is the ideal technique to study TM migration into the Li layer, [139] and subtle phase changes at the nanoscale. [140]

However, HAADF imaging has limitations, including challenges in imaging light elements and low dose efficiency. Additionally, the quantitative interpretation of HAADF imaging can be complicated by the channelling effect which causes a non-linear relationship between the scattering cross section and the number of atoms. The periodic potential of the atom can act as a small focusing lens to the incident beam and therefore the atoms underneath experience a more focused probe, leading to a stronger electron scattering than the previous atom. [141] In practice, HAADF is usually simultaneously acquired with another lower collection angle technique such as EELS, 4D STEM or ABF.

As the collection angle decreases, phase contrast and diffraction contrast become more pronounced. low-angle annular dark field (LAADF) imaging, which employs an inner radius slightly larger than the bright-field discs, incorporates diffraction contrast and has been used to visualise material phases, defects, and strain. Mid-angle annular dark field (MAADF) imaging, characterised by inner angles between HAADF and LAADF, offers a balance of diffraction contrast and Z-contrast suitable for specific material interpretations.

ABF-STEM, by collecting electron beams at small angles, provides phase-contrast images where contrast is less dependent on the atomic number, allowing for simultaneous detection of both light and heavy elements. ABF imaging is particularly effective in resolving atomic columns and observing light elements without strict specimen thickness requirements. ABF imaging has captured changes in local atomic structure and Li-ion location at the phase separated interface within Li_xFePO_4 platelets. [142, 143] Clear visualisation of the structural change in the oxygen sublattice upon Li extraction is achieved through ABF imaging enabling direct observation of O-O peroxo-like dimers in $Li_{0.5}IrO_3$ [144] and O vacancy formation in Li_4FeSbO_6 [145] and helping

to establish the fundamental relation between the anionic redox process and the evolution of O-O bonding in layered oxides.

While STEM imaging is versatile in providing different imaging contrasts, the single-channel detectors are susceptible to image distortion due to specimen drift, and beam-sensitive materials are susceptible to damage from the intense convergent beam. 4D-STEM has drawn great research attention as an extension of traditional STEM capability. Instead of the binning the collected electrons into a single channel detector, the distribution of the transmitted electrons is recorded in a 2D diffraction pattern at each probe position in a 2D raster scan across the sample, resulting in a 4D dataset. A wealth of information can be obtained through reconstruction of the 4D dataset, enabling advanced analyses such as phase imaging, strain mapping, and the mapping of magnetic and electric fields. The implications of these diverse 4D-STEM techniques for battery materials characterisation, will be explored in further detail in subsequent sections.

3.4.2 Diffraction

Nano Beam Electron Diffraction (NBED)

NBED offers a unique balance between CTEM and STEM configurations, employing a nearly parallel scanning probe to scan across the sample surface as shown in Figure 3.3a. This approach provides a spatially resolved map of lattice parameter variation.

NBED is commonly used to map phase variation in battery materials. [146, 147] The technique's small probe diameter enables detailed observation of highly localized phase transitions. Using NBED, Liu *et al.* successfully characterised three distinct phase changes within a 20nm region on the surface of an NMC111 cathode after the first charging process. [148] The incorporation of precession electron diffraction (PED) has notably refined the precision of NBED. PED reduces the

effects of dynamical diffraction, thereby enabling detection of fine structural features such as low-angle grain boundaries and single dislocations. The application of PED enhanced NBED in the study of subtle lattice mismatches in NMC111 reveals the polycrystalline nature of the particle. [149]

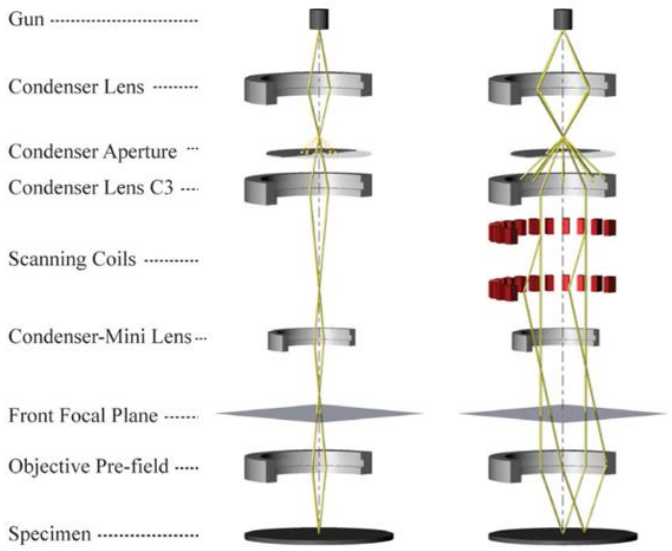


Figure 3.3: Schematic representation of ray paths in (a) NBED, (b) CBED/STEM configurations. [150] (Reproduced from Ganesh KJ, Kawasaki M, Zhou JP, Ferreira PJ. Microscopy and Microanalysis. 2010 Oct;16(5):614-21, with permission from Microscopy Society of America)

Convergent Beam Electron Diffraction (CBED)

CBED uses a larger convergence angle than NBED, achieving smaller probe diameters for better resolution. The diffraction spots broaden into discs in the back-focal plane in CBED (Figure 3.3), allowing the interference fringes to be resolved and providing rich information about crystal symmetry, structure factors and lattice strains.

CBED is more sensitive than NBED for the analysis of high-order Laue Zone (HOLZ) lines. HOLZ lines are sharp lines observed in the CBED disks, produced by high-order Bragg diffraction from lattice planes. The position of HOLZ lines is very sensitive to small changes in lattice parameter

and the local strain due to the large scattering angle, but requires extensive simulation for accurate interpretation. In battery studies, CBED is predominantly utilised for phase identification, [151-153] and measuring lattice parameters and Li composition. [154]

The diffraction pattern records the intensity of the Fourier transform of the exit wave function. Valuable phase information can be retrieved through reconstruction of the exit wave; several algorithms exist to perform this reconstruction. Details of phase contrast imaging using CBED will be discussed in the following section.

3.4.3 Coherent Diffractive Imaging

Differential Phase Contrast (DPC) & Centre of Mass (COM)

A DPC detector typically consists of diametrically opposed segment pairs, commonly in a four or 16-segment configuration. DPC computes the difference between opposing detector segments for each probe position in a 2D scan. This process constructs a detailed map reflecting the sample's electrostatic field, which can arise from various sources such as electric fields, magnetisation, density, or thickness variations. If a pixelated detector is used instead, the shift of the bright field disks can be calculated through a centre of mass (COM) approach or by applying virtual masks to convert the diffraction pattern into segmented area signals as acquired using DPC detector. [155]

It is important to note that DPC and COM calculates the distribution of the projected electrostatic field, rather than direct phase contrast imaging. To obtain phase contrast, which corresponds to the projected potential, integrating over the scanning positions becomes necessary. This process leads to the development of integrated DPC (iDPC) or integrated COM (iCOM), techniques that yield phase-contrast images derived from DPC principles. Moreover, the projected charge distribution can be calculated by taking differentiation of DPC or COM,

leading to the differentiated DPC (dDPC) or differentiated COM (dCOM) imaging. Overall, DPC (COM), iDPC (iCOM), and dDPC (dCOM) correspond directly to projected electric field, projected potential, and projected charge distribution, respectively. [156]

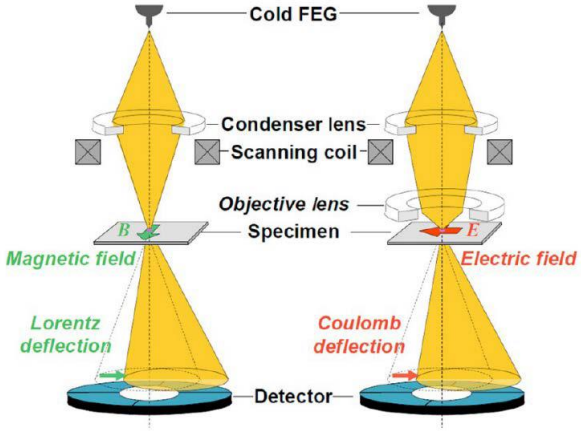


Figure 3.4: Schematic illustration of DPC STEM for electromagnetic field imaging for a specimen containing (left) a magnetic field and (right) an electric field. [157] (Reprinted from Shibata N, Findlay SD, Matsumoto T, Kohno Y, Seki T, Sanchez-Santolino G, Ikuhara Y. Accounts of chemical research. 2017 Jul 18;50(7):1502-12. Copyright 2017. With permission from American Chemical Society.)

Due to the higher electron utilisation rate and the integration processes which filter out noise, [156, 158] iDPC can achieve a high signal-to-noise (SNR) ratio with a lower electron dose than conventional HRTEM. [159] The lose-dose and high SNR makes iDPC exceptionally suitable for studying the surface structure, defects, and interfaces of battery materials. DPC-STEM has provided insights into the charge density distribution and transport of Li ions during charging in Li-rich materials ($Li_{1.2}Mn_{0.54}Co_{0.13}Ni_{0.13}O_2$) with high spatial resolution. [160] Wang *et al.* used iDPC to study the space charge effect between $LiCoO_2$/LPSCl which is important for lithium-ion transport across the electrode/electrolyte interface. [161] The difficulty of using the DPC/COM for battery study is how to isolate the Li ion segregation/deficiency from other factors that would also cause beam shift, such as the mean inner potential, thickness profile and crystallographic defects.

Ptychography

Ptychography offers enhanced resolution from aberration retrieval and phase sensitivity than conventional imaging methods. In ptychography, a series of diffraction patterns are collected at different positions of the specimen. Using a convergent probe, the illuminated areas of the diffraction patterns partially overlap, enabling the retrieval of phase information through diffraction interference. [162]

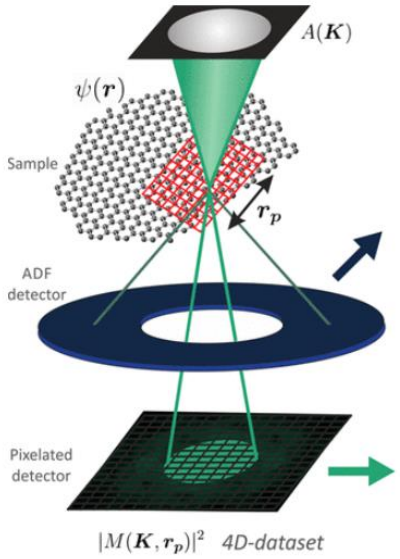


Figure 3.5: Schematic of 4D data set used in STEM ptychography. [163] (Reproduced from Lozano JG, Martinez GT, Jin L, Nellist PD, Bruce PG. Nano letters. 2018 Sep 26;18(11):6850-5. Under a Creative Commons Attribution license)

The quest for precise phase information has led to the development of various reconstruction algorithms, primarily categorised into non-iterative methods: single-side band (SSB) and Wigner-distribution deconvolution (WDD); and iterative methods, such as the extended ptychographic iteration engine (ePIE). During reconstruction, residual lens aberrations can be diagnosed and compensated, which saves the fine tuning of aberration before data acquisition, and minimises beam damage.

Experimentally, non-iterative ptychography has been applied for imaging both light and heavy elements in Li-rich cathode materials. Remarkably, it has achieved aberration-corrected atomic

resolution phase imaging with beam current in the sub-picoampere range. [163] This work highlights the potential of ptychography in high-resolution phase imaging while minimising electron beam-induced damage to sensitive battery materials.

A significant advancement in the iterative method ePIE is the introduction of the inverse multi-slice method which improves the resolution in the Z axis and allows for three-dimensional imaging. In this method, a thick specimen is approximated as a stack of layers, the simulation processes the interaction of a probe through each layer sequentially. Therefore, inverse multi-slice ptychography does not only allow for phase-contrast images at different positions along the beam axis, but also addresses the multiple scattering problem, thereby enhancing resolution and providing a more detailed understanding of the specimen. Yoon *et al*. used Inverse multi-slice ptychography to provide depth information on Li vacancies in NMC111 while retaining high lateral resolution. [164] The drawback of ptychography is the absence of real-time data processing during acquisition, due to its computational demands. Additionally, the widespread application of ptychography is limited by the cost of high readout speed pixelated detectors.

3.5 Spectroscopy

EDS and EELS are powerful spectroscopic techniques integral to the modern analytical TEM system. These methods provide profound insights into the chemical composition, bonding, valence states, and electronic properties of specimens. Their applications in the study of battery materials will be discussed in this section.

3.5.1 Energy Dispersive Spectroscopy

High-loss EELS and EDS detect the primary and secondary aspects of the interaction between atoms and incident electrons respectively. During the interaction, ionisation is the primary

process in inelastic scattering. Kinetic energy of the incident electron beam is transferred to the specimen which leads to the ejection of an inner-shell electrons from an atom, creating an unstable excited state. To regain stability, an electron from a higher energy level transitions to the vacant lower energy level, emitting an X-ray photon characteristic of the element involved.

EDS is a popular technique in materials science for a multitude of reasons including: its high efficiency in acquiring signal from a broad spectrum of elements, except for very light elements (hydrogen to boron); the ability to rapidly process data during acquisition; the low noise background owing to the counting mechanism of the detector; and the retractable detector design, which gives EDS high compatibility with both CTEM and STEM configurations. EDS is therefore one of the principal techniques used for analysing localised composition variations.

In battery research, EDS has proven to be invaluable. Hu *et al.* used atom-resolved EDS maps to directly visualise structural variations in the solid-state electrolyte material $La_{(1-x)/3}Li_xNbO_3$. [165] Yang *et al.* used EDS to reveal the presence of a phosphorus-rich SEI layer at the boundaries of $LiMn_{0.4}Ni_{0.4}Co_{0.2}O_2$ (NMC442) electrodes. [166] This finding conclusively indicates the permeation of the electrolyte deep into the core of agglomerated particles via the interfaces between primary particles. Such an observation highlights the importance of interfacial design in determining the overall performance of battery materials.

However, EDS has limitations, including the low X-ray ionisation probability and the limited solid angle of the detector which can lead to poor counting statistics, especially in thin specimens. Improvements can be made by installing multiple EDS detectors or more practically using longer dwell time, but at the price of higher dose which is detrimental for battery materials. Another problem is the detection of light elements. The emitted X-ray can lose energy through re-absorption and fluorescence before it is detected which can limit the technique's effectiveness in characterising light elements.

3.5.2 Electron Energy Loss Spectroscopy

The first measurement of the transmitted electron energy loss dates back to 1941 when Ruthemann [167] used a magnetic spectrometer and photographic recording. Since then, EELS has developed significantly and its history is marked by numerous instrumental innovations. In 1949, Möllenstedt [168] published the design of the electrostatic energy analyser which allowed for more precise measurements of energy losses. A critical development is the introduction of the Wien filter, a type of velocity filter that uses perpendicular electric and magnetic fields. It can be used as a monochromator and as an energy selector before and after the specimen position in the column respectively. The transition from photographic plates to digital detectors marked a significant leap, with CCDs and later direct electron detectors offering much higher sensitivity and resolution.

Software for data acquisition, processing, and analysis developed alongside the hardware improvements. Those innovations collectively contributed to the evolution of EELS from a qualitative tool to a highly precise quantitative technique. The applications of EELS extend across material science, physics, chemistry, and beyond, offering unparalleled insights into the electronic and chemical properties of materials at the atomic level.

In EELS, a high-energy electron beam is transmitted through a thin specimen. During this process, the electrons interact with the atoms in the sample elastically or inelastically. Once the beam has traversed the specimen, it enters a spectrometer where the electrons are dispersed based on their velocity (energy) and then projected onto a detector to create a spectrum that maps energy loss against intensity. Depending on the lost electron energy range, the EEL spectrum is typically divided into three sections: zero loss peak (ZLP, $E = 0$ eV), the low-loss spectrum (0 eV $< E < 50$ eV), and the core-loss spectrum ($E > 50$ eV).

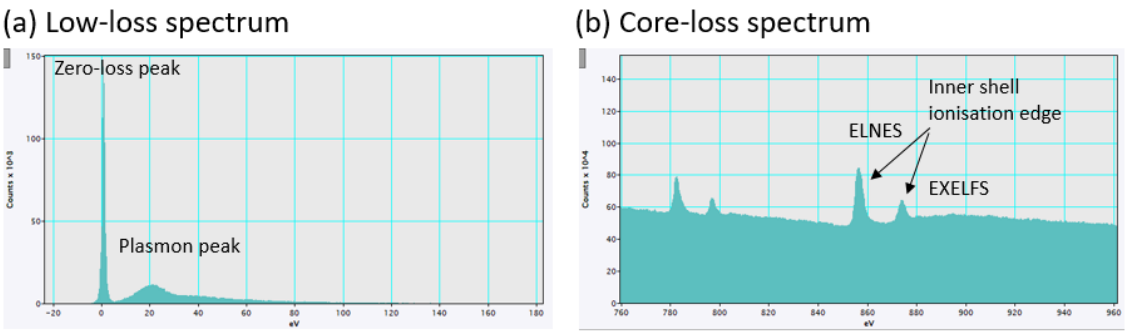


Figure 3.6: Schematic diagrams of EELS (a) low-loss spectrum consists of zero-loss pea and plasmon peak, and (b) core-loss spectrum, where ELNES and EXELFS can be observed on an inner shell ionisation edge.

ZLP

The ZLP represents the incident beam portion that passes through the specimen without detectable energy loss, comprising electrons that interact elastically with the electrostatic field of atomic nuclei. While this part of the spectrum contains valuable information about crystallography and phase contrast, it is not retrievable with current EELS techniques.

Low-loss Spectrum

Following the ZLP, the phonon peak arises from lattice vibration excitations with typical energy range from a few meV to 0.1 eV. Phonon excitations used to be categorised in the ZLP as the energy loss was too small to be detected. However, improvements in energy resolution from the cold field emission gun (FEG) , spectrometer and monochromator [169] have enabled the detection of these subtle features [170-174] and provided lattice information for interface [175] and thermal conductivity studies [176].

The remainder of the low-loss spectrum is characterised by the interactions of the incident electrons with outer atomic shell electrons, resulting in energy losses typically below 50 eV. Within this energy range, two principal interaction mechanisms are observed. In cases where outer-shell electrons are part of a delocalised band rather than confined to atomic core orbits, the incident beam can induce oscillations in the valence electron density, leading to a plasmon peak. This usually occurs in the range of 10-30 eV, followed by a monotonic drop in intensity at

higher energy losses. Conversely, in insulators where electrons are more tightly bound to nuclei and plasmon effects are minimal, single-electron excitations predominate. Most materials fall into between the 2 extremes. The low-loss spectrum is rich in information and can be used to study bandgap [177, 178], plasmon [179, 180] and infrared-vis-UV excitation [181-183].

Core-loss Spectrum

In the core-loss region, inner-shell electron excitations give rise to ionisation edges. These edges are marked by a rapid increase in intensity at the ionisation threshold, followed by a slower decrease, contrasting with the plasmon peaks that exhibit a sharper decline. The onset energy of these edges corresponds to the characteristic energy gap between atomic shells, enabling quantitative elemental analysis through identification and area measurement under the ionisation edges. Where sample thickness and energy resolution permits, the fine structure in the near-edge and extended regions provide valuable insights into crystallography and energy band structure. Therefore, EELS is an indispensable tool for probing coordination, bonding, valence states, and more. In the context of battery materials, where complex electrochemical reactions affect battery performance, EELS's ability to provide a detailed understanding is crucial.

Acquisition of an energy loss spectrum at each pixel of a scanned image, resulting in a three-dimensional data set often referred to as a spectrum-image data cube, with two spatial dimensions (x and y coordinates on the sample) and one spectral dimension (energy loss). Spectrum imaging combines spatially-resolved imaging with spectroscopy, allowing high spatial resolution mapping of element distribution, chemical states, and electronic properties.

A notable application of EELS in battery research is the quantification of valence states,[184, 185] particularly for TM ions commonly found in cathode materials. Changes in the EELS fine structure can be used to understand the role of TM ions during cycling. Graetz *et al.* highlighted how Ni primarily contributes to charge compensation in the lithiation/delithiation processes, while the valence of Co remains unchanged in $Li_{1-x}Ni_{0.8}Co_{0.2}O_2$. [186] EELS also unveils the mechanisms

behind parasitic side reactions that can lead to cathode material inactivation and capacity loss, by tracking the valence states of TM ions with high spatial resolution. [113]

EELS addresses the limitation of EDS in detecting light elements, enabling direct observation of Li^+ ions within operating lithium-ion batteries (LIBs). [187-189] This capability is vital for advancing our comprehension of battery operation mechanisms and identifying potential issues.

Zhang *et al.* used EELS to map Li with high spatial and temporal resolution, shedding light on the Li^+ migration mechanisms in $Li_4Ti_5O_{12}$ during cycling. [190] Beyond elemental mapping, changes in chemical environment can be retrieved through analysis of the EELS fine structure, as demonstrated in the investigation of the phase transition mechanisms in spinel $LiMn_2O_4$ via Li-K and Mn-M edge, [191] and in characterising the composition and distribution of the SEI. [192]

3.6 In-situ Biasing STEM

In-situ STEM studies are cutting-edge approaches for investigating the dynamic processes in solid-state batteries at the micro and nano scales, providing real-time insights into the structural and chemical changes during battery operation. In contrast to in-situ TEM studies of liquid-state batteries, which typically involve the liquid electrolyte to be held under high vacuum in TEM column within silicon nitride membrane, [193, 194] in-situ TEM studies of solid-state batteries sidestep these requirements. However, they present their own set of experimental challenges in preparing electrochemically active nanobatteries that are sufficiently electron-transparent for TEM analysis, while also ensuring mechanical stability.

Focused ion beam has been proved effective in solving the sample preparation problem. Brazier *et al.* performed the first FIB lift-out preparation of a SSLIB nanobattery, revealing chemical element migration at the interface. [195] Li accumulation at the interface of Li_xCoO_2/LiPON during in-situ biasing was observed, illustrating the dynamic interfacial reactions. [196]

Subsequently, Wang *et al.* expanded upon these findings with in situ STEM coupled with EELS on $LiCoO_2$/LiPON interface, proposing that the formation of an ionic resistive layer is a key mechanism behind interfacial impedance. [189] Furthermore, the impact of different coatings on Li accumulation has been characterised through in-situ DPC-STEM in studies of the $LiCoO_2$/LPSCl interface. [161]

3.7 Conclusions

In this chapter, the diverse configurations of TEM and STEM and their application in advancing solid-state battery research have been reviewed. Unlike other characterisation techniques that offer averaged structural and chemical insights, as discussed in Chapter 2, (S)TEM techniques provides the unique advantage of targeting precise local regions of interest. Particularly, the analytical STEM, enhanced by EDS and EELS, offers a offers a comprehensive study by simultaneously delivering detailed structural, compositional, and electronic structural information. This makes (S)TEM the ideal tool for probing the interfacial redox reaction in SSLIBs.

Despite the promising capabilities of (S)TEM techniques, a significant challenge in studying SSLIB is the highly air-sensitive nature of battery materials, such as the sulphide solid electrolyte LPSCl. This sensitivity necessitates solutions to prevent air exposure and consequent degradation, which can alter the material's intrinsic properties. Therefore, transitioning to the next chapter, the development of an anaerobic transfer workflow tailored for SSLIB materials will be explored.

Chapter 4 Air Exposure and Beam Damage Study of the Solid Electrolyte

4.1 Introduction

The capability of scanning transmission electron microscopy (STEM) in analysing battery materials is undeniable, yet there are significant challenges to characterisation, predominantly due to the high sensitivity of these materials to air and electron beams. This initial results chapter focuses on the impact of air exposure on the chemistry and morphology of LPSCl, alongside presenting the anaerobic transfer workflow developed for this air-sensitive solid-state battery material. Furthermore, the mechanisms of beam damage to LPSCl will be discussed, offering valuable insights for future STEM investigations on this material.

4.2 Anaerobic Transfer Workflow

A crucial aspect of the experimental setup in this thesis involves careful transfer of battery samples between the glovebox and the TEM to prevent air exposure. For this purpose, the JEOL double-tilt vacuum transfer holder (model 01030RSTH), which is designed for secure sample handling under vacuum conditions has been used. Figure 4.1 illustrates the holder in two states: with the sample stage extended for loading and retracted for transfer, securely sealed within the holder's body.

The transfer process is initiated by degassing the holder under vacuum in the antechamber for one hour to remove the residual dust and water molecules. Following degassing, the holder is moved into the glovebox, where the TEM grid is carefully loaded onto the sample stage. After loading, the air lock mechanism is engaged to encapsulate the sample stage, allowing it to be retracted and sealed in vacuum within the holder. All loading steps are performed within the Ar environment of the glovebox. As the glovebox is located a 15-minute walk away from the

microscope room, the vibration and negative pressure inside the sealing chamber of vacuum holder can easily cause leakage through the O ring. Therefore, an AtmosBag from Aldrick (model Z564427-1EA) was used to seal the retracted holder and create a further level of Ar encapsulation during holder transfer. The holder, which extends to 78cm in length, is compatible with the MBRAUN glovebox system which has an 80cm long antechamber, facilitating the safe transfer of the retracted holder.

Upon reaching the TEM room, the Ar bag and air lock are removed and the retracted holder is ready for insertion into the TEM. In the specimen chamber of TEM, while the specimen is still sealed in the vacuum chamber in the holder, the holder undergoes three vacuum pumping cycles to desorb any water molecules that may have adhered to the holder's tip during transfer. After the completion of these cycles, in the N_2-filled specimen chamber, the sample stage can be released from the vacuum chamber. Finally, with the specimen chamber fully pumped down for the fourth and also the last time, the holder and specimen can be inserted from the sample exchange chamber into the TEM column.

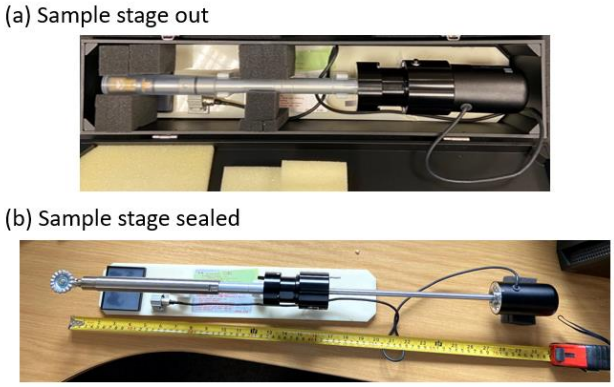


Figure 4.1: DT vacuum transfer holder with the (a) sample stage out, (b) sample stage sealed.

4.3 Air Exposure Study

Argyrodite LPSCl is a promising SE due to its high ionic conductivity and processability. However, there are several hurdles to its wider application including its low stability in air, leading to a

substantial decline in ionic conductivity and the release of toxic H_2S gas, as depicted in the hydrolysis reaction below:

$$Li_6PS_5Cl + 6H_2O \rightarrow LiCl + Li_3PO_4 + 5H_2S + 2LiOH$$

$$2LiOH + CO_2 \rightarrow Li_2CO_3 + H_2O$$

The decomposition products of LPSCl have been well studied both experimentally [197-199] and theoretically [67, 200], such as those by Tsukasaki *et al*., which have confirmed the hydrolysis reactions of LPSCl through the identification of products like Li_2CO_3, Li_2SO_4, and Li_3PO_4 via electron diffraction. They also noted a reduction in crystallite size from the micrometre to nanometre scale following air exposure. [201]

Therefore, instead of identifying chemical species, this section will focus on changes in particle morphology and elemental distribution due to air exposure. This will highlight the importance of the anaerobic transfer protocol from glovebox to microscope.

4.3.1 Morphology Change

Significant changes in particle morphology were observed in LPSCl before and after air exposure. Initially, the LPSCl powder was dispersed on the TEM grid and then transferred into the microscope using the TEM vacuum transfer holder. The pre-exposure state is captured in Figure 4.2a. After deliberately retracting the holder and exposing the grid to air for two seconds, the ADF image of the same particle in Figure 4.2b shows the loss of distinct features at the edge of the particle, and a rougher surface with cracks and cavities. The comparison reveals substantial morphological changes post-hydrolysis, affirming the effectiveness of the sample transfer method in preserving sample integrity.

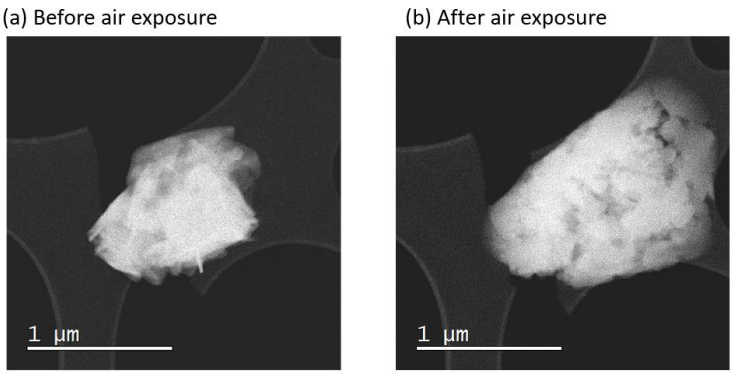


Figure 4.2: ADF image of the same LPSCl particle (a) before and (b) after air exposure.

4.3.2 Chemical Composition and Distribution Change

Oxygen is introduced to LPSCl through hydrolysis. However, detection of O contamination during vacuum transfer of LPSCl has not been investigated in the literature. This section aims to bridge this gap using STEM-EDS to study O contamination as a result of air exposure, and also the changes in the elemental distributions and ratios.

$$\frac{C_A}{C_B} = k_{AB}\frac{I_A}{I_B}$$

Ionisation cross section varies with atomic number and therefore the X-ray intensity in EDS result needs to be calibrated for qualitative measurement. [202] The Cliff-Lorimar factor k_{AB}, which can be determined theoretically and experimentally, [125, 203] correlates the X-ray intensity (I_A and I_B) to concentration ratio C_A and C_B as shown in the formula above. Variations due to particle thickness were also removed by normalising the EDS maps with simultaneously acquired ADF images. Figure 4.3 shows the EDS maps of a LPSCl particle with a mere 8 at% of O contamination, which can be attributed to O arising from impurities from the column and TEM grid. By comparison, a LPSCl particle which had purposely been exposed to air shows a high oxygen contamination of 32 at% and displays pronounced oxygen segregation at the surface and chlorine inhomogeneity in Figure 4.3a and also sulphur deficiency in Figure 4.3b.

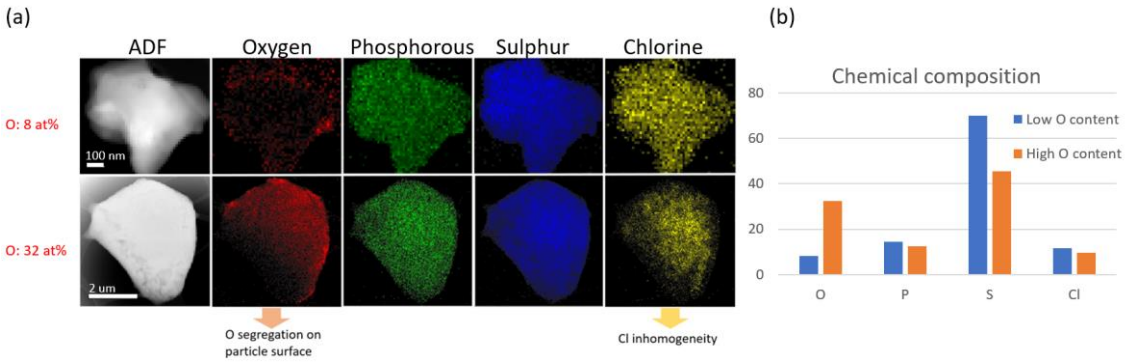


Figure 4.3: Comparison of (a) EDS maps of LPSCl particle with 8 at% O content (top row), and with 32 at% O content (bottom row), and their (b) quantified chemical composition of O, P, S and Cl. (Data acquisition credit to Dr. Weixin Song)

During the optimisation of the air tightness control of transferring the TEM vacuum holder, many EDS data were acquired with different extent of air exposure. The analysis of these data revealed a decrease in the sulphur to phosphorus (S:P) ratio from 5 to 4 with increasing oxygen content, as shown in Figure 4.4, indicating a release of H_2S.

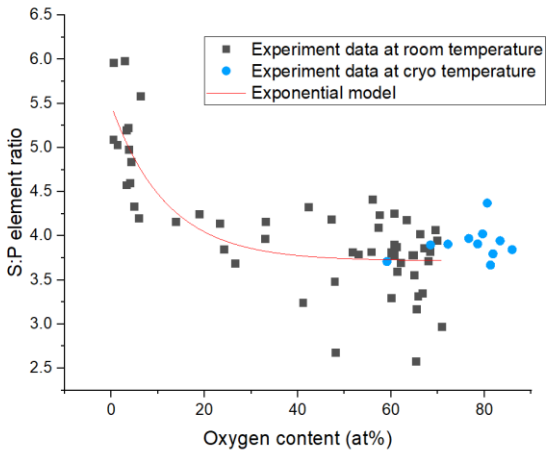


Figure 4.4: S:P element ratio changes against O content, blue datapoints were collected using cryo holder. (Data acquisition credit to Dr. Weixin Song and Dr. Emanuela Liberti)

Notably, Figure 4.4 includes data points obtained using the Fischione Model 2550 cryo transfer tomography holder. Unfortunately, this cryo holder is not capable of vacuum transfer. Despite efforts to minimise LPSCl exposure by grid loading in a liquid nitrogen environment and rapid

transfer processes to the microscope specimen chamber, ice layer formation on the samples was inevitable as shown in Figure 4.5. The amorphous features around the LPSCl particles in Figure 4.5 are uniquely observed at cryogenic temperature, compared to the ADF images at room temperature in Figure 4.2. The EDS mapping in Figure 4.5c has been normalised to the simultaneous acquired ADF image to highlight the element distribution without the effect of thickness profile. The O map confirms those features are not LPSCl but rich in O content, which is attributed to the ice layer formed from the condensed water during the rapid transfer from liquid nitrogen to the microscope specimen chamber. Similarly to the effect of hydrolysis reaction in Figure 4.3, Cl inhomogeneity is also observed in Figure 4.5c with the presence of ice layer. The reason may attribute to the repetitive melt and refreeze of ice layer over LPSCl particle, induced by the scanning of highly energised electron beam and low temperature, which triggers hydrolysis reaction of LPSCl.

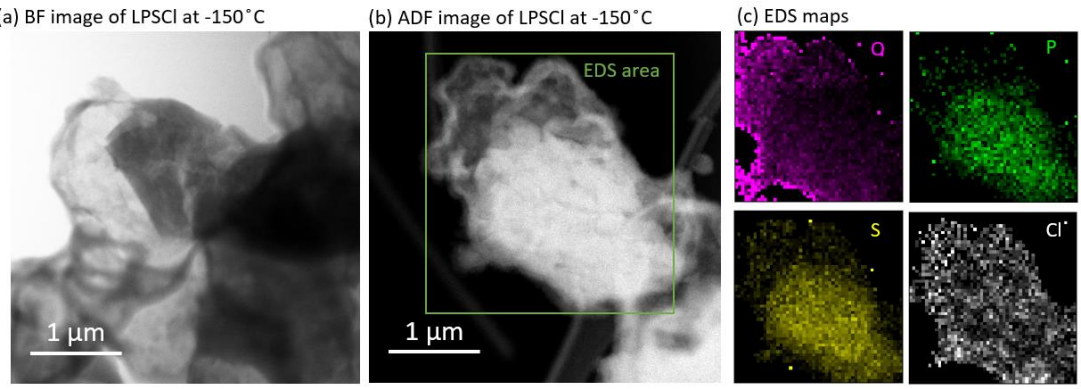


Figure 4.5: (a) BF image of LPSCl at -150˚C, (b) ADF image of LPSCl at -150˚C, (c) comparison of chemical composition in the ice layer and LPSCl area covered in ice. (Data acquisition credit to Dr. Weixin Song)

4.4 Beam Damage Study

4.4.1 Introduction

The TEM study of battery materials is often complicated by their susceptibility to radiation damage. Due to the materials' delicate crystal structures, they can be easily disrupted by the

high-energy electron beam. Furthermore, the operational similarities between the electron beam's interaction with the materials and the flow of electrons through the materials during battery cycling can lead to misinterpretations, where the effects of radiation damage might be mistakenly attributed to the electrochemical cycling process itself.

Thus, mitigating beam-induced damage becomes a crucial aspect of TEM studies on battery materials. Understanding the predominant radiation damage mechanisms is essential for developing effective strategies to minimise these effects.

Mechanism

Beam damage mechanisms can be categorized into knock-on damage and radiolysis, based on whether they result from elastic or inelastic scattering, respectively. [204]

Knock-on damage

Elastic scattering occurs when an incident electron is deflected by an atom nucleus due to Coulombic interactions without reduction in the total kinetic energy on the electron. However, as the incident is deflected by an angle θ, there will be a transfer of energy due to energy and momentum conservation as shown below:[205]

$$E = E_{max} sin^2 \frac{\theta}{2} = E_{max} \frac{1 - cos\theta}{2}$$

$$E_{max} = \frac{E_0(E_0 + 2m_e c^2)}{E_0 + (1 + m_e/M)^2} \approx \frac{2E_0(E_0 + 2m_e c^2)}{Mc^2}$$

θ – scattering angle

c – speed of light

E_0 – incident electron energy

M – nucleus mass

m_e – rest electron mass

E_{max} – maximum energy transfer (backscattered electron θ=180˚)

As suggested by the factor of $sin^2\frac{\theta}{2}$ in the equation, small angle deflections result in negligible amounts of energy transfer. However, with large angle scattering, if E_{max} exceeds E_d (threshold energy), the atom will be displaced into an interstitial position, leaving a point defect behind. [206] It has been suggested that if the incident beam energy E_0 is sufficiently low that E_d is not reached, knock-on damage can be prevented. E_d is affected by atomic number, bonding strength, crystal structure and atom position in bulk specimen. When high-angle scattering occurs near the specimen surface, atoms are more prone to escaping into the vacuum than into interstitial positions, although this requires more energy. This is referred to as electron-beam sputtering. [207] Hole drilling and specimen thinning are common results of knock-on damage.

Radiolysis damage

Radiolysis damage is caused by ionisation due to the inelastic interaction between an incident beam and the electron cloud surrounding an atom nucleus. Due the significantly lower difference in mass in electron-electron interactions compared to nucleus-electron interactions, the effect of the transferred momentum is much larger than in knock-on damage and can cause excitation of the outer-shell electrons. [204]

The process of radiolysis damage consists of electron excitation and the subsequent chemical bond recovery. The excitation phase occurs instantaneously as the material encounters the electron beam, disrupting chemical bonds and generating free radicals in organic substances, or electron-hole pairs in ionic crystals. These broken chemical bonds are unstable and can randomly relink, forming new bonding that deviate from the material's original structure. As the

electron dose accumulates, the material's crystalline structure progressively degrades, eventually leading to a uniformly amorphous state.

Sample heating

With inelastic scattering, kinetic energy of the incident beam can be converted to heat which causes localised heating in the specimen. Heating is more significant at higher current densities because it enables more inelastic scattering events. The current density in STEM with a convergent beam is significantly higher than that used in TEM with parallel beam at the same beam current is used because of the difference in the area the beam interacts with. However, interestingly, the observed temperature rise in STEM is only slightly higher than in TEM imaging. [204] This is due to the short exposure time for each beam position during a STEM scan, which gives time for heat to dissipate. In TEM the sample is continuously bombarded by the electron beam, causing heat to accumulate and leading to higher temperatures. Materials with good thermal conductivity like metals are less vulnerable to electron beam heating since heat can easily conduct away, but it can cause severe thermal degradation in organic materials and electrical insulators such as battery electrolytes even at low current density.

Electrostatic charging

Charging is a notable damage mechanism for TEM study of electrically insulating materials. It occurs due to escaped secondary electrons from incident beam-specimen interaction, leading to positively charged specimen surface. Charging can cause image distortions due to the deflection of the electron beam, which is influenced by the electric fields created by accumulated charges. Additionally, this charging can induce physical damage to the sample, such as bending or drifting.

Methods to Minimize Beam Damage

Acceleration Voltage Choice

There is no single set of EM parameters that are ideal for all kinds of materials. It is necessary to establish the dominant damage type to choose the most effective method of imaging. For example, accelerating voltage affects knock-on and radiolysis damage mechanisms in different ways. Knock-on damage can be reduced by lowering the voltage and can even be stopped entirely if the voltage is lower the energy threshold (E_d). On the contrary, the cross section of inelastic scattering increases with decreasing voltage, resulting in worse damage at lower accelerating voltages.

Critical Dose and Dose Rate Threshold

For beam-sensitive materials like organic compounds, the damage grows as the cumulative electron dose (electrons per unit area) increases while the dose rate (dose per unit time) has little impact: with the same accumulated dose, higher dose rates produce the same level of damage. In such cases, the critical dose—beyond which significant damage occurs—can be determined from the relationship between damage and total dose. The calculation of critical dose will be discussed in the following section.

But for most of the inorganic materials, which are more robust to beam damage, the dose rate has greater effect on the beam damage. it is commonly found that the damage increases with higher dose rate, which are attributed to the notable temperature rise and thermal decomposition, [208] or the poor electrical conduction and charging effect. [209]

Cryogenic-EM

Unlike knock-on damage in which there is an energy threshold under which it will not occur, radiolysis happens immediately when a specimen is exposed to an incident beam. A common way to reduce radiation damage is to lower the temperature during TEM experiments. It has been reported that by keeping the specimen at -173˚C, the tolerance to electron dose increases by a factor of 5-7, [210] and mass loss decreases by a factor of 10-100. [211] Although the cross section of inelastic scattering is not reduced at lower temperatures and bonds breaking cannot be avoided, the key mechanism behind the improvement in resistance to radiation damage is the reduced mobility of atoms, so they are prevented from leaving their original position.

Post-acquisition Processing

The post processing algorithm electron ptychography discussed in Chapter 3, can correct residual lens aberration after data acquisition. Therefore, by using electron ptychography, electron dose and radiation damage can be minimised by lowering the beam current and exposure time before data acquisition. Low dose imaging using electron ptychography has been applied to Li-rich cathode materials to track structural changes at different states of charge. The position of Li and O atomic columns have been successfully located, while surface damage such as amorphisation and surface reconstruction has been significantly reduced. [212]

Quantification of Beam Damage

HAADF imaging

As described above, sample thinning or hole drilling can be observed when atoms are deflected into the vacuum. Therefore, if loss of mass is quantified, the extent of radiation damage can be extrapolated. The software Absolute Integrator can calculate the absolute scattering cross-

section from STEM HAADF images. [213] However, there are some drawbacks to this method. Firstly, it assumes that all radiation damage is in the form of beam electron sputtering, which may not be true as radiolysis can also induce mass loss through the formation of volatile products that are subsequently released into the vacuum chamber. Since radiolysis-related mass loss varies with the material, this method's applicability in quantifying mass loss is constrained to be relative to specific samples. Additionally, it is hard to obtain accurate quantification of mass loss. For example, hydrocarbon contamination on specimen surface can cause mass gain which will affect the accuracy of the mass measurement.

Diffraction Pattern

As mentioned in the above section on radiolysis, ionisation and reconnection of bonding reduce the degree of crystallinity. DPs are sensitive to periodicity in crystal structure and therefore can be used to estimate the degradation of crystallinity and radiation damage. The critical dose D_c, represents the maximum electron dose a radiation-sensitive material can withstand before significant loss of structural information. The critical dose Dc is quantified by the decay of a chosen feature in DP to 1/e (around 37%) of its original intensity. [214, 215]

Using DPs as an approach to measure radiation damage was proved to be an effective method by Henderson *et al.* Substantial blurring of diffraction spots can be observed when the molecular structure is destroyed by radiation. [216]

Electron Energy Loss Spectroscopy

EELS offers another opportunity to quantitatively measure radiation damage, by evaluating changes in specimen thickness, elemental composition, and bonding characteristics. [217, 218]

The application of this technique has been highlighted in studies of radiation-sensitive materials, such as polyethylene terephthalate (PET), where low-loss EELS spectra provided insights into the extent of beam-induced alterations. [219, 220] Similarly, the electron beam damage in CaF_2–

Al_2O_3–SiO_2 glass has been studied through the Ca L_{23} and O-K edges in EELS, detecting subtle changes in elemental and bonding states due to radiation. [221]

4.4.2 Results and Discussion

To study beam-sensitive LPSCl, it is crucial to first understand the mechanisms of beam damage so that the experimental settings can be optimised. This section details our attempt to monitoring changes in crystallinity with accumulating electron dose. Continuous DPs were obtained at both 200kV and 300kV.

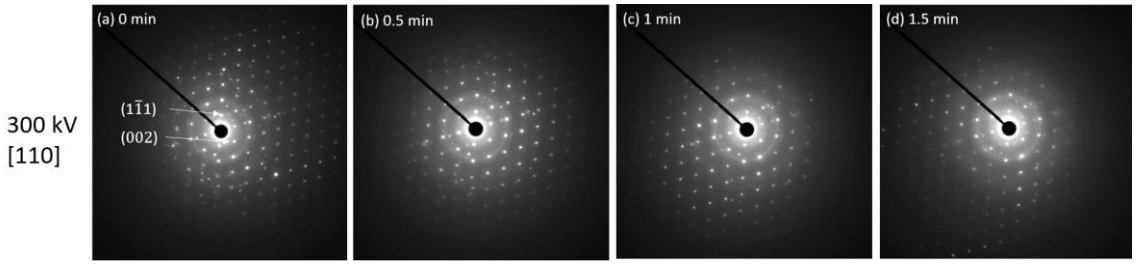


Figure 4.6: Diffraction pattern of LPSCl at 300kV, zone axis of [110].

At 300kV with a dose rate of 7.11 e/Å²/s, DPs were captured at a rate of 0.3s per frame over a period of 4.5 minutes. Notably, a shift in the Laue zone from the top right corner to the bottom left can be observed in Figure 4.6a-d, indicating particle tilting during observation. This tilting is attributed to the effect of charging on the electrically insulating solid electrolyte. The accumulated negatively-charged electrons on the particle surface are repelled by the incident electron beam through the Coulomb force.

As introduced earlier, the critical dose, D_c, can be quantified based on the decay in diffraction spot intensity. The relationship between diffraction spot intensity (counts) and accumulated dose (e/Å²) is shown in Figure 4.7. However, the peak within the first 500 e/Å² complicates the estimation of D_c for crystallinity decay, as this peak results from charging-induced tilting.

Beyond the charging-induced peak, the intensity of the diffraction spots remains relatively stable as shown in Figure 4.7a. It is worth noting this is strongly influenced by the choice of mask size. Because of the particle rotation during data acquisition, a large mask size (50x50 pixels) was initially employed as shown by the red squares in Figure 4.7c and e. To illustrate the effect of mask size on diffraction spot intensity estimation Figure 4.7c and e compares the first and last DPs of LPSCl. The summed intensity in the marked area changes from $2.1x10^7$ to $1.7x10^7$. However, a diagonal line profile across the diffraction spot reveals an intensity ratio of 1:3 in Figure 4.7d and f, indicating that the large mask did not effectively capture the decay in crystallinity. This is attributed to an increase in background signal from amorphisation, which results in the overall intensity appearing stable.

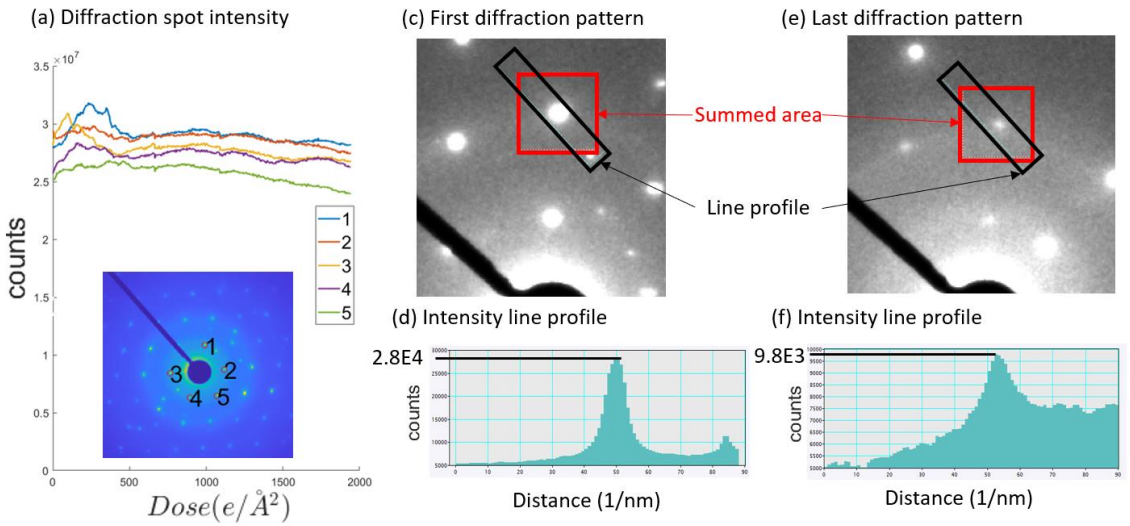


Figure 4.7: (a) 300kV diffraction spot integrated intensity change plotted against accumulated dose (b) diffraction pattern with numbered diffraction spot (c)the first diffraction pattern and (d) the last diffraction with masked area labelled in red square and line profile at diagonal direction at (d) and (f).

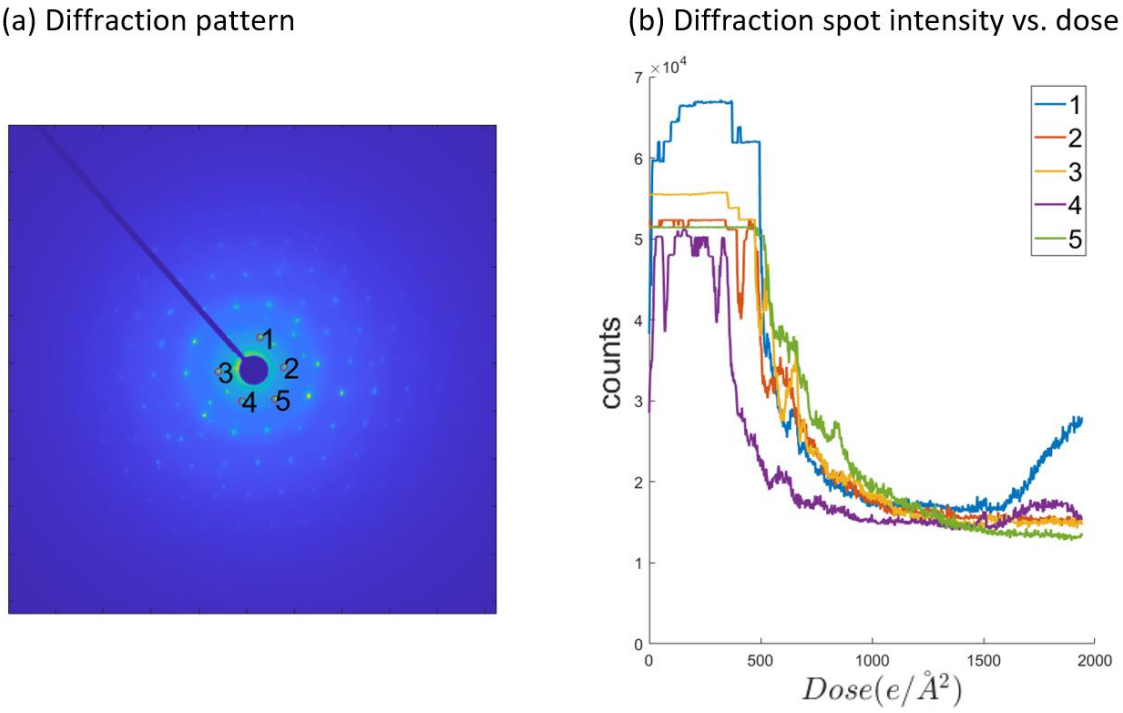


Figure 4.8: (a) Diffraction pattern at 300kV (b) diffraction spot maximum intensity change plotted against accumulated dose

Using the maximum intensity of each diffraction spot plotted against the accumulated dose, as depicted in Figure 4.8, offers a clearer representation of the intensity decay than the summed intensity method. However, particle tilting still introduces an initial peak within the first 500 e/Å². This peak remains indistinguishable from the intensity decay attributed to amorphisation. The critical dose of LPSCl considering both charged-induced tilting and amorphisation can be roughly estimated to be in the order of 10^2 e/Å² at 300kV.

To rigorously investigate the predominant beam damage mechanism, experiments were conducted using a similar beam dose rate of 9.47 e/Å²/s at 200kV. Ideally, comparing the critical dose of identical diffraction spots at the same zone axis across different beam voltages would elucidate the dominant damage mechanism. A higher critical dose at increased voltage would suggest radiolysis as the primary concern, recommending the use of higher beam voltages for such studies. Otherwise, knock-on damage dominates and the beam voltage should be lower.

Nevertheless, the fast DP spot intensity decay of the sample does not allow tilting to align the zone axis, necessitating data acquisition by moving the sample stage in diffraction mode and recording images once DPs appeared. Despite these challenges, some DPs were successfully captured at both 200kV and 300kV with the same zone axis, as shown in Figure 4.9. Yet, the persistent issue of charging-induced particle tilting, leading to diffraction spot intensity decay, remains indistinguishable from the effects of amorphization.

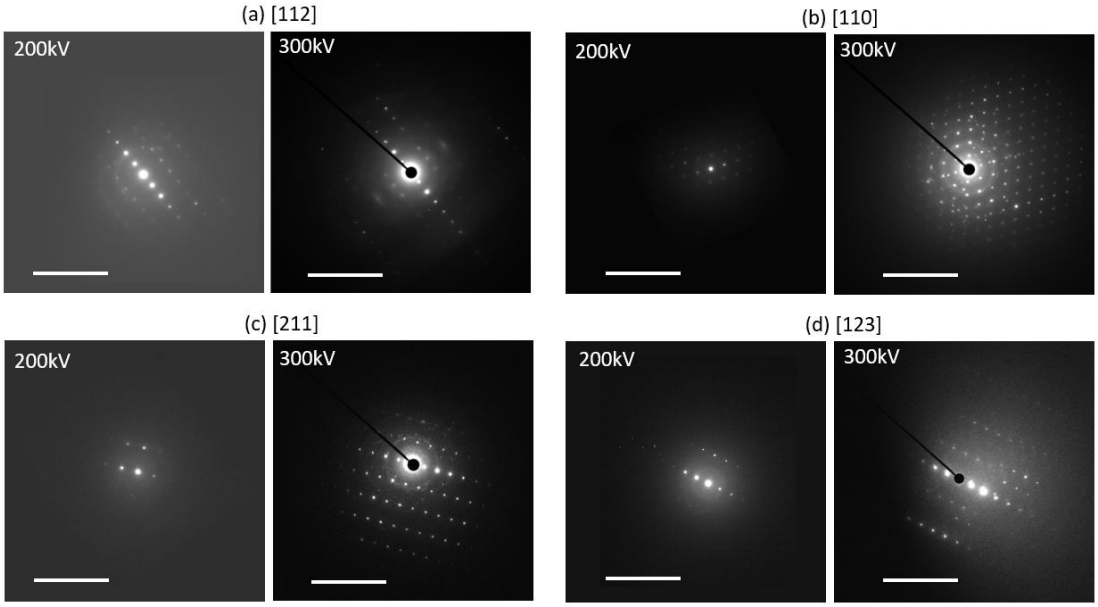


Figure 4.9: DP of LPSCl at 200kV and 300kV on zone axis of (a) [112], (b) [110], (c) [211], (d) [123].

A technique which is commonly used to reduce charging of electrically insulating materials is conductive coating the specimen. However, the process itself can be damaging, particularly for air- and reactive-sensitive materials like LPSCl. Maintaining the near-natural state of the material during beam damage studies is essential. Blanking the beam between acquisition to allow accumulated charge to dissipate is another method which could mitigate the charging effect. Unfortunately, the charging-induced particle tilting persists upon beam re-engagement, making this solution ineffective.

A potential solution could involve encapsulating the particle with graphene layers, which have excellent electrical conductivity, to mitigate the charging effect and also physically prevent

tilting. Graphene encapsulation has also been found to prevent knock-on and radiolysis damage, and it allows the application of higher electron doses for high-resolution imaging and chemical analysis. [222] However, the progression of this project was halted, due to time constraints exacerbated by unforeseen delays. The onset of the Covid pandemic in my first year delayed the TEM training and experiments to the second year. By the time I finished the air exposure study and obtained some results for the beam damage study, it was already the beginning of my third year. Given that the anaerobic transfer procedure has been established for the future solid-state battery study in TEM and the primary scientific question into the interfacial redox reaction remained unexplored, while recognising that addressing the tilting issue would demand a significant investment of time, I decided to prioritise investigating the interface between LPSCl and NMC622.

4.5 Conclusions

In this chapter, the effects of air exposure on the morphology, elemental distribution, and elemental ratio of the air-sensitive solid electrolyte LPSCl have been thoroughly explored. The key achievement was the establishment of an anaerobic transfer protocol from the glovebox to the TEM, laying a foundational step for future studies on interfacial phenomena. Moreover, the beam damage mechanisms in LPSCl has been investigated by comparing diffraction patterns obtained under similar dose rates and identical zone axes at both 200kV and 300kV. Despite these efforts, the intrinsic electrically insulative characteristics of the electrolyte presented substantial challenges, notably particle tilting, which complicated the quantification of the critical dose for beam damage. This made further study unfeasible with the current experimental setup.

The next chapter will shift the focus onto the preparation of interface lamellae for TEM analysis.

Chapter 5 TEM Specimen Preparation Methodology for Solid-State Batteries

5.1 Introduction

Analytical STEM is a powerful technique in acquiring high energy resolution information at high spatial resolution. However, to achieve an optimal signal-to-noise ratio (SNR) in STEM characterisation, the sample must be thin enough to transmit electrons. The vast majority of materials are not naturally electron transparent, and therefore various sample preparation techniques have been developed for STEM.

The methods for STEM sample preparation can be broadly categorised into mechanical cutting and grinding, electropolishing, and ion beam milling. Mechanical thinning is the most basic method where the sample is sliced by sharp blade or finely ground to achieve the desired thickness. During electropolishing, samples are immersed in an electrolyte then an electric current is applied, resulting in uniform thinning through controlled electrochemical dissolution. Finally, an energetic ion beam is used in ion beam milling to sputter materials away at a specific site.

Each STEM sample preparation method has its advantages and limitations. The method should be chosen based on the analytical objectives of the study and also the sensitivity of the material to retain their intrinsic properties for STEM study. For example, electropolishing is not suitable for battery materials because artefacts induced in electrochemical dissolution may be mixed up with the effect from cycling behaviour.

Our primary objective is to study the interfacial redox reaction between NMC622 and LPSCl through core-loss EELS. The ideal specimen is a uniformly thin slice of NMC622 and LPSCl with a sharp interface, so that the EELS mapping can capture the depth dependent interfacial redox reaction.

The highly reactive nature of solid-state battery materials, especially towards water and air, requires the whole sample preparation process is conducted in a dry and anaerobic environment. This restricts the choice of equipment to those either installed within gloveboxes or those that can facilitate anaerobic transfer.

In this chapter, the exploration of sample preparation from manual grinding to ball milling and finally cryogenic plasma focused ion beam (cryo-PFIB) milling will be discussed. The sample preparation-induced artefacts for each method are measured and compared. The applications of cryo-PFIB in studying cathode materials at various states of charge while preserving the NMC622/LPSCl interface is demonstrated.

5.2 Manual grinding

Manual grinding stands out for its simplicity in operation, as no solution and post-processing is required. In the Ar-filled glovebox, materials were ground with a mortar and pestle. The resulting material was scraped from the pestle head onto a lacey Cu mesh grid, which was loaded onto the TEM vacuum transfer holder for further study.

However, analysis of the particle size shows that it was not effectively reduced. Commercial NMC622 powder with particle size of around 1um was used throughout the project. Manual grinding can easily vary in grinding force and speed during the operation, leading to a wide distribution of particle sizes. As a result, although few small particles can be observed after manual grinding in Figure 5.1a, most of the particles' size remain unchanged. EDS maps of Ni and S from NMC622 and LPSCl respectively are used to highlight the interface. It can be observed from Figure 5.1b and c that the NMC622 particle is overlapping with an LPSCl particle. The challenge lies in ensuring a distinct, non-overlapping and thin interface from particle grinding. Moreover, the comparison of SNR in core-loss EELS in Figure 5.1d and e show the ground material exhibits a variable thickness profile across a single particle. The plasmon peak

corresponds with the interaction of incident beam with valence electrons in the specimen. In thick regions, the multiple scattering effect becomes significant, causing a pronounced plasmon peak that overwhelms the edges in the core-loss EELS spectrum. This substantially complicates the quantification process in EELS.

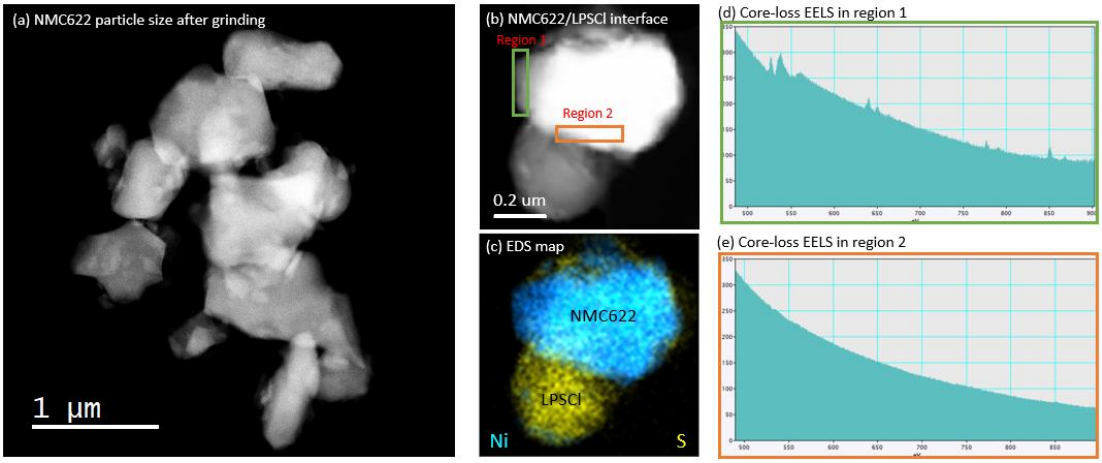


Figure 5.1: (a) NMC622 particles size and morphology after manual grinding with mortar and pestle, (b) ADF image of NMC622 mixed with LPSCl in mortar, the interface is highlighted in (c) merged EDS map of Ni (blue, from NMC622) and S (yellow, from LPSCl), core-loss EELS collected from (d) thin edge of NMC622, marked in green, (e) interface with LPSCl, marked in orange.

The difficulties in obtaining a consistent thickness, reduced particle size, and defined interface make mortar and pestle grinding incompatible with the requirements for this study.

5.3 Ball Milling

Ball milling is commonly used for particle size reduction, powder mixing and synthesis in Li-ion batteries. [223-227] The improvement in size reduction and mixing could increase the chance of observing a well-defined interface. The materials are added into a jar with grinding media made from wear-resistant materials (typically zirconia or stainless steel). The jar is then sealed and undergoes rapid rotation on a milling machine. The motion induces collisions between the milling balls, material and the wall of the jar. This process not only reduces the particle size but

also generates substantial heat leading to localised heating. Therefore, ball milling may be considered as a mechanochemical process.

Here, the materials were ball milled for 6 h at 500 rpm, using a ball mill inside an Ar glovebox. An improvement in particle size reduction can be seen from the peak broadening in the XRD in Figure 5.2b. The ADF in Figure 5.2a demonstrates the significant improvement over manual grinding as the particle size is now down to 100 nm.

However, the ball milling also leads to degradation and amorphisation of the material. The overall decrease of XRD peak intensity is observed on the ball milled NMC622, as shown in Figure 5.2b, which suggests the ball milling process amorphised the NMC622/LPSCl and destroyed the interface of interest. Attempts were made to restore crystallinity through annealing, but after 1 hour at 600˚C under Ar, while the peaks are much sharper, the XRD pattern demonstrates a significant alteration in the crystal structure compared to the original state.

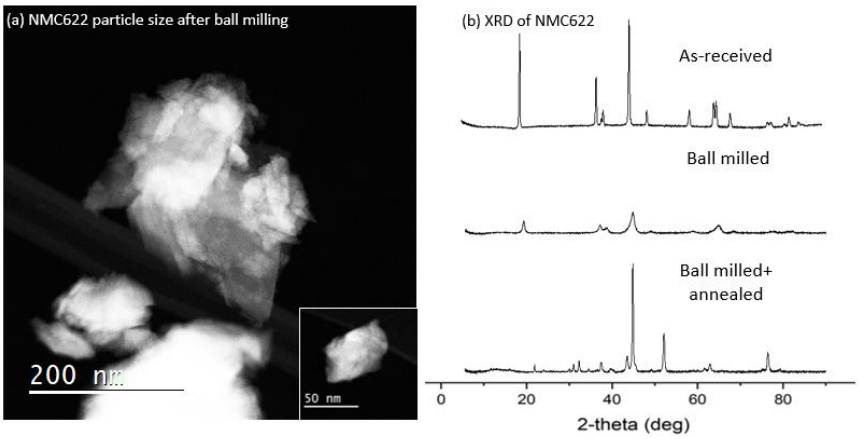


Figure 5.2: NMC622 particles size and morphology after ball milling, (b) XRD of NMC622 at as-received state, after ball milling and ball milling + annealing

Achieving a balance between particle size reduction and controlled structural degradation through ball milling method would require systematic investigation of the ball milling and annealing conditions. However, similar to manual grinding, ball milling cannot fundamentally

address issues such as variations in thickness profiles at particle edges and particle overlap in interface studies.

This exploration directs us to a technique that is most sophisticated but also with the unique benefits of site-specific fine control – focused ion beam (FIB).

5.4 Focused Ion Beam

5.4.1 Introduction

FIB has become indispensable in materials characterization and sample preparation. FIB was initially developed for the modification and analysis of integrated circuits in semiconductor devices due to its high lateral resolution and the ability of both sputtering and deposition. [228] Around 1990, FIB was incorporated into TEM specimen preparation. Its unique site-specific control led to active exploration of FIB application in scanning electron microscopy (SEM)/TEM characterisation in various areas of material science and pushed development of FIB techniques further. [229-239]

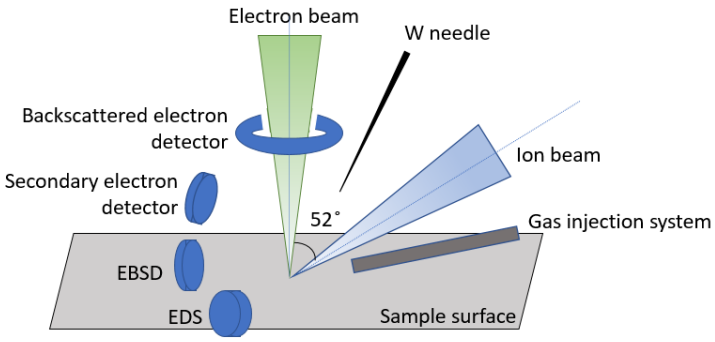


Figure 5.3: Diagram of FIB-SEM dual beam platform with analytical functions

A typical FIB system comprises several crucial components: firstly, an ion beam is generated and accelerated from the ion source, then the beam is shaped by passing through a set of electrostatic lenses and apertures. The location of the ion beam on the sample surface is controlled by scan coils. The energetic ion beam strikes the specimen surface and sputters atoms

away. During the interaction between ion beam and sample, secondary electrons, which are low-energy electrons emitted from within 5 nm from surface, are generated. Using a secondary electrons detector in FIB can monitor the progress during milling. Besides, gas injection systems (GIS) and micromanipulators are commonly used to allow deposition and TEM lamella preparation.

Modern FIB systems typically incorporate an SEM column, forming a FIB-SEM dual beam platform as shown in the schematic diagram in Figure 5.3. SEM is a well-developed characterisation tool in both scientific research and industrial application. It uses a focused electron beam to scan over the sample surface, generating various signals. Each signal, captured by specific detectors, conveys distinct types of information. The most common SEM characterisation functions include high-resolution surface morphology imaging using a secondary electron detector, compositional contrast imaging via a backscattered electron detector, chemical element mapping with EDS, and crystallographic analysis through electron backscatter diffraction (EBSD). By integrating SEM's comprehensive characterisation capabilities with FIB's site-specific modification ability, the FIB-SEM dual-beam platform enables real-time feedback in micro/nano-structuring, internal structure analysis, and 3D reconstruction. [240-243]

Ga FIB and Xe Plasma-FIB

Ga^+ is the conventional and still the most common ion choice for FIB due to its low melting point and high vapor pressure at low temperature. This ensures stable ion emission when using liquid metal ion source. However, while it offers precise milling Ga ions can interact with certain materials, leading to Ga implantation and undesirable structural changes.

Due to these challenges, xenon plasma has emerged as an alternative to Ga. The Xe Plasma FIB offers higher sputtering rates due to the larger atomic mass of Xe and can achieve higher beam currents by using an inductively coupled plasma (ICP) source, thus enabling more efficient

material removal. In addition, Xe PFIB produces a thinner amorphous layer on the sample surface than Ga FIB, since the heavier ions have a smaller interaction volume and are therefore lower penetration depth. [244-246] Finally, being a noble gas, Xe is chemically inert, reducing the chances of chemical contamination. [245]

Xe PFIB shows promising advantages over Ga FIB in terms of higher throughput, less structure damage and chemical contamination. Nevertheless, at low energy and low current conditions (below 20nA), [247] the Xe ion beam is broader than Ga. This limits its spatial resolution and causes curtaining artefacts during milling. This drawback makes TEM sample preparation challenging; the final step requires low energy and low current polishing, during which these issues become more acute.

TEM Lamellae Preparation Methods

There are two popular approaches to prepared TEM lamellae using FIB.

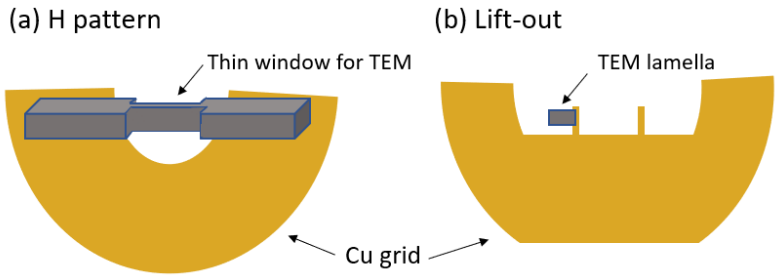


Figure 5.4: Schematic diagram of (a) H pattern and (b) lift-out method FIB lamellae.

The original FIB-TEM lamellae method was proposed by Kirk *et al.* in 1989. [233] This method allows the sample to be thinned to the desired thickness while preserving its original location. The finished sample looks like a capital 'H' in FIB, therefore this method is called the 'H' pattern method as shown in Figure 5.4a.

However, preliminary sample preparation is required for this method and the lamellae prepared by the H pattern method have limitations on tilting angle in the TEM. To overcome these issues, a new method of 'lift-out' was proposed by Overwijk *et al.* [248] As suggested by the name, the lamellae is lifted out from its original location and then transferred to a TEM grid during the process. Both methods were used in this study, details will be discussed later in this chapter with examples.

Overall, the unique advantages of PFIB in preparing site-specific TEM samples with nanometre precision are especially beneficial for composite solid-state battery materials, which have particularly mechanically weak interfaces. However, as discussed previously PFIB can also induce contamination and structure degradation which will interfere the study of nature state of the material. Solid-state Li-ion batteries are highly susceptible to hydrolysis reaction [249-251] and energetic beam damage. [252, 253] Therefore, it is necessary to systematically study PFIB damage on these materials to ensure sample integrity is preserved while achieving the desired thickness and quality necessary for TEM studies.

A cryogenic temperature has been reported to successfully minimise the damage induced in sample preparation and TEM characterisation. [254-256] The effect of applying a cryogenic stage on PFIB for battery STEM sample will be discussed.

5.4.2 PFIB Damage Study at Ambient and Cryogenic Temperature

In the previous section, the superior milling efficiency and reduced structural and chemical damage offered by Xe PFIB compared to the traditional Ga FIB has been highlighted. For this study, a FEI Helios G4 Xe PFIB, equipped with a cryogenic stage to further minimised the ion beam damage was used. It is worth noting that the literature on PFIB-induced damage in TEM samples of solid-state Li-ion battery materials is limited. My research aims to fill this gap by

examining Xe PFIB-induced damage on the cathode material NMC622, under both ambient and cryogenic conditions.

At cryogenic temperatures, Pt or W deposition cannot be used in the FIB. Because the sample surface acts as a cold finger once cooled down, the organo-metallic gas precursor ejected from GIS will soon condense all over the sample surface, instead of being deposited by the ion beam. While connection via redeposition is sometimes used, [257, 258] connections made by redeposition of the sputtered material are very delicate, leading to a lower rate of success in sample preparation. The other option is to warm the sample back up to room temperature to deposit Pt as normal for a lift-out. But the sample must then be cooled again to cryogenic temperatures for the final polishing step, before again being warmed up for transfer to the TEM. This additional thermal cycle raises questions about the effects of repeated cooling and heating on the sample, and thus the H-pattern method, which allows the sample to undergo just one thermal cycle, was initially adopted in this study.

Method

The workflow begins in the Ar-filled glovebox where the battery is cycled and stored. The sample was anaerobically transferred into the PFIB using the Gatan iLoad vacuum transfer system, and into the STEM using the JEOL Be Double-tilt TEM vacuum transfer holder. Details of each step are presented below:

In the H pattern method, sample preparation in the PFIB and analytical characterisation in the STEM take place on the same TEM grid. Given the different beam orientations between PFIB (ions parallel to the grid) and TEM (electrons perpendicular to the grid), it is essential to ensure the correct alignment of the sample, especially for interface samples.

NMC622 and LPSCl are both available as commercial products in black and white powders respectively. To enable ionic conductivity in the cathode, a composite of NMC622 and argyrodite are used. They were mixed using a mortar and pestle and then the mixed powder was pressed into a pellet against LPSCl under 500 MPa for 3 mins, forming a 2-layer structure as shown in Figure 5.5a. The pellet was then broken into small pieces and a fragment with a thin tip was mounted onto half Cu aperture grid. Due to the limited Z height adjustment (±100 um), X and Y location in atomic resolution STEM, and also the limited tilting angle of the double-tilt TEM vacuum transfer holder (tilt Y: ± 5˚). The precise control of sample location on the grid is crucial that the thin tip must be centrally positioned within the grid hole of the TEM holder with diameter of 3mm, and also as close as possible to the grid plane. Apart from the refined requirements of the sample location, the orientation of the sample must be carefully controlled as well. With the aim of studying the depth dependent interfacial reaction, we need the interface plane to be perpendicular to the grid plane and therefore the fragment is oriented sideways on the grid, as illustrated in Figure 5.5b. To meet these requirements regarding the sample geometry, location, and orientation, the chosen fragment was carefully picked up with a No.5 diamond tweezer. It was then dipped into silver dag for mounting onto the grid. The grid was clamped in FIB vice grid holder to stand upright.

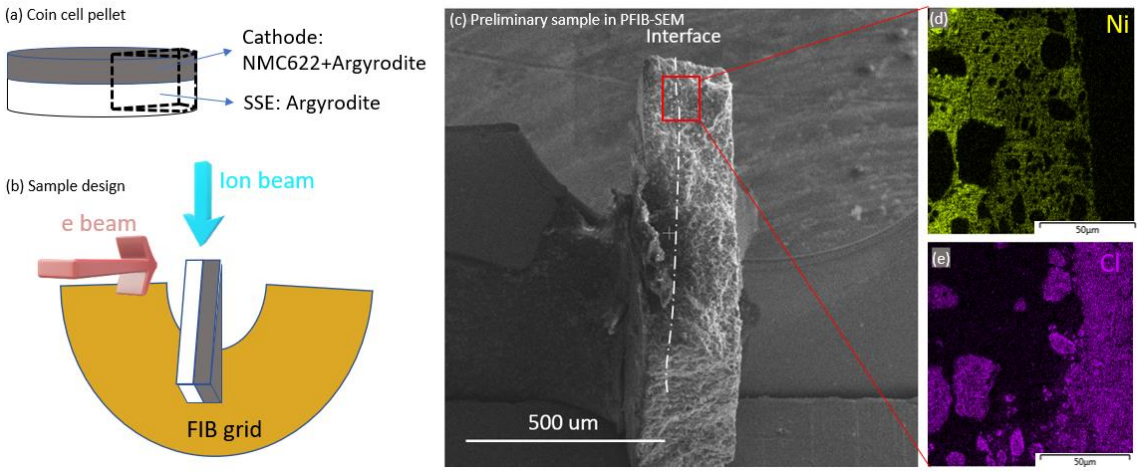


Figure 5.5: Schematic diagrams of (a) cathode/SE pellet and (b) sample design for PFIB milling (c) secondary electron image of the sample design, in the highlighted area EDS maps of (d) Ni (yellow) and (e) Cl (purple) shows the interface between cathode and LPSCl. (PFIB milling and EDS data acquisition credit to Dr.Alex Sheader)

The SEM stub was transferred to the PFIB via the iLoad system in an Ar atmosphere. The FIB stage was cooled down to -100°C with liquid nitrogen for milling. Due to the limited Z height adjustment in STEM, the electron transparent window should be made as close as possible to the grid plane, and therefore a smaller milling depth should be used on the grid-facing side. Due to the installation of the cryogenic stage and the brittleness of materials at cryogenic temperature, actions like rotation, tilting and large movement are forbidden once cooled down. Therefore, we are limited to monitoring the milling progress from a single angle, which means the milling and polishing of the lamella's opposite side must be carried out without visual observation. The lamella was then transferred back to glovebox on the same grid with the same holder. The process of thinning the sample down is visualised in Figure 5.6 a-c.

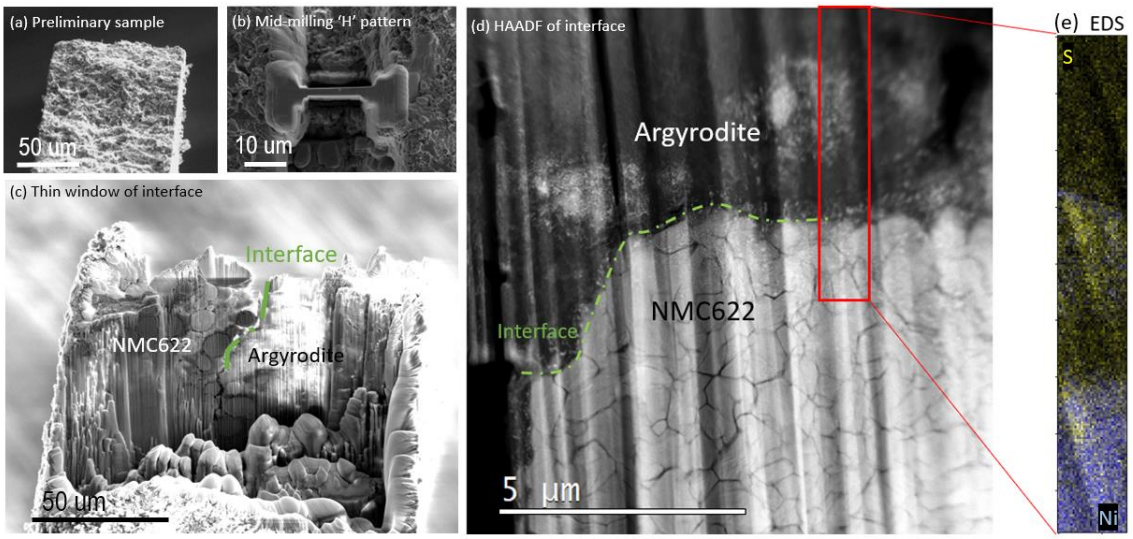


Figure 5.6: (a) Preliminary sample prepared for PFIB milling, (b) top view of lamella during milling, an 'H' shape is observed, (c) thin window of NMC622/LPSCl interface (d) HAADF image of the interface and (e) merged EDS map of S (yellow) and Ni (blue) (PFIB milling and EDS data acquisition credit to Dr.Alex Sheader)

In the glovebox, the grid was loaded onto the TEM vacuum transfer holder and then transferred to the STEM as shown in the HAADF image in Figure 5.6. Using both the EDS map of S from LPSCl and Ni from NMC622, and the HAADF image contrast, the interface can be located.

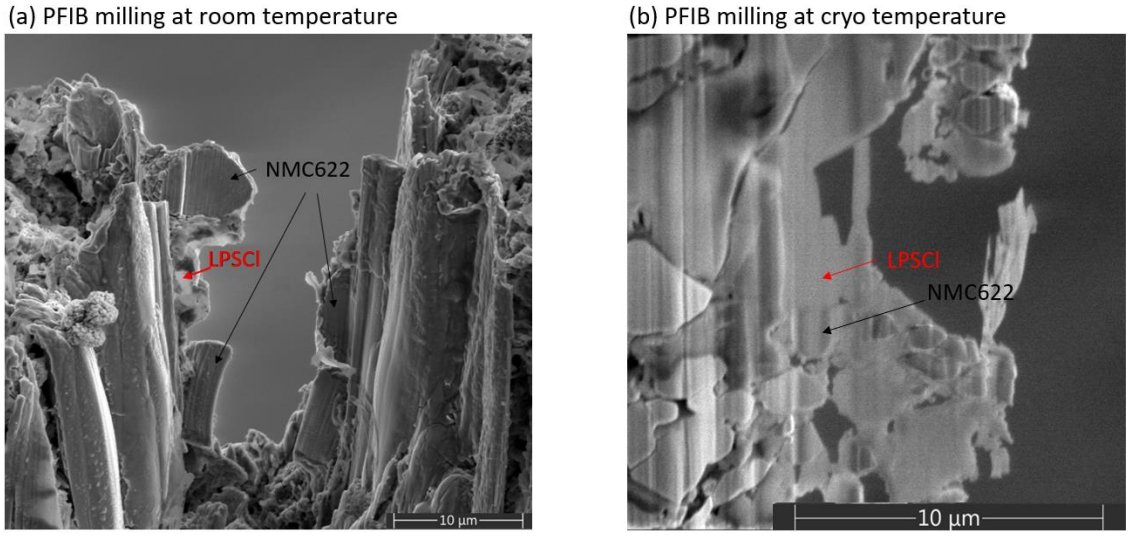


Figure 5.7: PFIB milling on NMC622/LPSCl sample (a) at room temperature, (b) at cryo temperature.

At room temperature, LPSCl is milled significantly faster than NMC622 under the same ion beam conditions. It is common that, before achieving the desired thickness for NMC622, the adjacent

LPSCl has already vanished as shown in Figure 5.7a. The application of cryogenic temperature is helpful in minimising the milling rate gap and producing an interface with a consistent and uniform thickness as depicted in Figure 5.7b. The improvement in milling performance resulting from lower temperatures suggests that the high milling rate of LPSCl at room temperature is primarily due to localised heating from ion beam-sample interactions. Consequently, cooling is an effective strategy for mitigating the localised heating and reduce the milling rates difference.

Figure 5.8 shows a cryo-PFIB milled NMC622/LPSCl interface lamella, and the EDS map of S and Ni in Figure 5.8b and c show the clear interface without overlap. Figure 5.8d is the horizontal line scan of the intensity in the highlighted area Figure 5.8a. The ADF intensity is linearly proportional to the thickness while the averaged atomic number remains unchanged. Therefore, ADF intensity can be a rough estimation of the thickness profile of same material in one image. The ADF intensity of NMC622 and LPSCl area are both relatively stable suggesting a uniform thickness of both materials.

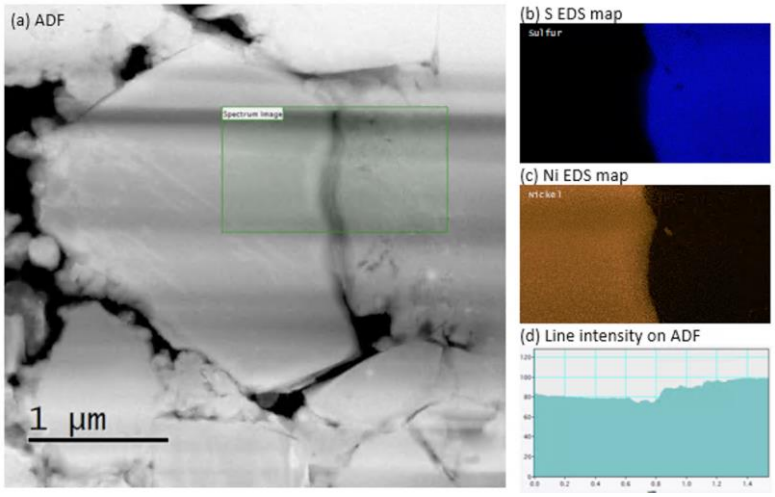


Figure 5.8: (a) ADF image of cryo-PFIB milled NMC622/LPSCl interface, EDS map of (b) S and (c) Ni in the highlighted area, (d) horizontal line scan of intensity of the highlighted area in ADF.

Further atomic-resolution ADF imaging and core-loss EELS were subsequently used to study the microstructure and oxidation state respectively, and will be discussed in depth in the following sections.

Structural Changes

The microstructure of NMC622 consists of alternating layers of Li, TM ions and O. This layered structure plays an important role in the electrical performance by providing high Li mobility in NMC which leads to high-rate capability. However, it was found that the layered structure can degrade to spinel and rocksalt when the TM ions and Li ions swap positions as illustrated in the schematic crystal structure and experimental data of the 3 structures from literature in Figure 5.9. While the Li ion sites are gradually occupied by TM ions, the Li mobility is reduced and battery performance deteriorates, for example: impedance increase and capacity decay. [259-266]

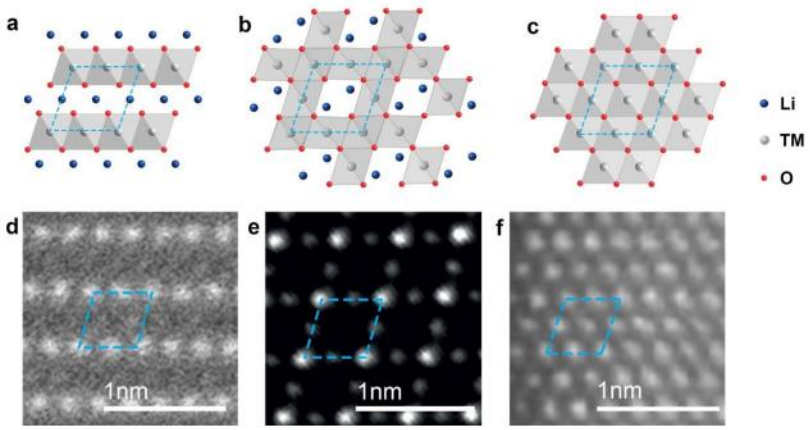


Figure 5.9: Schematic crystal structure of (a) layered, (b) spinel, (c) rocksalt phase; STEM -HAADF images of (d) layered, (e) spinel, (f) rocksalt phase. [267] (Reprinted from Zhang H, Liu H, Piper LF, Whittingham MS, Zhou G. Chemical reviews. 2022 Jan 13;122(6):5641-81. Copyright 2022. With permission from American Chemical Society.)

To study the ion beam-induced damage, the microstructure of pristine NMC622 prepared by cryo-PFIB and ambient temperature PFIB are compared to the as-received NMC622 using HAADF imaging. HAADF images have contrast determined only by mass-thickness, and therefore for a sample of approximately uniform thickness, atomic number dominates in image contrast. Because TM ions are much heavier than Li and O, TM overshadows the visibility of Li and O ions in HAADF. Consequently, only TM layers can be observed in the Figure 5.10a of as-received pristine NMC622 which has not be ground or milled.

Figure 5.10b and c show pristine NMC622 prepared by the H pattern method at cryogenic and ambient temperature respectively. From bottom to the top of the images, atoms start showing up in between the TM ion layers towards the particle surface (highlighted with dashed lines). This is a result of the energetic Xe ion beam causing cation mixing and altering the microstructure of NMC622. By measuring the thickness of the rocksalt layer on the surface of NMC622, the ion beam damage can be quantified. In samples prepared at cryogenic temperatures, the damage layer can be minimised to merely 2.5nm (± 0.5nm from 4 datasets.) on the surface, while at ambient temperature the damage layer is more than twice the depth at around 5.8nm (± 1.1 from 3 datasets.). The minimised sample preparation damage is important to highlight the effect of interfacial reaction with LPSCl in the further study, and not mix it up with ion beam damage.

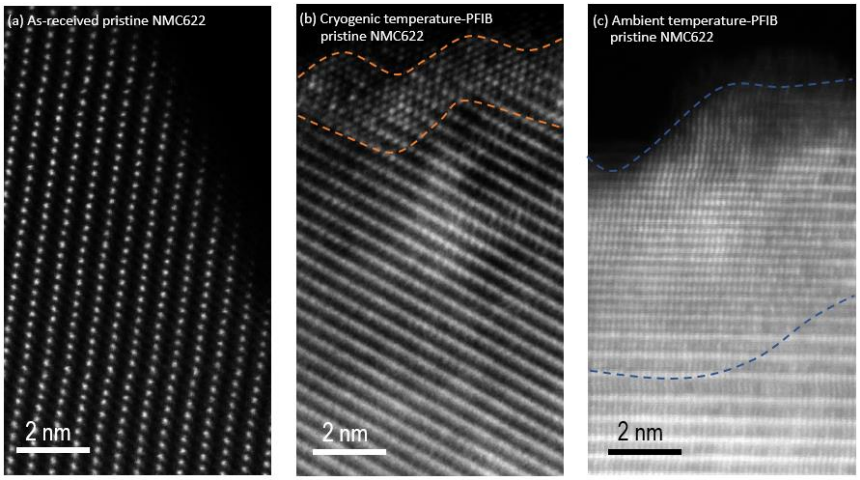


Figure 5.10: HAADF images of pristine NMC622 (a) at as-received state, (b) after cryogenic-temperature PFIB milled, (c) and after ambient-temperature PFIB milled.

Chemical Changes

The understanding of the ion beam damage can be further enhanced by using EELS to study TM ions' oxidation state change. The $L_{2,3}$ white lines in core-loss EELS arise due to the excitation of 2p electrons into unoccupied 3d orbitals. The energy shift and fine structure changes are closely

related to the vacancy in 3d orbitals and therefore the oxidation state of 3d transitional metal ions.

Dual-EELS were acquired in the same areas as shown in Figure 5.10b and c (and reproduced in Figure 5.11a and c for clarity) to correlate the structure degradation with oxidation state changes of O and the TM.

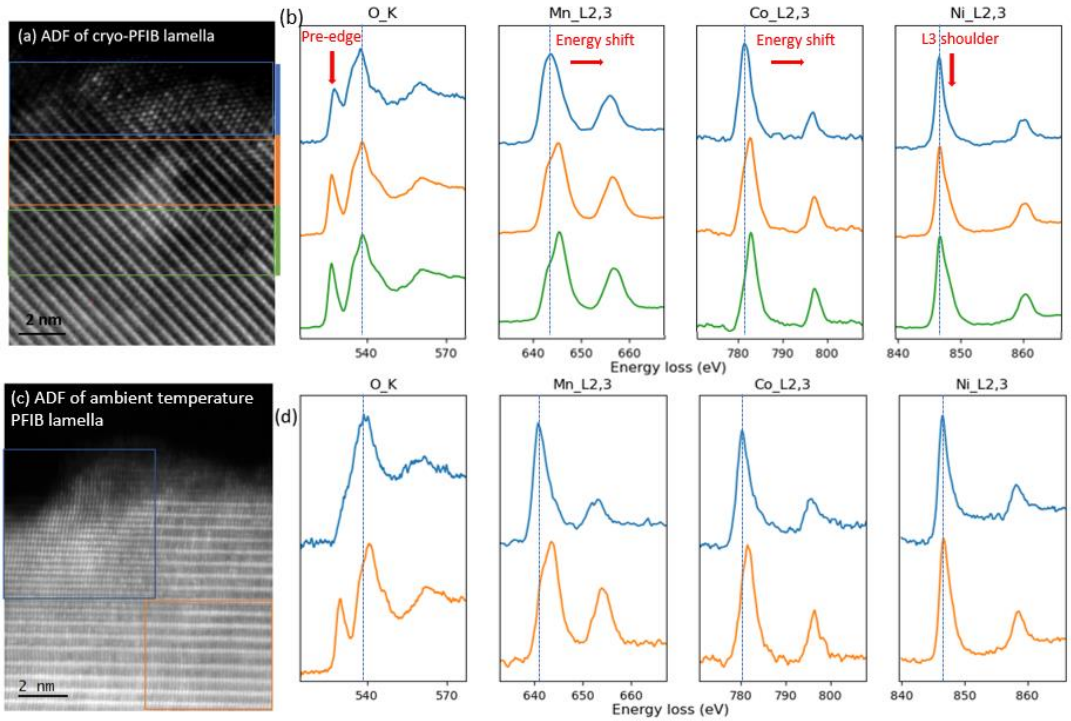


Figure 5.11: HAADF images EEL spectra of pristine NMC622 that is (a)(b) cryo-PFIB milled, (c)(d) ambient-temperature PFIB milled. Spectra are integrated across the area highlighted in the same colour.

In Figure 5.11, spectra integrated from the area highlighted in same colour are compared. The changes in the fine structure of the O-K, Mn-$L_{2,3}$, Co-$L_{2,3}$ and Ni-$L_{2,3}$ edges showing the oxidation states of different structures. For O-K edge, the pre-edge at 530eV is associated with electron excitation from O 1s to O 2p hybridised with TM 3d. therefore, the O-K pre-edge is commonly understood as the general sign of oxidation state of the system. The greater the intensity of the pre-edge, the more vacancies in the O 2p and TM 3d and therefore the higher its oxidation state. [266, 268, 269] In Figure 5.11, a general reduction in energy can be observed from the layered

structure into rocksalt as the pre-edge intensity decreases from bottom to top in both Figure 5.11b and d.

Another general rule in analysing core-loss EELS edges is the energy shift (also known as chemical shift): the edges shift towards higher energy loss for higher oxidation states. [218, 270-272] The correlation of the edge shift and oxidation state is due to the increased effective nuclear charge and therefore decreased shielding effect which results in a higher energy is required for the inner electrons to be excited to higher energy vacant states. In this case, energy shift can be observed in the Mn and Co L edges in this case. Reduction of Mn and Co are correlated with the structure degradation.

For Ni, changes in the EELS fine structure are less obvious between the pristine layered structure, where Ni exists as a 2+/3+ mixture in NMC622, and the rocksalt where Ni is reduced to solely 2+ in NiO. The key difference is the appearance of a shoulder at the higher energy loss of the L_3 edge, which can be seen to reduce from the top to the bottom spectrum in Figure 5.11b and d.

Overall, the PFIB damage at cryogenic and ambient temperatures of pristine NMC622 were characterised through the structural degradation and chemical reduction using atomic-resolution HAADF and core-loss EELS. The study shows that the cryo-PFIB significantly minimise the sample preparation damage down to 2nm on the surface. It's crucial to quantify this damage to accurately distinguish between the actual results of subsequent studies and any alterations caused by the beam.

5.4.3 Preserving Charged State of Cathode

Despite of the convenience of using the same grid for PFIB and STEM, the lamellae prepared by the H pattern method are highly mechanically unstable and have restricted tilting angle due to the adjacent chunky area. Most importantly, the preliminary sample to be PFIB milled must have

a thickness of <100um. If this is not achieved, milling an electron transparent window on a thick sample is very time-consuming even with the high milling-rate Xe PFIB.

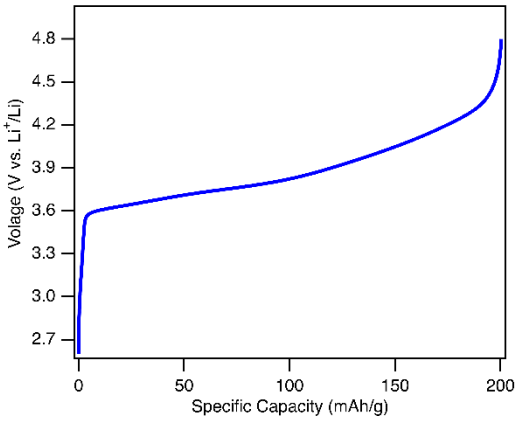


Figure 5.12: Cycle performance of NMC622|LPSCl|Li-In

To study the NMC622 at charged state, NMC622|LPSCl|Li-In cell was charged under 20Mpa, at C/20 rate to 4.8V vs. Li^+/Li. The composite cathode is a mixture of NMC622 and LPSCl in weight ratio of 70:30. The capacity is 200 mAh/g at 4.8V vs. Li^+/Li. The pellets made for cycling are much thicker (up to 2 mm) which is far above the thickness requirement for the H pattern method, so this method is no longer suitable for samples after cycling. According to the HAADF characterisation of PFIB damage at room temperature, the ion beam induced rocksalt layer is less than 10 nm. Therefore, if lift-out is performed at room temperature and leave enough buffer layer for the ambient temperature damage, and then proceed to thin the lift-out lamella at cryogenic temperature to electron transparency, the damage layer can be minimised using the lift-out method with a single thermal cycle rather than the two required to do both bulk milling and final polishing at cryogenic temperatures.

The ambient-temperature lift-out and cryo-thinning procedure is illustrated and its application on NMC622 cathode material at different states of charge are discussed in this section.

Method

The anaerobic transfer procedure is the same as the H pattern method. In the glovebox, the cycled battery pellet was mounted onto a SEM stub with carbon tape and then transferred to the PFIB via the iLoad holder. In PFIB, a Pt protective layer was deposited onto the region of interest (ROI), and then two trenches were made at the top and bottom of ROI, to make a lamella of around 4um thick to leave enough buffer layer for the ion beam damage. Then, a 'J' cut was made through the lamellae to be ready for the lift out procedure as shown in Figure 5.13a. The next step was to insert a W needle to pick up the lamella and transfer to the Omniprobe grid in Figure 5.13 b-d. After the needle was cut off and retracted, the sample was cooled down with liquid nitrogen for the cryo-thinning. The lamella was thinned with progressively lower currents as the desired lamella thickness is approached. For the final polishing, the ion beam current was reduced to 5kV 0.1~0.3nA to minimise beam damage.

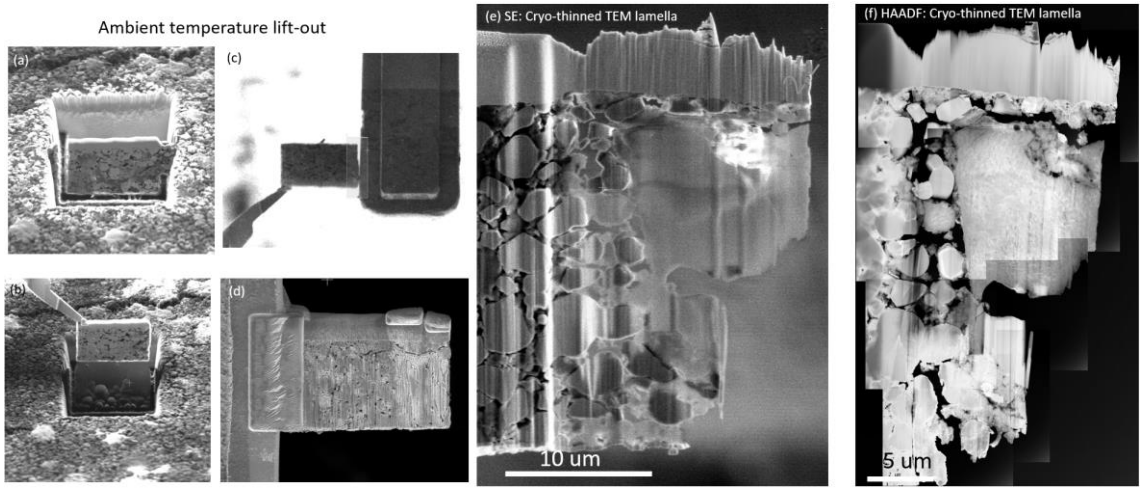


Figure 5.13: Workflow of ambient-temperature lift-out from (a) trenches milling, (b) lamella lifting using W needle to (c) lamella mounting to Omniprobe grid finger (d) lamellae after W needle removed, then the temperature is cooled down with liquid nitrogen to -100°C.

Charge Compensation in NMC622 During Cycling

Previously, the use of the H-pattern method has been demonstrated to effectively preserve the original structure and oxidation state of pristine NMC622. However, delithiated NMC622 in charged state becomes much more susceptible to structural degradation under the ion beam. Therefore, it is crucial to investigate the feasibility of employing PFIB to maintain the integrity of charged NMC622 for STEM studies.

Figure 5.14a shows EELS data for NMC622 at pristine, charged to 4.8V vs. Li^+/Li, and discharged states from a NMC622|LPSCl|Li-In cell, the cells were charged under 20Mpa, at C/20 rate. The composite cathode is a mixture of NMC622 and LPSCl in weight ratio of 70:30. The oxidation states of O, Mn, Co and Ni are compared to highlight their roles during cycling. The EEL spectra shown here are integrated across the bulk region to eliminate any contributions from the surface degradation effect.

The intensity of the O pre-peak experiences a significant rise after charging, which, as discussed earlier, suggesting the oxidation of NMC622 during delithiation. In contrast, Mn, being a stabilizing element in NMC structure, maintains its 4+ oxidation state at all charging levels. Co exhibits a minor energy shift toward higher energy loss at charged state, indicating Co oxidation. However, the most remarkable fine structure change occurs in the Ni L_3 edge, suggesting that Ni plays a dominate role in compensating for the electron loss during cycling.

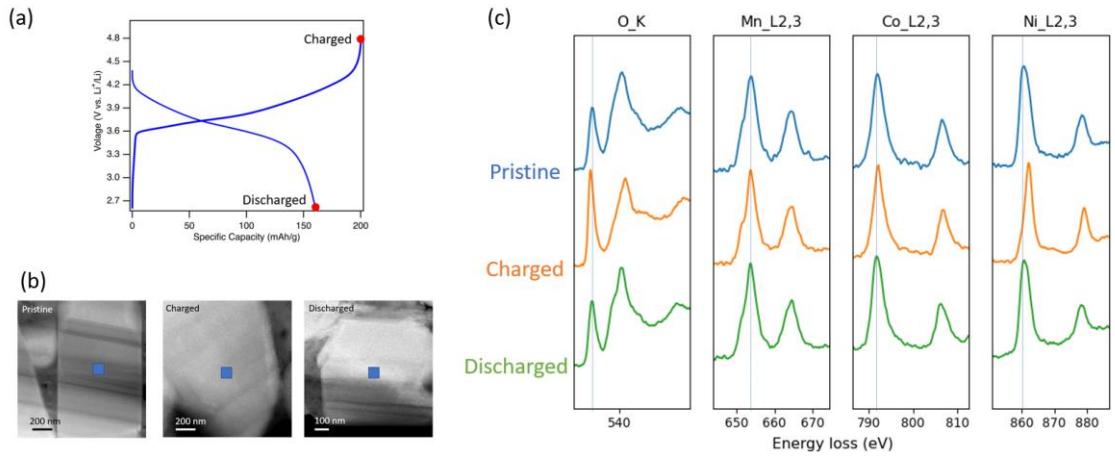


Figure 5.14: (a) Cycle performance of NMC622|LPSCl|Li-In (b) the spectrum acquisition area that corresponds to (c) EELS O-K, Mn-$L_{2,3}$, Co-$L_{2,3}$ and Ni-$L_{2,3}$ at pristine, charged to 4.8 V vs. Li^+/Li and discharged state.

X-ray techniques, such as XAS, has advantageous of superior energy resolution, but at the price of low spatial resolution. This makes XAS an ideal choice for studying bulk properties of materials in a static state. In Figure 5.15, the Mn, Co and Ni L_3-edge soft XAS spectra of electrodes at various states of charge from literature are presented as a reference. By comparing the EELS study with the XAS study, despite of the different energy resolution of EELS and XAS, the agreement in the fine structure features demonstrates the success of my approach in preserving the charged state after ion beam milling and electron beam exposure. In chapter 7, this approach will be applied to cathode/SE interface study and highlight the superior spatial resolution in STEM, by simultaneously mapping the oxidation state and element distribution across the interface with nanometre stepsize.

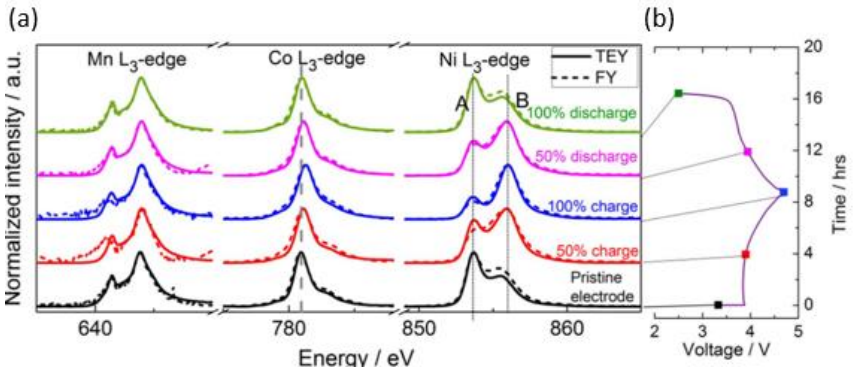


Figure 5.15: (a)Mn, Co and Ni L_3-edge soft XAS spectra of electrodes at various states of charge in total electron yield (TEY: 5nm from surface, solid lines) and fluorescence yield (FY: 50-100nm from surface, dashed lines) modes and (b) the corresponding voltage profile of the initial cycle [273] (Reproduced from Tian, C., et al., Journal of the Electrochemical society, 2018. 165(3): p. A696-A704. Under a Creative Commons Attribution license)

5.5 Conclusions

In summary, an anaerobic-transfer cryo-PFIB STEM sample preparation methodology for air- and beam-sensitive battery materials is presented in this chapter. A uniformly thin slice of NMC622 and LPSCl with a sharp interface is preserved. The beam damage on pristine NMC622 can be minimised to 2 nm characterised by the structure degradation from atomic resolution ADF image corresponding with chemical reduction from core-loss EELS. On delithiated NMC622 after charging, the charged state is successfully preserved. Upon charging, Ni takes the main role of charge compensation, while some redox can also be observed on Co. Mn, being the structure stabiliser, remains unchanged through cycling.

The practical challenges of transferring the air-sensitive sulphide solid electrolyte and preserving the beam-sensitive highly charged cathode materials NMC622 have been successfully achieved. A depth-dependent valence state change of O and TMs can be observed on the surface of NMC622 after PFIB milling. To quantify the penetration depth of surface reduction layer and study its evolution at different state of charge, next chapter will focus on the methodology of

EELS data analysis. Different methods will be compared and the tailored quantification method for rigorously obtaining the valence state of O and TMs in SSLIB will be presented.

Chapter 6 Electron Energy Loss Spectrum Fine Structure Quantification

6.1 Introduction

Building on the previous chapter's focus on sample preparation methods for acquiring high signal-to-noise ratio EELS data with minimal beam damage, this chapter now transit to the challenge of data analysis.

As have been discussed in the chapter 3, the core-loss EELS spectrum provides valuable information about the atom bonding, configuration and valence state with high spatial resolution. This chapter delves into the methodology of oxidation state quantification in core-loss EELS analysis. Three distinct methods: chemical shift, white line ratio, and energy loss near-edge structure (ELNES) fingerprint will be discussed and applied to an example dataset for comparative analysis.

During the data processing, an intriguing post-peak feature just above Ni-L edge was observed. This feature, combined with the partial cross-section calculated from the Dirac-based general oscillation strength, prompted a deeper investigation into the complex alterations of atomic shells during inner-shell excitations.

Additionally, this chapter will present a tailored methodology that focuses on the fine structure change. The process for quantifying the valence states from O-K, Mn-L_3, Co-L_3, and Ni-L_3 edges will be detailed. This methodology is not only integral to the analysis but also exemplifies the nuanced application of EELS in advanced material research.

6.2 Example Dataset

An example dataset acquired on 4.8V vs. Li^+/Li charged NMC622/LPSCl as shown in Figure 6.1 will be used for the following discussion. Applying different quantification methods on the same dataset provides a direct comparison of their ability in capturing the fine structure change and correlates it with the oxidation state change.

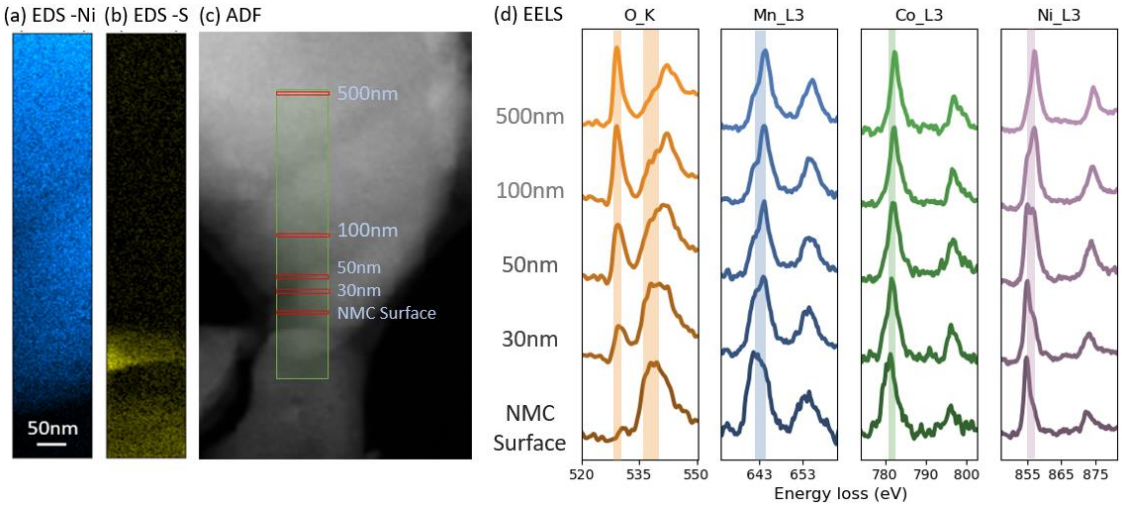


Figure 6.1: (a) EDS map of Ni (blue) from NMC622 and (b) S (yellow) from argyrodite, (c) ADF image, the spectrum area is marked in green, from the red labelled area at 500nm, 100nm, 50nm and 30nm from the interface and at interface (d) EELS fine structure are highlighted in shaded area.

Figure 6.1 shows the simultaneously acquired EDS and EELS maps on the NMC622 and LPSCl interfaces. Their interface can be located through the EDS map of Ni and S, the elements unique to the cathode and electrolyte respectively. The EELS data were acquired in the spectrum area marked in green in Figure 6.1c, spectra from five different depths from the interface were selectively extracted and stacked in Figure 6.1d, where the valence-dependent splitting and energy shift were highlighted in the vertical shaded region.

The top spectrum is extracted from a depth of 500 nm within the bulk of NMC622. Upon comparison with reference STEM-EELS and XAS data in literature [148, 270, 274], the intense pre-peak of O-K edge at 530eV and the energy position of Ni L_3 white line above 550eV indicate

the cathode was highly charged as expected. A uniform charging across the entire particle would optimise battery capacity. However, closer to the interface with the solid-state electrolyte, notable changes occur: there is a significant decrease in the O-K pre-peak intensity, and the L edges of Mn, Co, and Ni shift towards lower energy. These changes collectively suggest a reduction in the NMC622 near the surface, which could contribute to a loss of material capacity.

Understanding and quantifying this observed reduction is crucial for a fundamental discussion of the interfacial reactions under various conditions. To achieve this, the example dataset will be used to compare different quantification methods and establish a reliable approach for quantifying the reduction observed at the NMC622/LPSCl interface.

6.3 Quantification of TM $L_{2,3}$ Edge

The typical L edge of a 3d transition metal has features of 2 sharp peaks referred as 'white lines', since they were first discovered on photographic film in X-ray absorption spectra. [275] They emerge with the excitation of 2p electrons into highly localised unoccupied 3d orbitals. The splitting of the L edge is caused by the spin orbit coupling that 2p orbit splits into $2p_{3/2}$ and $2p_{1/2}$ which corresponds to the L_3 and L_2 edges respectively. If the energy resolution allows, a considerable amount of fine structures can be observed on the L edge.

Based on the energy range, these fine structures can be divided into ELNES and the extended energy loss fine structure (EXELFS); ELNES, observed within 30eV beyond the ionisation edge, offers insights into valence state, atom coordination, spin orbit interactions, and crystal field splitting, [276-281] EXELFS, appearing 40-50eV above the edge onset, involves higher kinetic energy electrons post-core excitation and is likely to undergo multiple elastic scatterings. EXELFS can reveal geometric information about neighbouring distances [282-284].

In EELS L edge analysis for 3d TM, three common methods are employed for oxidation state quantification: (1) chemical shift, observing shifts in the $L_{2,3}$ edge onset; (2) $L_{2,3}$ white line ratio, comparing the intensity ratios of I(L_3) to I(L_2); and (3) L_3 ELNES valence-dependent splitting analysis. In the following section, the chemical shift will be discussed first, followed by an introduction to model-based ELNES quantification and then the white line ratio and ELNES analysis will be applied and discussed with the example dataset.

6.3.1 Chemical Shift

In the chemical shift method, shifts in the onset energy of core-loss edges are observed to approximate changes in oxidation states. Typically, these edges shift towards higher energy losses by 1 to 2eV in materials with higher oxidation states, a trend observed across various elements in diverse materials. [285-287] The edge onset energy represents the energy difference between the inner-shell initial state and the lowest energy outer-shell final state. This chemical shift correlates with changes in the effective nuclear charge. As a material is oxidized - losing outer shell electrons - the effective nuclear charge increases, tightening the binding of inner shell electrons and requiring more energy for their excitation.

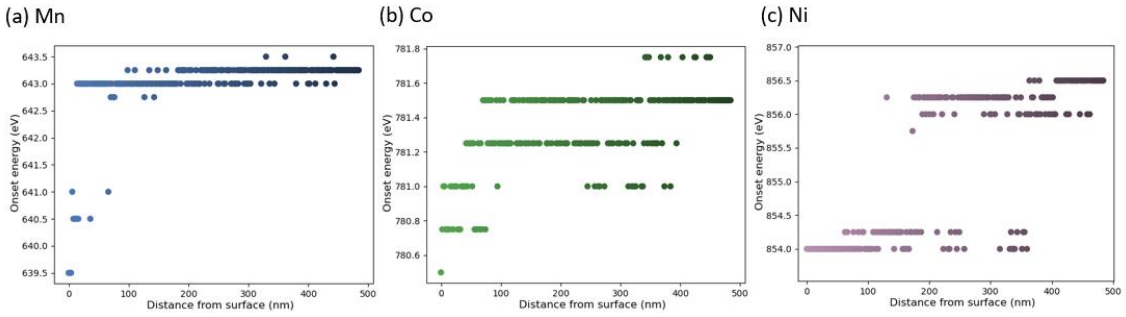


Figure 6.2: Edge onset energy of (a) Mn, (b) Co and (c) Ni from the interface to 500nm deep in the bulk of NMC622

On the example dataset, principle component analysis (PCA) [288] denoising is applied to smooth the spectra, and then the edge onset energy is determined from the maxima of the first derivative of the spectrum intensity. Figure 6.2 shows the chemical shift of the Mn, Co and Ni

from bulk to the interface. The markers may overlap with each other, but there is only one datapoint at a single depth. The discreteness along y axis came from the dispersion of 0.25eV/ch. Despite of the oscillation, the onset energy of three elements all showing a decreasing trend towards the interface suggests reduction. However, the chemical shift method lacks sufficient precision to determine at which depth the reduction happened and the degree of reduction.

A key challenge in employing the chemical shift method for precise quantification lies in the absence of a reliable theoretical model for calculating the absolute ionization threshold energy. The gain or loss of outer-shell electrons leads to complex alterations in binding energies across all electronic energy levels, including the initial core orbital and the final orbit. Further complexity comes from the dynamic relaxation effect, where electron orbitals around the positively charged core hole are pulled inward and cause reduction in measured binding energy. As a result, the chemical shift method may not always be valid for different species at various coordination environments.

From the data acquisition perspective, the accuracy in measuring the edge onset position can be influenced by a variety of experimental factors, including the energy resolution of both the source and detector, the eV/channel dispersion settings, and the calibration of the dispersion. Additionally, when multiple oxidation states are present, this method struggles to differentiate the proportion of each component.

Therefore, there is a need for a quantification method that can accurately determine the exact oxidation state and remain independent of experimental conditions, providing a more universally applicable and reliable approach to oxidation state determination in EELS.

6.3.2 Model Based ELNES Quantification

Introduction

The L edge ELNES of TM contains valence-specific multiplet structures which can be used as valence fingerprints. However, the challenge lies in how to isolate the useful information from noise and background intensity to ensure accurate quantification and to minimise artefacts. This requires a deep understanding of the energy-loss mechanisms that produce the features observed in EELS data. This section will start with discussion of the common noise removal steps used in literature and introduce a tailored model fitting quantification method of the $L_{2,3}$ edge for the beam sensitive material in method section. And then compare the white line ratio method and ELNES fitting method in correlating white line change with oxidation state change.

Systematic errors

The first step is to correct for systematic errors like dark current and gain reference which arise due to detector inherent properties. The scanning probe of STEM can cause noticeable drift, especially at low magnification. To address this, dual-EELS has been consistently acquired to capture both ZLP and the core-loss spectrum near simultaneously. This enables calibration of the core-loss spectrum by applying the same energy shift used to align the ZLP to 0 eV at each pixel. Another common artefact arises when X-rays enter the spectrometer, appearing as sharp, intense spikes on the spectrum. They should be removed and replaced with the interpolated intensity, according to the adjacent background.

Denoise

Apart from the systematic noises, there is random noise from the Poisson distribution of electron excitation. While longer exposure times or a brighter beam can reduce this noise, such methods are not suitable for beam-sensitive materials where minimising beam dose is essential.

Therefore, denoising methods such as principle component analysis (PCA) are commonly used to smooth the raw EELS data. However, PCA is a statistical technique used for signal processing and the principal components do not necessarily correspond with the specific physical processes that give rise to certain features in EELS data. Therefore, PCA can be arbitrary in smoothing the EELS data, and it should be used with caution or even avoided when studying subtle fine structures or weak SNR data in case it introduces artefacts.

Powerlaw background

The white lines observed in EELS spectra are superimposed on a continuously decaying background, resulting from the tails of plasmon peaks and previous edges. This background can be effectively removed by fitting a power-law or similar functions to a pre-edge region, typically over 30eV-50eV and extrapolating this fit to the edge region. Powerlaw background fitting is illustrated in Figure 6.3a.

Multiple scattering effect

The multiple scattering effect: where the incident electron undergoes more than one inelastic scattering event, can drastically alter the shape of the observed edge and affect the accuracy in white line area extraction. Fortunately, the multi-scattering can be removed through Fourier deconvolution when the sample thickness exceeds the mean free path. [218]

However, it's important to note that the mathematical process of Fourier deconvolution can introduce artefacts into the data, complicating subsequent quantification efforts. Deconvolution works better when the multiple scattering is not too severe. Otherwise, the forward convolution method [289, 290] in model fitting can avoid introducing noises while counting for the multiple scattering effect.

Partial cross-section

In addition to the prominent white lines where core-shell 2p electrons are excited into highly localized 3d vacant sites, these electrons can also transition into the continuum background. This transition results in ejected secondary electrons with kinetic energy, creating a smooth, flat tail after the ionisation edge. Historically, simple functions like the arctan function [291, 292] or step function [272, 293] were used in the early stages of $L_{2,3}$ quantification. They were soon replaced by more accurate partial cross section calculation from atomic wave functions. The partial cross-section specifies the probability of inelastic scattering within specific angular and energy loss ranges. The first step towards obtaining cross-sections is to calculate the generalized oscillator strength (GOS), which represents the probability of transition from its initial state to a particular state in the continuum. Commonly used models are the hydrogenic model [294] and the Hartree-Slater model [295].

The hydrogenic model is the simplest way to estimate GOS, based on wave mechanics of hydrogen atom, developed by Bethe in 1930. [296] It's particularly effective for K-shell edges, aligning well with experimental data while requiring minimum computing. [297] However, it falls short for L-shell and M-shell edges due to oversimplifications in screening effects and effective nuclear charge estimation. [298]

The Hartree-slater method (H-S) is a popular method for $L_{2,3}$ white line quantification in transition metal ion study. [299-301] Because it offers more accurate description of edge shape, by calculating the wavefunctions from an iterative solution of the Schrödinger equation with a self-consistent atomic potential. [302]

Both the hydrogenic and H-S models provide free-atom cross-sections, overlooking the effects of chemical bonding on wavefunctions and collective excitations. [303] To include electron spin and relativistic effects within the atom, the Dirac equation can be employed. [304, 305]

The computed GOS needs to be scaled and aligned to fit the experiment data. The fitting range for scaling is usually in the lowest window in the post-edge region depending on the EXELFS oscillation position as shown in Figure 6.3b. The edge onset position is usually bounded with white line maxima.

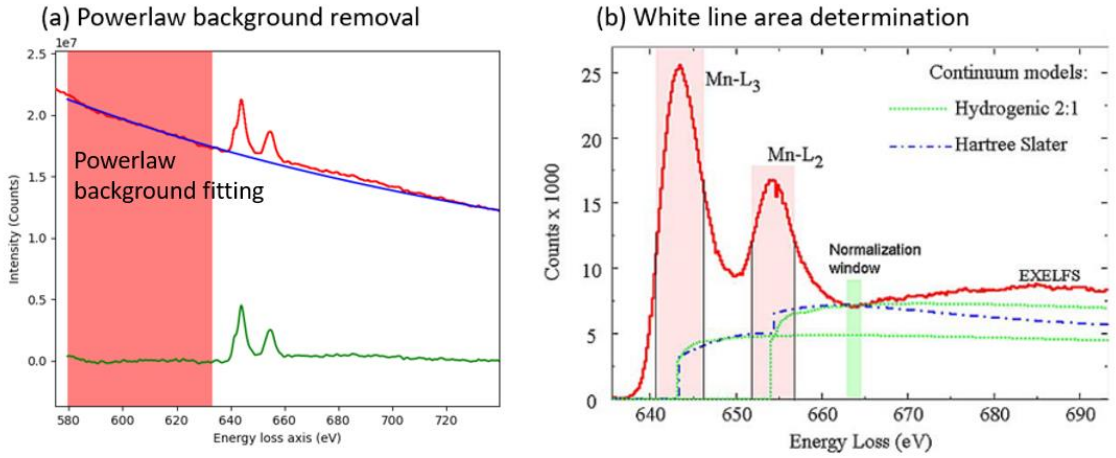


Figure 6.3: (a) Powerlaw background fitting, before (red spectrum) and after (green spectrum) powerlaw background removal of Mn-$L_{2,3}$ edge, (b)background subtracted Mn-$L_{2,3}$ ionisation edge. Hartree–Slater and modified double-step hydrogenic continuum models are shown with step onsets at peak maxima and height ratio 2:1. Positions of normalisation and integration windows are indicated by the shaded regions. [299] (Reprinted from Schmid HK, Mader W. Micron. 2006 Jul 1;37(5):426-32. Copyright 2006, with permission from Elsevier.)

Regarding data processing methods, the raw data can be directly modified to minimise noise and remove background intensity or models can be employed to fit the experimental data which offers enhanced accuracy, especially in noisy datasets. [289, 306]

In the model fitting method, the model components can vary from experimental or computed reference spectra to purely mathematical descriptions of white line splitting. Shuman and Somlyo [307] used the linear sum of the powerlaw background and external reference spectra to fit the experiment result for elemental analysis. This method was extended to explore the mapping of the bonding through variation of white line fine structure change by Arenal. [308] Mendis *et al.* [309] used spectra from the surrounding pure matrix as reference to identify interface with different volume fraction and therefore only used data from the sample being

analysed. Van Aken used the sum of the gaussian peaks, with the arctan function as the mathematical description of the white line splitting for modelling the more intense Fe L_3 ELNES spectra. [292, 310, 311]

Method

From the discussion of noise removal and subtraction, although there are some minor variations in the methods, the physical meaning of each step is clear. Considering the beam-sensitive nature of battery materials, a specialized quantification method for the analysis of fine structure changes for battery materials have been developed.

This approach incorporates several key steps. Recognising that the fine structure changes are prominent, as evident in Figure 6.1, PCA denoising is avoided. While PCA is a powerful tool for noise reduction, it can easily smooth out critical fine details arbitrarily. Instead, the SNR was improved through pixel binning. From the 2D array of EELS data which was acquired at the interface (as highlighted by the green region in Figure 6.1c, pixels that were parallel to the interface were binned. This strategy allowed us to conduct a depth-dependent study of interfacial reactions, preserving the integrity of the raw fine structure.

Secondly, due to low dose in the data acquisition, the spectra still possessed noticeable Poisson noise after pixel binning which was amplified after Fourier deconvolution and complicated further quantification. Considering the noisy nature of the raw data, forward convolution was determined to be more appropriate for our analysis.

Thirdly, the spin-orbit splitting energy gap increased with atomic number. Although the Co and Ni $L_{2,3}$ white lines were well separated, the Mn $L_{2,3}$ white lines still exhibited some degrees of overlapping as shown in Figure 6.4. Unlike the direct modification on raw data, such peak overlapping is effectively addressed through model fitting. Lastly, model fitting enables

convenient estimation of the fitting quality. This step is crucial for ensuring the accuracy and reliability of the quantification process.

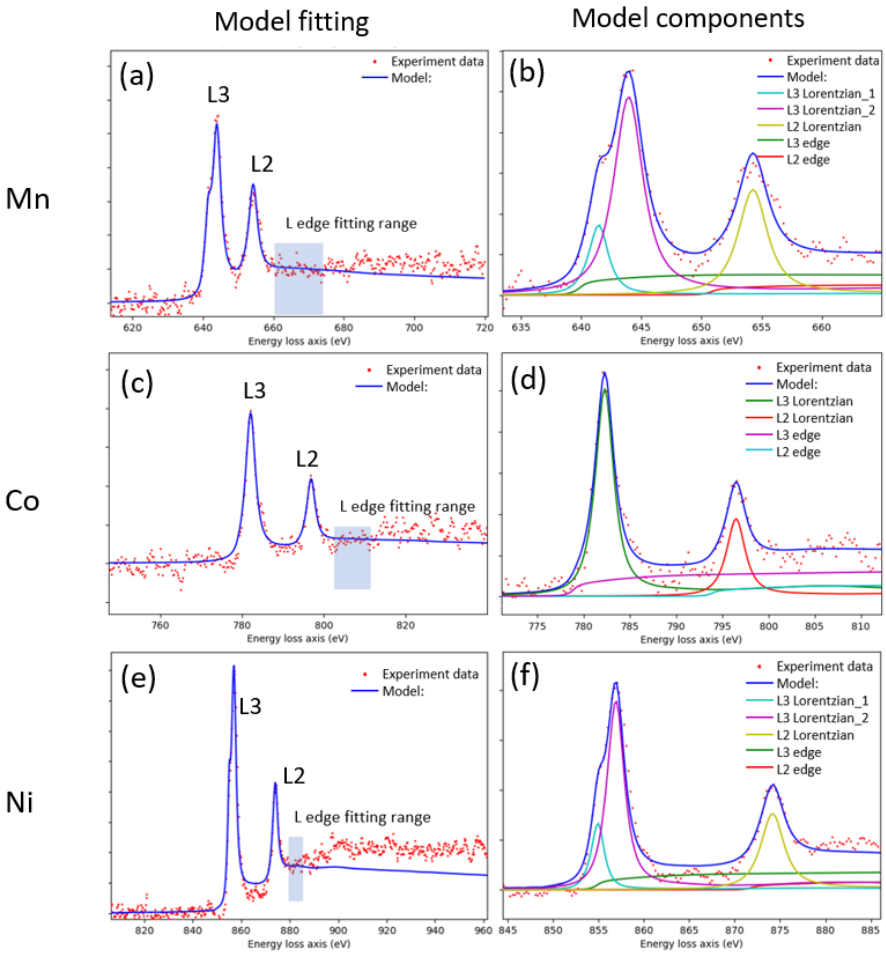


Figure 6.4: Model fitting and model components for (a)(b) Mn (c)(d) Co and (e)(f) Ni.

Overall, the data processing workflow is summarised as below: the dataset was firstly corrected with gain and dark references. After the ZLP was aligned and X-ray spikes were removed, the powerlaw background was removed by fitting the 30eV-50eV pre-peak region.

The following model fitting process is illustrated in Figure 6.4. Models consisting of H-S background and Lorentzian peaks were used to fit powerlaw background removed data in which the Lorentzian peaks did not directly reflect the physical conditions, but as descriptions of the details of the TM L_3 ELNES fine structure, energy positions and FWHM. The L_3 and L_2 continuum cross section intensity ratio was bounded to 2:1. For Mn and Ni L_3 white lines, two Lorentzian

peaks were used to accommodate their pronounced asymmetrical shapes, influenced by crystal field splitting in the 3d final states.

The model then underwent forward convolution with the low-loss spectrum in Hyperspy, [312] followed by a least square fit to the experimental data. The overall fitting performance and the model components for Mn-$L_{2,3}$, Co-$L_{2,3}$, Ni-$L_{2,3}$ are presented in Figure 6.4. Finally, the quality of the fitting is quantified through the calculation of the R^2 value. R^2 is a statistical measure used to estimate the goodness of fit of a regression model and can be calculated as below. The closer the R2 value is to 1, the better the fit. Considering the Poisson noise in the experiment data, an R^2 value maintained above 0.9 is indicative of a good fit.

$$SS_{res} = \sum_i (y_i - f_i)^2$$

$$SS_{tot} = \sum_i (y_i - \bar{y})^2$$

$$R^2 = 1 - \frac{SS_{res}}{SS_{tot}}$$

$y_i - observed\ value$

$f_i - predicted\ value\ from\ the\ model$

$\bar{y} - mean\ of\ the\ observed\ value$

In the following section, the white line ratio method and ELNES fitting of L_3 edge method will be used to capture the white line structure change and quantifying them into oxidation state.

White Line Ratio

Due to the 2j +1 degeneracy, the L_3/L_2 intensity ratio is expected to be statically 2:1. However, wide deviation was found in 3d transition metals in 1980 by Leapman and Grunes. [313] A systematic study of 3d transition metal $L_{2,3}$ edges in 1982 by Zaluzec showed that the L_3/L_2

intensity ratio increased noticeably with higher atomic number. [314] In the same year, Leapman *et al.* observed L_3/L_2 intensity ratio increase with higher oxidation state in Ti and Mn. [315] These discoveries then triggered extensive exploration of the correlation between 3d TM oxidation state and $L_{2,3}$ white line state both experimentally [271, 272, 286, 293, 316] and theoretically. [317, 318] During this, some empirical rules were concluded: the L_3/L_2 ratio increased from d_0 and reached a maximum for the d_5 configuration and then decreased in going from d_5 to d_{10}. [316] Additionally, a linear correlation was discovered between the total intensities of the $L_{2,3}$ white lines and the number of unoccupied 3d states in 3d transition metals. [293] The white line ratio method has been popular in materials such as catalysts, batteries and other transition metal-based compound where understanding the oxidation state is crucial for determining material properties. [319-322]

In this section, the white line ratio is calculated by the sum of Lorentzian peaks area for L_3 white line divided by the Lorentzian peak area of L_2. The computed white line ratio will be compared with reference data for a comprehensive analysis.

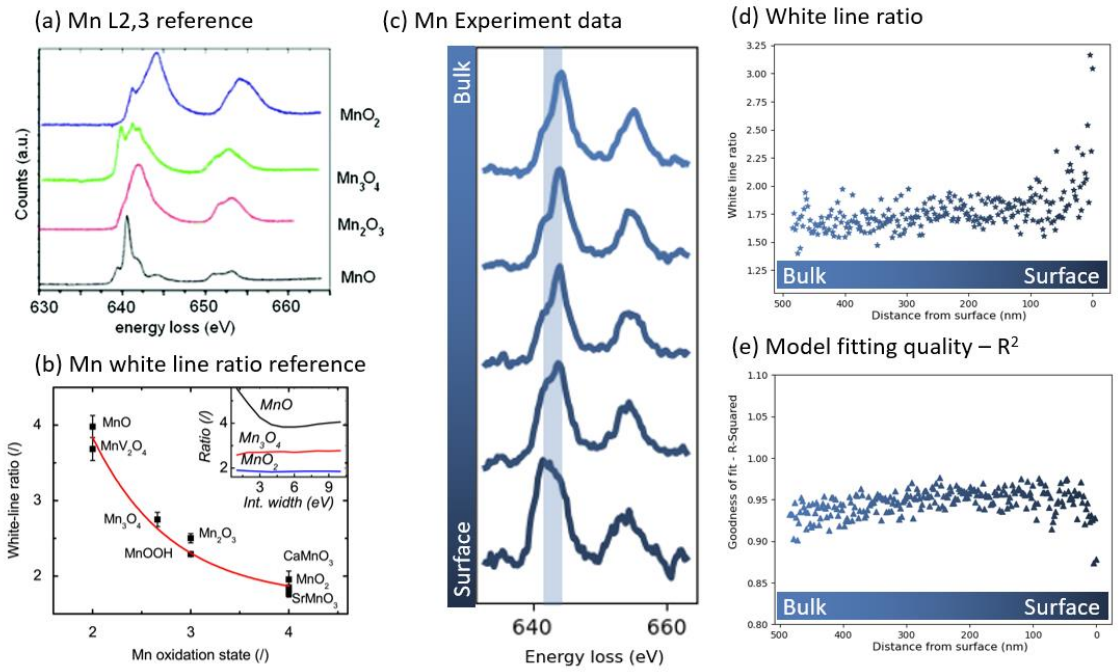


Figure 6.5: Reference of Mn (a) $L_{2,3}$ edge, and (b) corresponding white line ratio [301, 323] (Reprint with permission from Goode AE, Porter AE, Ryan MP, McComb DW. Nanoscale. 2015;7(5):1534-48. permission conveyed through Copyright Clearance Center, Inc) (Reprinted from Tan H, Verbeeck J, Abakumov A, Van Tendeloo G. Ultramicroscopy. 2012 May 1;116:24-33. Copyright 2012, with permission from Elsevier.) (c) Mn-L edge experiment data from bulk to surface, (d) Mn $L_{2,3}$ white line ratio plotted against the depth from surface, (e) model fitting quality – R^2 for each datapoint in (d)

The computed Mn $L_{2,3}$ white line ratio in Figure 6.5d is plotted with the distance from the interface which showed a sudden increase as the surface is approached. This trend, when compared to the reference in Figure 6.5b, indicates Mn remains at 4+ in the bulk, but in moving closer to the interface, a transition to a mixture of 2+ and 3+ states is observed. The quality of model fitting for each datapoint is measured by R^2 plotted in Figure 6.5e, which is overall above 0.9, except for the 2 datapoints at interface where the SNR is lower due to reduced thickness at the surface.

However, the white line ratio of Co in Figure 6.6d does not exhibit a clear trend, despite the satisfactory quality of model fitting. Thus, the white line ratio method may not be the most direct

indicator of Co oxidation state changes. The low R^2 value for the datapoints at interface is due the low SNR at the thin surface.

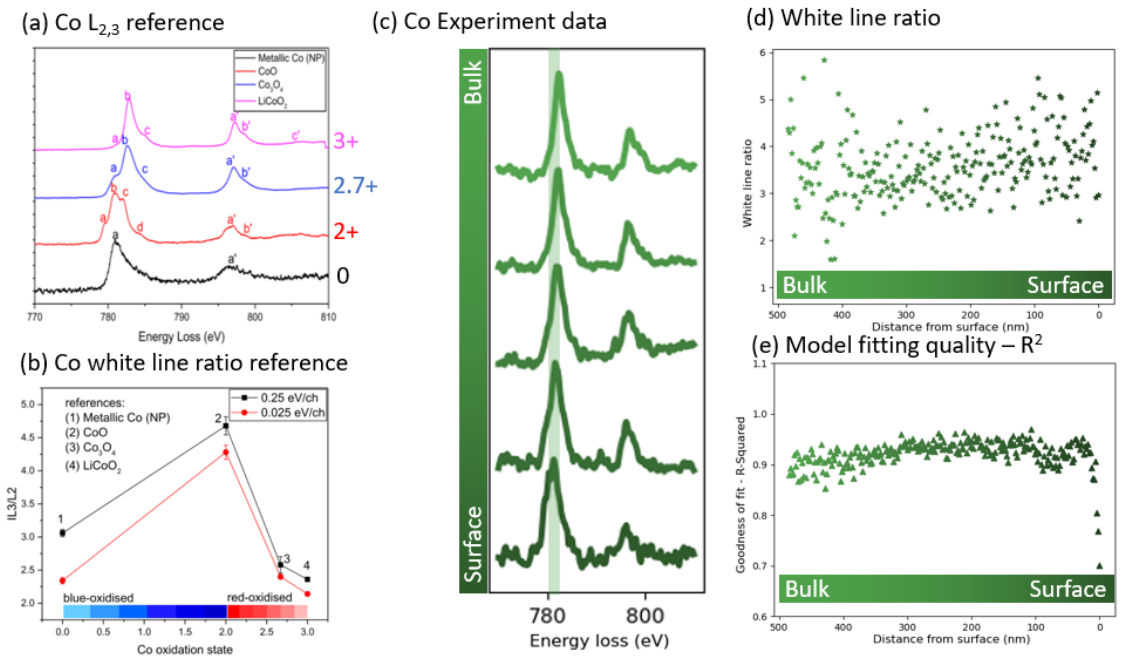


Figure 6.6: Reference of Co (a) $L_{2,3}$ edge, and (b) corresponding white line ratio [324] (Co $L_{2,3}$ reference credit to Dr. James Sode) (c) Co-L edge experiment data from bulk to surface, (d) Co $L_{2,3}$ white line ratio plotted against the depth from surface, (e) model fitting quality – R^2 for each datapoint in (d)

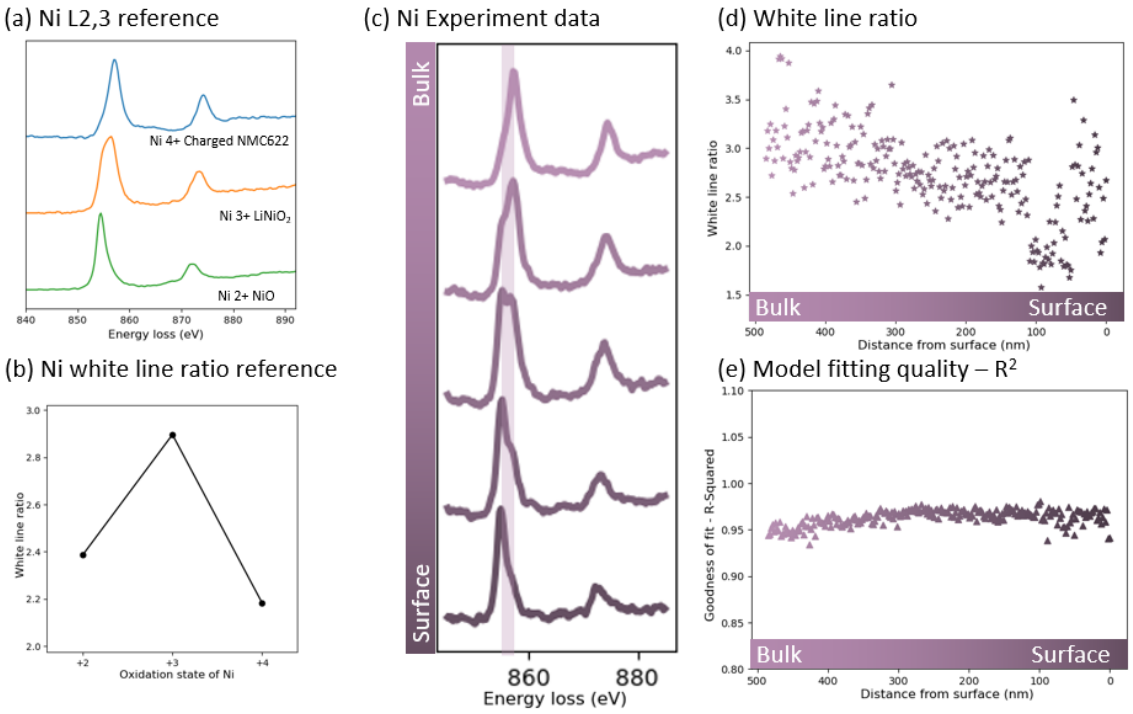


Figure 6.7: Reference of Ni (a) $L_{2,3}$ edge, and (b) corresponding white line ratio (c) Ni-L edge experiment data from bulk to surface, (d) Co $L_{2,3}$ white line ratio plotted against the depth from surface, (e) model fitting quality – R^2 for each datapoint in (d)

Similarly, the Ni white line ratio does not provide a straightforward interpretation of Ni redox reactions at the interface. However, the R^2 values for Ni remain well-controlled around 0.95, indicating reliable model fitting.

When compared to the chemical shift method, the white line ratio approach offers more robustness against variations in experimental conditions. The white line ratio calculation can effectively correlate to oxidation state for Mn in this study and other well-studied elements such as Fe. [299, 311] However, it is not robust enough for other elements in different coordination. Various examples in the literature have reported contradictory relationships [285, 315] Additionally, the alteration of noise removal methods can significantly influence the quantified white line ratio. [292]

Given the pronounced change of fine structure from bulk to surface, a more responsive method that can grasp those changes and correlate to oxidation state change is needed.

Before moving to the discussion of another quantification method, I would like to discuss an interesting feature in the post-edge region of L_2 which was observed during the model fitting processing which could offer additional insights into the electronic structure and chemical environment of the transition metal ions.

Misalignment of Energy Onset of White Line and Cross Section

Figure 6.8 shows O-K, Mn-L, Co-L and Ni-L edges simultaneously acquired in one spectrum. When fitting the Hartree-Slater cross sections for L_3 and L_2 with a statistical ratio of 2:1, a rising bump after the L_2 white line can be noted in Co and more prominently in Ni. This bump, if observed in isolation as in Ni, might typically be attributed to multiple scattering effects. However, given the absence of a significant thickness effect in Mn and Co, plus the negligible plasmon peak in the dual-EELS low-loss spectrum (Figure 6.8b), this feature seems to be inherently linked to the electronic structure of Ni.

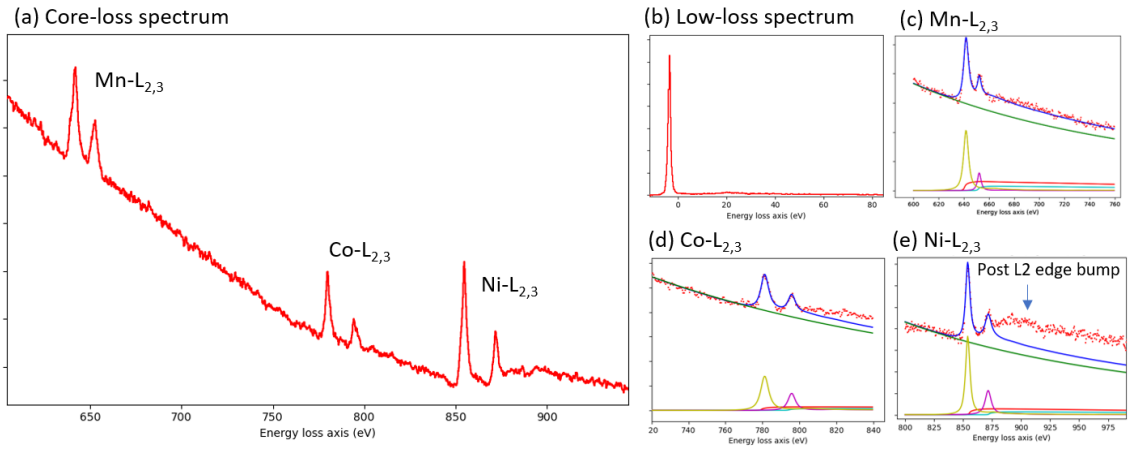


Figure 6.8: Dual-EELS of (a) core-loss spectrum and (b) low-loss spectrum, comparison of model fitting on (c) Mn-$L_{2,3}$ (d) Co-$L_{2,3}$ and (e) Ni-$L_{2,3}$.

The features observed 40-50eV above the edge onset: EXELFS, are typically understood as resulting from photoelectrons backscattering off neighbouring atoms after exciting core electrons, providing insights into short-range order. The first discussion of a post-peak above

the L edge in TM was by Wang *et al.* [291] in 2006, where they reported a broad post-peak above the Fe L edge in iron fluorides and oxides, absent in metallic iron. The observation was attributed to the strong backscattering of the surrounding F and O atoms, they suggested that similar features might be observed in other TM oxides.

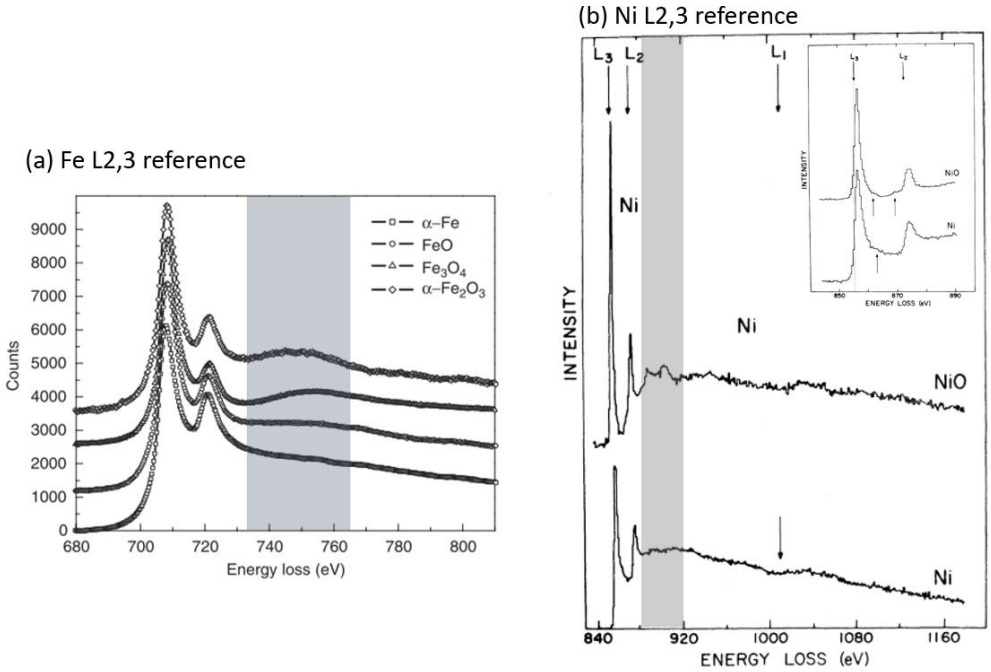


Figure 6.9:Experimental L edge of (a) iron and iron oxides [291], (Reprinted from Wang F, Egerton RF, Malac M. Ultramicroscopy. 2006 Aug 1;106(10):925-32. Copyright 2006, with permission from Elsevier) (b) nickel and nickel oxides [315]. (Reprinted with permission from Leapman RD, Grunes LA, Fejes PL. Physical Review B. 1982 Jul 15;26(2):614. Copyright 1982 by the American Physical Society.)

Figure 6.9b presents the comparison of Ni^{2+} and metallic Ni L edge with same energy resolution. The similarity of post-peak in is the oxide and its absence in metallic metal in Ni L edge and Fe L edge as highlighted in the grey region in Figure 6.9, suggests possible similar backscattering of surrounding O in oxides. Apart from the coordination, I would like to discuss the contribution from the electronic structure change of the TM ion to the post-peak. Unlike Fe, the larger spin orbit splitting energy gap in Ni, enables the gap between L_3 and L_2 white lines to be observed without peak overlapping. For metallic Ni, the L_3 and L_2 partial cross sections sit underneath the respective white lines in an approximate 2:1 ratio. However, for NiO, the intensity between L_3

and L_2 white lines almost drops to zero. Based on these observations, a delay in the partial cross-section was hypothesized and calculations was conducted to test its validity.

Conventionally, the change of valence orbit occupancy is not taken into account in partial cross-section calculations, including the common Hartree-Slater and hydrogenic models, being free-atom models. Motivated by the observation of broad post-edge peak in experiment data, Dr. Zezhong Zhang used the Dirac equation to calculate the NiO and Ni L edge, [325] accounting for electron spin and relativistic effects, to calculate the edge onset and shape for Ni^{2+} and metallic Ni, as shown in Figure 6.10b. The calculated edge onset was 848.6eV for metallic Ni and 868.4eV for NiO, with a substantial difference of 19.8eV. When fitting the computed cross section to the experimental data, the metallic Ni cross section was shifted by 5eV to 853.6eV for a better fit, resulting in a cross-section onset difference of 14eV, as illustrated in Figure 6.10c.

Interestingly, while the cross-section onset has significantly chemical shifted by 14eV when Ni is oxidised from 0 to 2+, the white lines only has 1eV of chemical shift. This discrepancy suggests that the loss of valence shell electrons predominantly affects the continuum band's position (relative to the 2p orbit), while the energy gap between the 2p and 3d orbitals remains relatively unchanged.

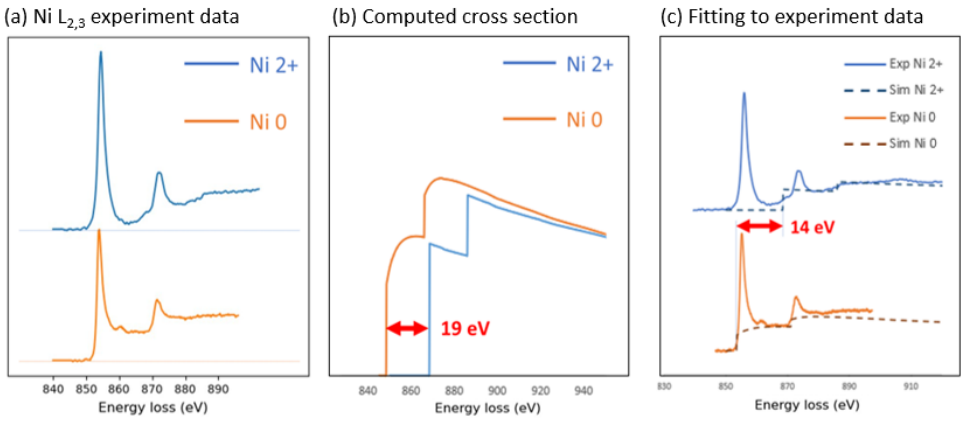


Figure 6.10: (a) Experiment data of EELS Ni $L_{2,3}$ at 0 and 2+, (The metallic Ni experiment data is adapted from EELS Database: Philip Ewels, Thierry Sikora, Virginie Serin, Chris P. Ewels and Luc Lajaunie."A Complete Overhaul of the Electron Energy-Loss Spectroscopy and X-Ray Absorption Spectroscopy Database: eelsdb.eu."Microscopy and

Microanalysis, 22, 717–724 (2016), doi:10.1017/S1431927616000179, contributed by Potapov PL, Kulkova SE, Schryvers D, Verbeeck J. Physical Review B. 2001 Oct 22;64(18):184110.) (b) computed partial cross section of Ni $L_{2,3}$ at 0 and 2+,[325] (c) fitting of the computed partial cross section to experiment data

This observation raises important questions about the conventional understanding of oxidation processes in transition metals, particularly regarding how these changes are reflected in EELS spectra. The discrepancy between the behaviour of the continuum band and the 2p-3d gap underlines the complexity of electron interactions in oxidised states and emphasizes the need for a better approach to interpreting EELS data.

ELNES Fitting

Back to the quantification of TM L edge white lines. As stated in the method section, the analysis of white line structure in EELS was enhanced by employing multiple Lorentzian peaks to describe the valence-dependent splitting of the L_3 peak. This approach diverges from the traditional method of taking the area ratio under the L_2 and L_3 white lines. Instead, the fitting coefficients are used to track the fine structure changes and therefore capture the oxidation state change.

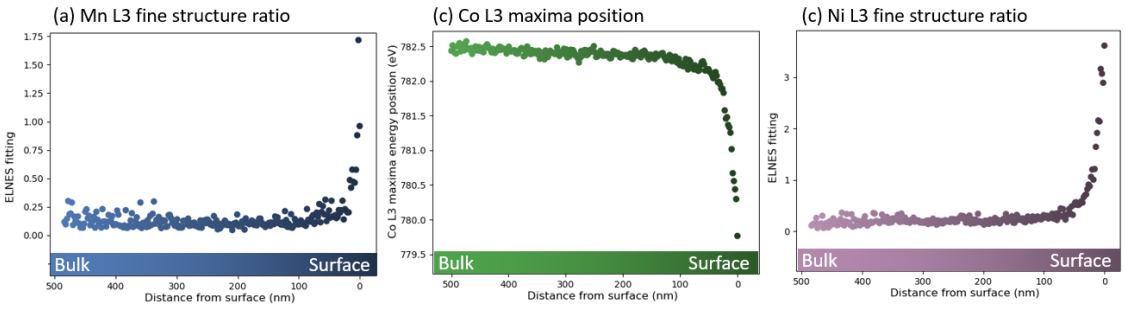


Figure 6.11:ELNES fitting of (a) Mn: intensity ratio of L_3 splitting peaks at 641.5eV and at 644eV, (b) Co: energy position of L_3 maxima, (c) Ni: intensity ratio of L_3 splitting peaks at 855eV and at 857eV.

The L_3 white line of Mn^{4+} typically features a main peak at 644eV with a shoulder at 641.5V. Upon reduction, this white line gradually shifts towards the peak at 641.5eV. The intensity ratio of these two peaks was used to represent valence changes of Mn, as shown in Figure 6.11a. The

ratio remains constant in the bulk but exhibits a sharp increase at approximately 80 nm from the interface, indicating a shift in the Mn L_3 white line towards lower energy and a reduction.

Although the Co L_3 white line exhibits negligible splitting at the current energy resolution of 1eV, experimental data reveals a monotonic energy shift towards lower energy. Consequently, the central position of the Lorentzian peak for the Co L_3 white line was employed to indicate the oxidation state. Figure 6.11b shows the maxima position of the Co L_3 white line plotted against the distance from the surface, revealing a sudden reduction at about 100 nm.

The Ni L_3 white line splits into two peaks at 855eV and 857eV. According to the reference data of Ni L edge in Figure 6.7, the Ni L_3 white lines show transition from the higher energy peak to the lower one from Ni^{4+} to Ni^{2+}, appearing as a broad peak at the 3+ state. Figure 6.11c plots the intensity ratio of the 855eV peak over the 857eV peak. This ratio remains close to zero in the bulk, indicating the dominance of the higher energy peak of Ni^{4+}. The sharp increase approaching the interface suggests a reduction of Ni as the L_3 white line transitions to the lower energy peak.

This approach, tailored for each specific element, has proven to be highly effective in capturing subtle changes in the fine structure of Mn, Co, and Ni. More importantly, the accurate tracking of fine structure allows the precise depth of redox reaction to be determined, which is essential for my study on interfacial reaction evolution.

6.4 O Covalency

The selection of a 0.25eV/channel dispersion setting in my study enabled the simultaneous collection of the O-K edge along with the L edges of the three TMs. This approach is particularly advantageous for a comprehensive analysis of oxidation states and bonding interactions within the material.

The O-K edge arises from electron excitations from the O 1s to O 2p orbitals. Characteristically, the O-K edge features a pre-peak and a main peak around 530eV and 540eV. Notably, the energy position and intensity of these peaks are influenced by changes in the valence state, bonding nature, and coordination of oxygen. Based on first-principle calculations of the O-K edge in NiO, [326, 327] the pre-peak is associated with electron transitions to hybridised O 2p and TM 3d orbitals, while the main peak corresponds to transitions to hybridised O 2p and Ni 4s or 4p bands. An increase in the intensity of the pre-peak suggests a higher valency in the TM and stronger covalent bonding between oxygen and the transition metal. Consequently, the relative intensity of the pre-peak to the main peak serves as a convenient indicator of the overall redox trend in TM oxides. [186, 328, 329] A more pronounced pre-peak implies a higher degree of oxidation, reflecting the increased electron vacancies and the nature of O-TM bonding.

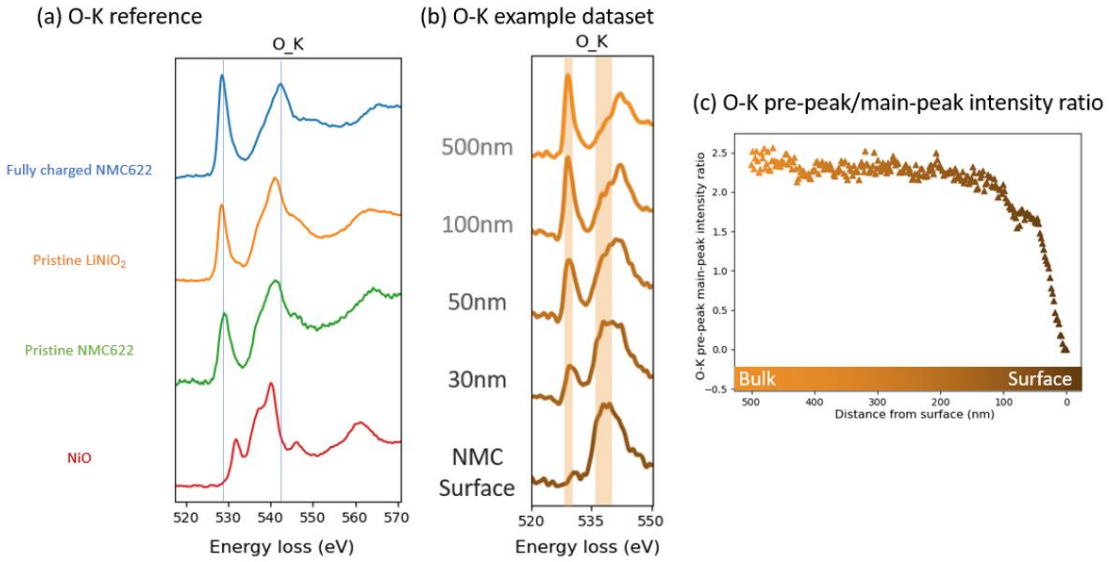


Figure 6.12: (a) O-K reference spectra, (b) O-K example dataset and the corresponding (c) intensity ratio of pre-peak and main-peak plotted against the depth from interface.

The pre-peak/main-peak intensity ratio is plotted against the depth from surface in Figure 6.12. The value remains stable in the bulk and decreased to zero as approaching the interface, suggesting reduction of the oxide. The reduction depth is around 120nm.

6.5 Conclusions

In this chapter, three different EELS fine structure quantification methods: chemical shift, white line ratio and ELNES fitting have been discussed and compared on the same example dataset. A tailored ELNES fitting method that avoids arbitrarily denoising of the spectra, and replacing the Fourier deconvolution which introduce noises by forward convolution in model fitting have been presented. This method has been proved to fit nicely with the experimental data and capture the valence states from the subtle fine structure changes in EELS. Additionally, the observation of the broad post-L edge bump of Ni has been attributed to the 14eV energy shift of the Ni partial cross-section, based on the Dirac-based GOS calculation.

So far, establishment of the anaerobic-transfer workflow and the TEM sample preparation technique in previous chapters, together with the data processing methodology in this chapter, have all provide solid foundation to the last result chapter. The evolution of interfacial redox reaction between NMC622/LPSCl at various charging states will be studied.

Chapter 7 STEM-EELS study of NMC622/LPSCl Interfacial Redox Reaction

7.1 Introduction

The bottleneck of SSLIB has been discussed in Chapter 1: the low coulombic efficiency and short cycle life, predominantly due to high electrode/electrolyte interfacial resistance. This challenge is often linked to loss of contact, chemical as well as electrochemical reactions occurring at the interface.

A thorough understanding of the interfacial redox reaction is crucial for advancing composite electrode designs and enhancing interfacial engineering strategies. Multiscale characterisation has been applied to identify interfacial products, their spatial distribution, their ionic/electronic nature, and their effect on cell performance.

Specifically at the NMC/LPSCl interface, studies have identified degradation products NiS, CoS, MnS, Li_2S, LiP_xCl_y, and LiCl in the discharged state, whereas $Mn_3(PO_4)_2$ or $Ni_3(PO_4)_2$, Li_3PO_4, PO_x, and SO_x ($2 < x < 3$) are detected after electrochemical cycling through XPS. [330, 331] Alongside, XAS confirmed the tendency of P−O and S−O bonds formation as a result of electrochemical reaction [197]. TOF-SIMS provided improved spatial resolution in studying the composition and morphology of the interphase. [331]

Surface reduction of the cathode has been studied with several X-ray based techniques such as resonant inelastic X-ray scattering (RIXS), XAS and X-ray Raman spectroscopy. However, their poor spatial resolution limits a precise measurement of the dimension of the surface reduction layer. The inherent challenge in studying these interfaces lies in their buried nature and the composite makeup of most cathodes, which include solid electrolyte, active material and conductive carbon additives. This complexity necessitates a strategic approach to experimental design, to probe the interfacial reaction at high spatial resolution. The analytical STEM enables

direct visualisation of the crystal structure, high spatial-resolution mapping of elemental distribution, chemical states and electronic structures at the interface.

However, despite the unparalleled spatial and energy resolution of STEM techniques, the difficulty lies in the preparation of electron transparent samples, especially specimen in the reactive charged state. Therefore, its application in SSLIB materials study is largely confined to thin edges of around 30nm beyond the surface on large particles and at the discharged state. The interfacial redox region on NMC622/LPSCl has not been precisely measured, which could possibly penetrate further than 30nm and evolve upon charging and discharging. A systematic study with much larger field of view in terms of oxidation state mapping is necessary to answer this question. My study seeks to bridge this gap, by using cryo-PFIB to mill micrometre level electron-transparent region at NMC622/LPSCl interface with minimised beam damage, and mapping the oxidation state in nanoscale spatial resolution through EELS quantification.

To lay the groundwork for a comprehensive examination of the interfacial redox reaction, I have adopted consistent sample preparation methodology and data analysis methods across all materials. The specifics of this anaerobic-transfer and cryo-PFIB lift-out technique and core-loss EELS fine structure quantification are detailed in previous chapters. In this chapter, the spontaneous chemical reaction between NMC622/LPSCl is discussed and compared to the pristine NMC622 prepared in the same workflow. Then, the interfacial reduction layer thickness and its evolution upon charging and discharging is measured precisely for O, Mn, Co and Ni. To distinguish the interfacial redox reaction with LPSCl from the self-decomposition of NMC622 especially at high charging voltage, the NMC622 charged with solid electrolyte LPSCl is compared to NMC622 charged in a $LiPF_6$ in EC/DMC liquid electrolyte. Finally, the mechanism of interfacial redox reaction is discussed through a study of elemental migration across the interface with EDS quantification.

7.2 Spontaneous Chemical Reaction Upon Mixing

If the cathode and the solid electrolyte have a mismatch in chemical potential, spontaneous chemical reactions may occur once these two materials are put into contact. On a mixture of NMC and LPSCl without biasing, Jung *et al.* observed impedance increase as a function of contacting time. The bulk impedance increase can be due to the degradation of both the NMC and LPSCl, whereas interfacial impedance growth is due to formation of the CEI as an ion-blocking layer. [332] An XPS study found the formation of phosphates and sulphates such as Li_3PO_4 and Li_2SO_4 on the uncycled NMC622/LPSCl sample, however XPS detection is limited in identifying TM species due to signal overlap. As a result, the detection of degradation products of LPSCl is usually attributed to the surface reaction with residual water and oxygen molecules on the cathode surface rather than the spontaneous redox reaction with NMC622. [330, 331]

The ambiguity of the spontaneous redox reaction between NMC622/LPSCl can be solved by core-loss EELS which can probe the oxidation states of the TMs in NMC622. Additionally, the precise surface reduction layer depth for each element can be quantified on the cryo-PFIB lift-out lamellae of pristine NMC622 and mixed NMC622/LPSCl samples. The latter specimen was prepared by mixing NMC622 and LPSCl powder using mortar and pestle, and then pressed into pellet under 500MPa.

Figure 7.1 compares the ADF/EDS/EELS data acquired on the uncycled NMC622/LPSCl interface and pristine NMC622 sample prepared in the same workflow. The spectrum areas are marked in green in the ADF images in Figure 7.1a and c. The interface of the NMC622/LPSCl sample is located through an EDS map of Ni and S as shown in Figure 7.1d. EELS data of O-K, Mn-L_3, Co-L_3 and Ni-L_3 extracted from different depth in NMC622 are stacked in Figure 7.1b,e, the changes of fine structure are highlighted by the shaded area.

The quantification method of EELS fine structure has been discussed in Chapter 6. The O covalency is quantified through the relative intensity of the pre-peak to the main peak, a higher

pre-peak implies a higher degree of oxidation. Therefore, the low O-K pre-peak at the surface of pristine NMC622 particle suggests reduction induced by the Xe ion beam damage. In comparison, the interface at the NMC622/LPSCl shows a much lower O-K pre-peak, suggesting a pronounced further reduction caused by the spontaneous redox reaction with LPSCl. The quantification of the fine structure change is performed for a straightforward interpretation of the reduction layer depth on NMC622 surface. The quantification method: ELNES fitting, have been discussed in details in Chapter 6: the pre-peak/main-peak intensity ratio of O-K; the intensity ratio of the peak at 641eV over the peak at 644eV of Mn-L_3 white line; the central position of the Co L_3 white line; the intensity ratio of the 855eV peak over the 857eV peak of Ni-L_3 white line are used to correlate the fine structure with the valence state of the element.

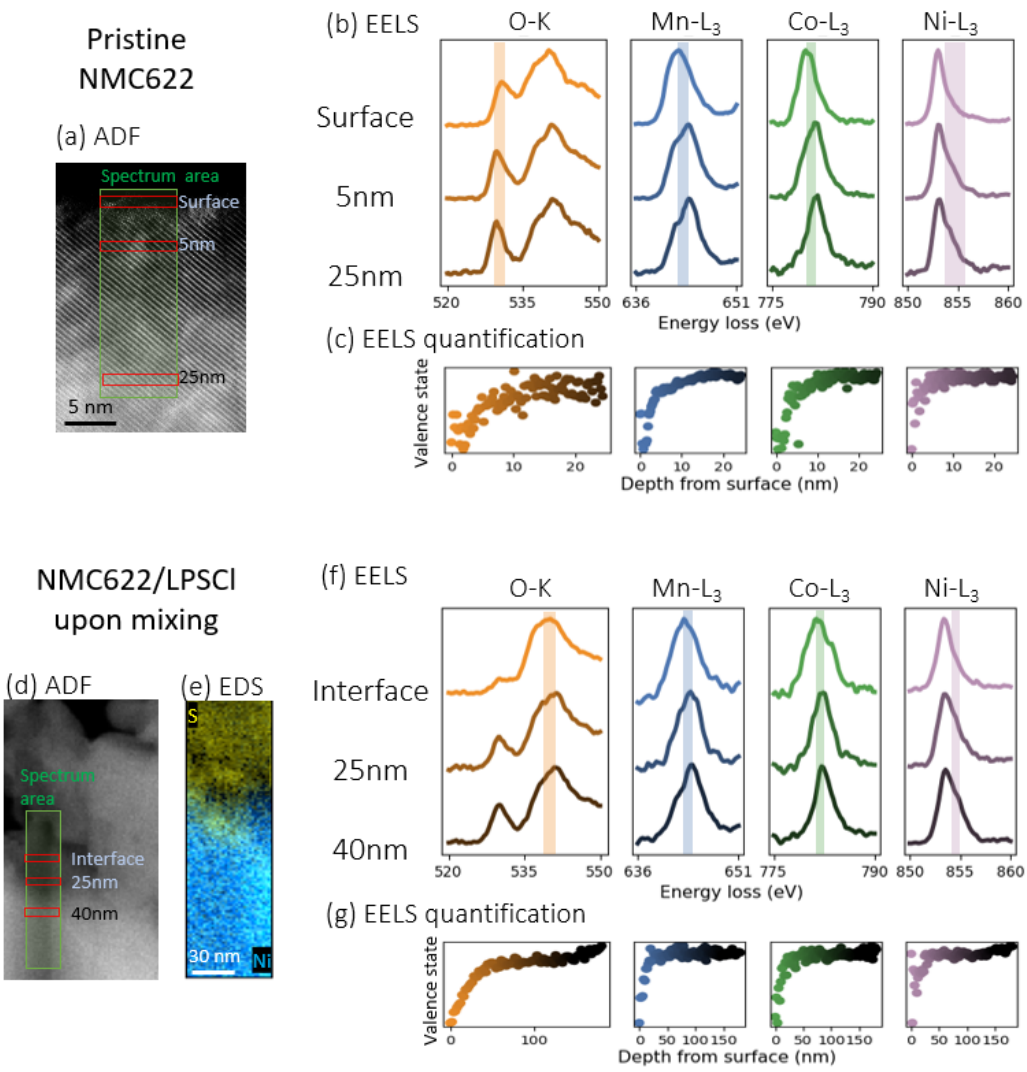


Figure 7.1: (a) Atomic-resolution ADF image of pristine NMC622 prepared by cryo-PFIB, the spectrum area is highlighted in green. (b) stacked EEL spectra from the surface, 5nm and 25nm, the fine structure changes are highlighted in the shaded area (c) EELS fine structure quantification, the valence state in arbitrary units is plotted against the depth from surface. (d) ADF image of NMC622/LPSCl upon mixing prepared by cryo-PFIB, and the (e) EDS map of Ni (blue) and S (yellow) from the corresponding spectrum area (f) stacked EEL spectra from the interface, 25nm and 40nm., (d) EELS fine structure quantification.

From the EELS quantification of valence states at different depths from the interface, reduction at the surface/interface can be observed. To compare the reaction penetration depths, the onset of the reduction layer is determined from when the exponential fitting of the valence states at different depths approaches 90% of the bulk value. The onset depth for each element is plotted in Figure 7.2 for both pristine NMC622 and uncycled NMC622/LPSCl interface. The

four elements show different reduction depth, especially O reduces much deeper than the TMs. For the study of reduction layer evolution at different conditions, the O reduction depth will be used for discussion as the relative intensity of O pre-peak to the main peak serves as a convenient indicator of the overall redox trend in TM oxides.

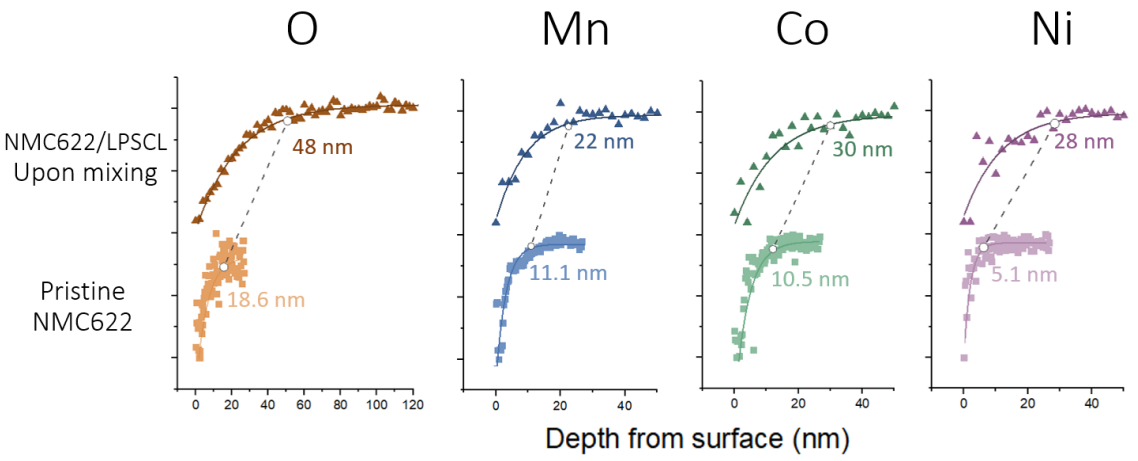


Figure 7.2: Quantification of EELS fine structure change of O, Mn, Co and Ni at pristine NMC622 surface and NMC6222/LPSCl interface.

It can be observed that the reduction of O, Mn, Co and Ni in the pristine sample happens within 20nm from the surface, while the reduction depth at the NMC622/LPSCl interface reaches up to 62nm for O. By comparing to the pristine cathode material, the further reduction layer of 40nm caused by the spontaneous redox reaction beyond the sample preparation damage has been highlighted. In the next section, the interfacial reaction upon cycling will be discussed.

7.3 Interfacial Electrochemical Reaction Upon Cycling

The charge-discharge profile for the first cycle of the NMC622/LPSCl/Li-In is shown in Figure 7.3. NMC622|LPSCl|Li-In cell was charged for 1 cycle under 20Mpa at C/20 rate. The composite cathode is a mixture of NMC622 and LPSCl in weight ratio of 70:30. The cell that has been charged to 4.3V vs. Li^+/Li with 198 mAh/g, 4.5V vs. Li^+/Li with 201 mAh/g, 4.8V vs. Li^+/Li with 204 mAh/g and discharged from 4.8V vs. Li^+/Li with 162 mAh/g capacity respectively. These 4 states

of charge (SoC) were chosen to study the effect of cycling on the interfacial redox reaction. A low coulombic efficiency of 79% is observed on the first cycle, which is attributed to the parasitic reactions between electrodes and electrolyte, irreversible electrolyte decomposition and contact loss due to volume change upon cycling.

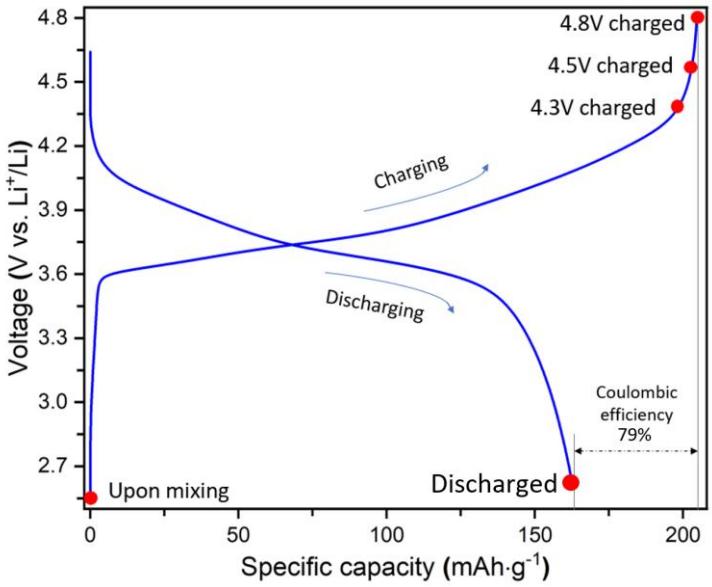


Figure 7.3: Cycling performance of NMC622/LPSCl/Li-In on the first cycle. (Cell running credit to Dr. Longlong Wang and Lechen Yang)

Figure 7.4-7.7 show the simultaneous EDS and EELS acquired on NMC622/LPSCl interface at different SoC: 4.3V vs. Li^+/Li charged, 4.5 vs. Li^+/Li charged, 4.8V vs. Li^+/Li charged, and discharged from 4.8V vs. Li^+/Li respectively. The spectrum image areas are highlighted in the ADF images. In a similar pattern of data, the EDS map of Ni and S locates the interface between NMC622 and LPSCl. EELS spectra at different depths from the interface are stacked and the depth-dependent energy shift of EELS fine structure is highlighted in the shaded area. Quantification of the fine structure change is performed and plotted underneath the corresponding EELS data.

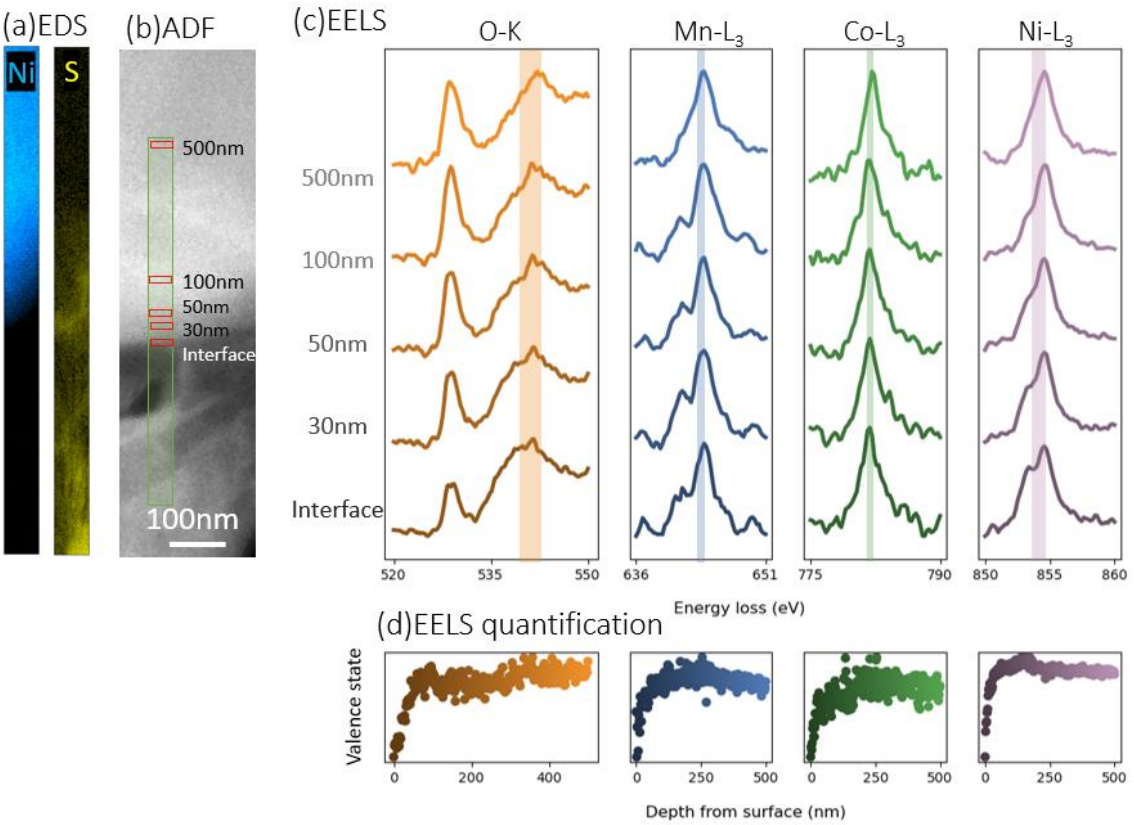


Figure 7.4: 4.3V vs. Li^+/Li charged: (a) EDS map of Ni (blue) from NMC622 and S (yellow) from argyrodite, (b) ADF image, the spectrum area is marked in green, from the red labelled area at 500nm, 100nm, 50nm and 30nm from the interface and at interface (c) EELS fine structure are highlighted in shaded area, (d) the EELS core-loss fine structure quantification, the valence state in arbitrary units is plotted against the depth from surface 0-500nm with step size of 2nm.

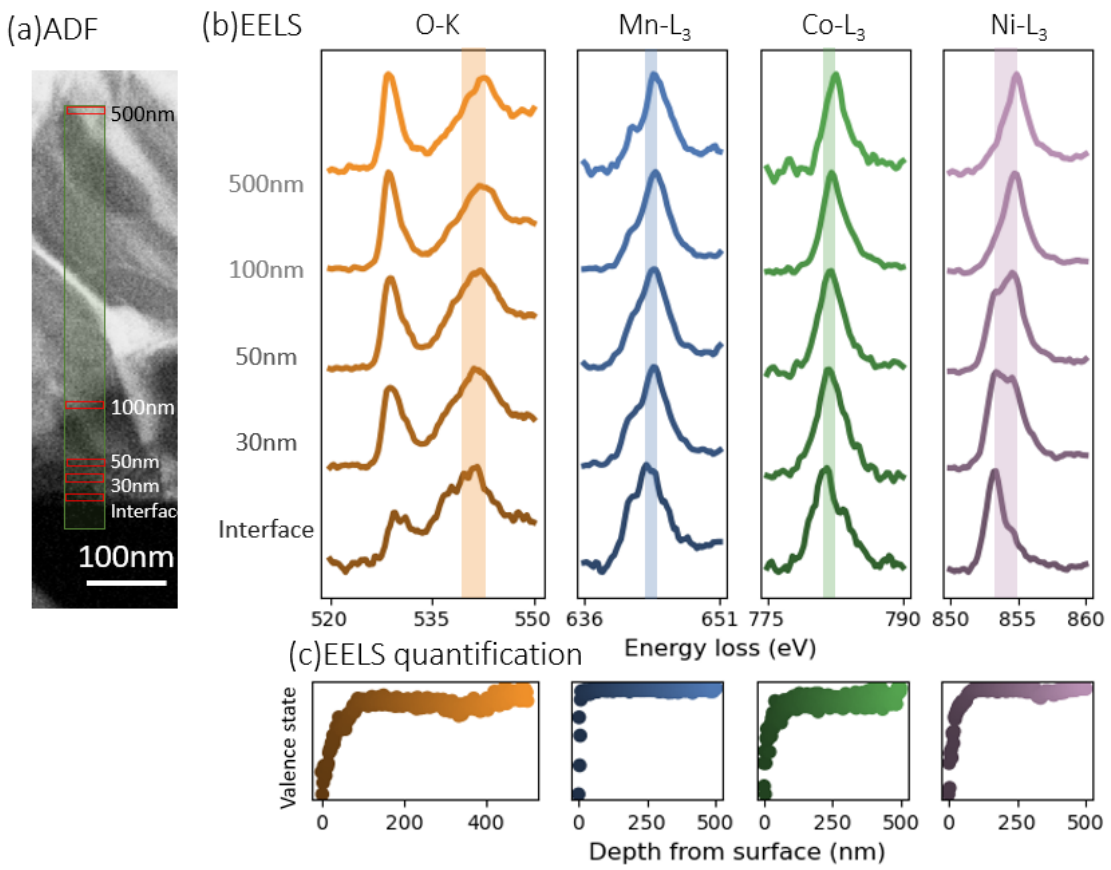


Figure 7.5: 4.5V vs. Li^+/Li charged: (a) ADF image, the spectrum area is marked in green, from the red labelled area at 500nm, 100nm, 50nm and 30nm from the interface and at interface (c) EELS fine structure are highlighted in shaded area, (d) the EELS core-loss fine structure quantification, the valence state in arbitrary units is plotted against the depth from surface 0-500nm with step size of 2nm.

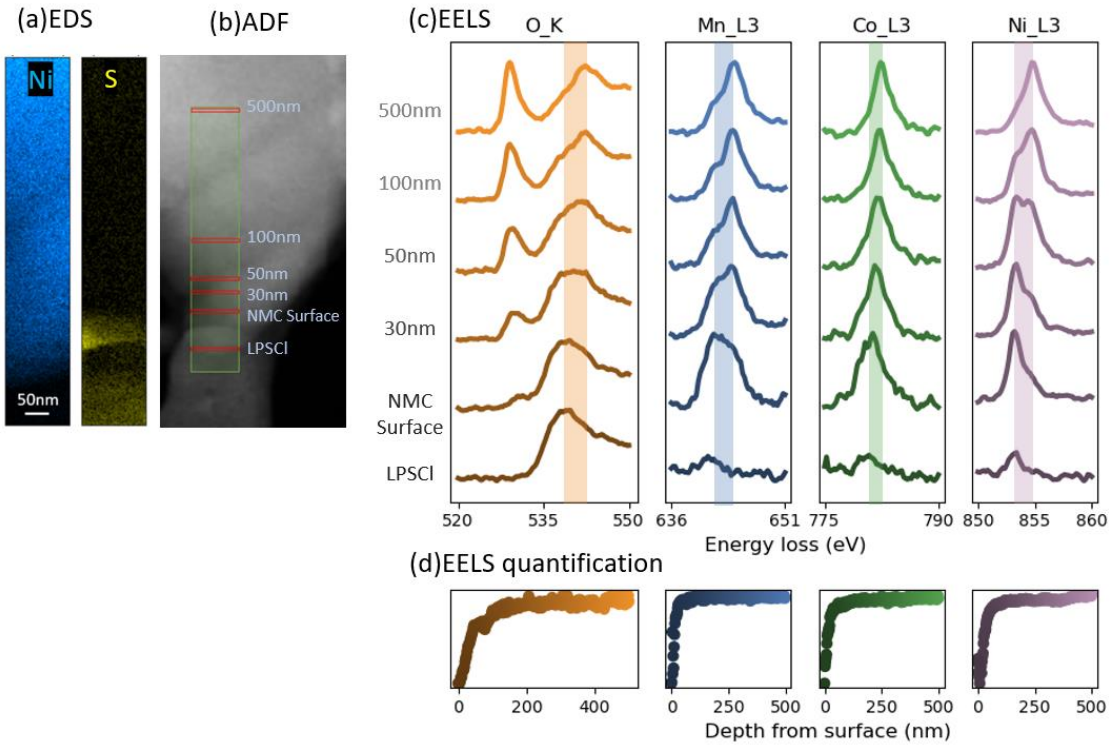


Figure 7.6: 4.8V vs. Li^+/Li charged: (a) EDS map of Ni (blue) from NMC622 and S (yellow) from argyrodite, (b) ADF image, the spectrum area is marked in green, from the red labelled area at 500nm, 100nm, 50nm and 30nm from the interface and at interface (c) EELS fine structure are highlighted in shaded area , (d) the EELS core-loss fine structure quantification, the valence state in arbitrary units is plotted against the depth from surface 0-500nm with step size of 2nm.

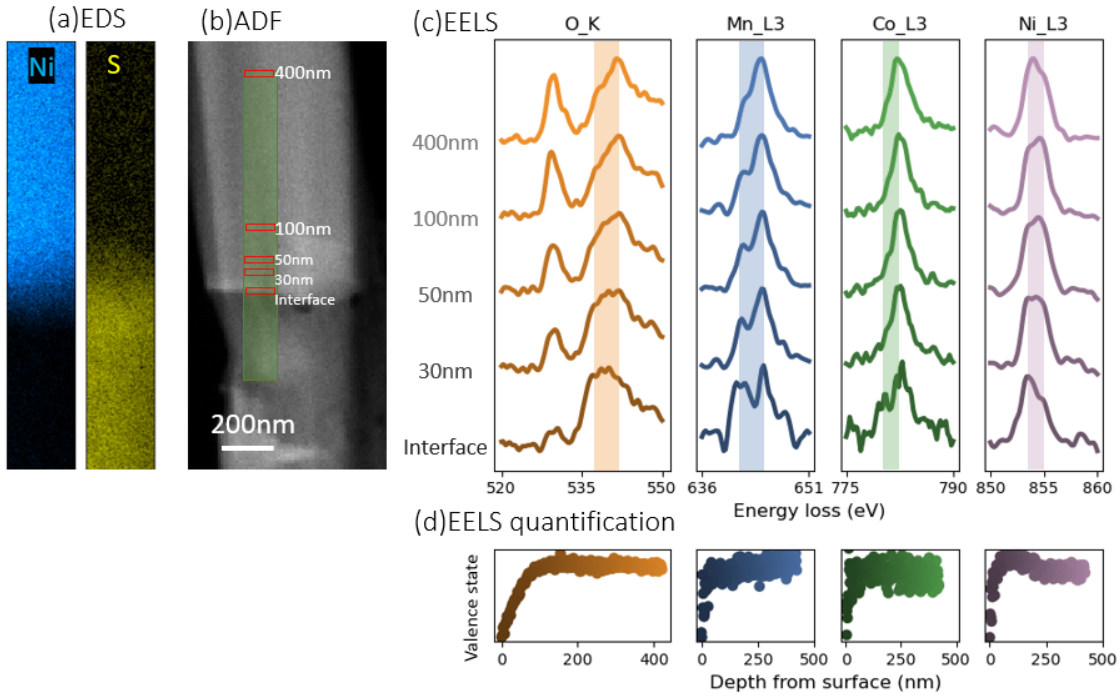


Figure 7.7: 4.8V vs. Li^+/Li discharged: (a) EDS map of Ni (blue) from NMC622 and S (yellow) from argyrodite, (b) ADF image, the spectrum area is marked in green, from the red labelled area at 500nm, 100nm, 50nm and 30nm from the interface and at interface (c) EELS fine structure are highlighted in shaded area , (d) the EELS core-loss fine structure quantification, the valence state in arbitrary units is plotted against the depth from surface 0-500nm with step size of 2nm.

For 4.3V vs. Li^+/Li, 4.5V vs. Li^+/Li and 4.8V vs. Li^+/Li charged state in Figure 7.4-7.6, the top EELS spectra are acquired at 500nm from the interface, representing the bulk of the NMC622 particle. Here, the high O-K pre-peak intensity relative to the main peak and the Ni L_3 peak shape aligns very well with the XAS data in literature. [273] For all 4 SoCs, as moving from the bulk towards the interface, the O-K pre-peak intensity drops, and an energy shift of Mn-L_3, Co-L_3 and Ni-L_3 towards lower energy loss can be observed, suggesting reduction of all 4 elements towards the interface.

Figure 7.8 compares the interfacial reduction layer depth evolution upon cycling. The spontaneous redox reaction from the mixed, uncycled sample from Figure 7.2 is included for comparison.

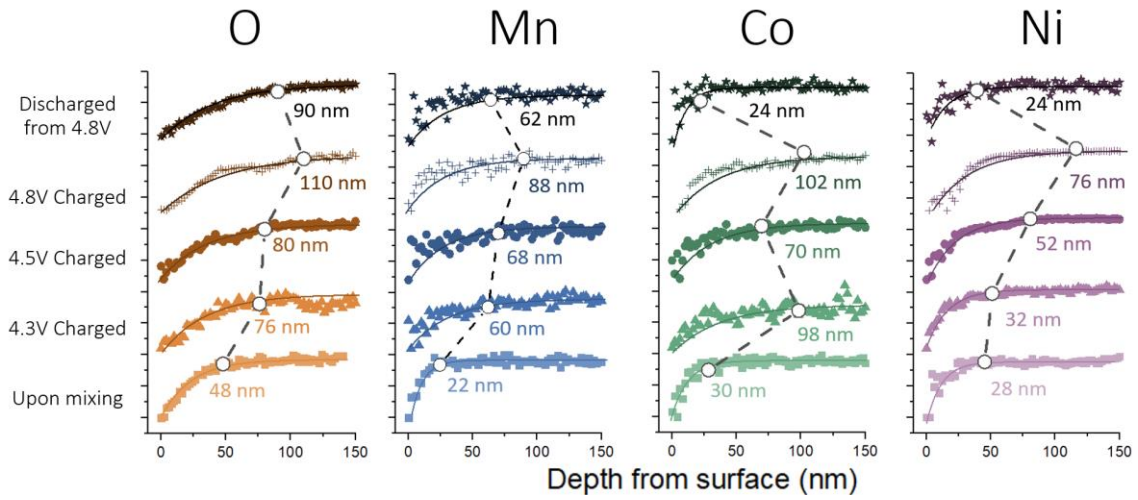


Figure 7.8: O, Mn, Co and Ni oxidation state as a function of depth from interface upon mixing, at 4.3V vs. Li^+/Li charged, 4.5V vs. Li^+/Li charged, 4.8V vs. Li^+/Li charged, and discharged from 4.8V vs. Li^+/Li.

The higher chemical reactivity between cathode and sulphide SEs at charged state have been reported from the increased interfacial impedance and thickening of the CEI layer, [333] which can be attributed to the structure instability of cathode in the delithiated state. [96] As expected, a significant deepening of the surface reduction can be observed on the 4.3V vs. Li^+/Li charged NMC622 compared to the uncycled sample, as a result of the electrochemical reaction between the LPSCl and charged NMC622.

As the voltage increases beyond 4.3V vs. Li^+/Li, NMC materials release oxygen and undergo irreversible structural changes which result in enhanced capacity fading. [333, 334] As a result of the structural change at high voltage, a further penetration of the reduction depth can be observed at 4.5V vs. Li^+/Li and 4.8V vs. Li^+/Li compared to the 4.3V vs. Li^+/Li.

A reversibility of the interfacial reduction layer can be observed from the decrease of the reduction area as NMC622 was discharged from 4.8V vs. Li^+/Li, which aligns well with the reversibility of the degradation products observed in XPS [330] and the lower interfacial impedance in the discharged state compared to the charged state. [335] Apart from the reversibility of the interfacial reduction, some other factors also contribute to the much thicker reduction area observed in the charged state compared to the discharged state.

The experiments were conducted ex situ, meaning the chemical reactions between NMC622 and LPSCl continued during sample transfer and preparation. In the case of a discharged sample, it was immediately discharged once it reached 4.8V vs. Li^+/Li and therefore the chemical reaction happens between discharged NMC622 and LPSCl. While for the charged sample, LPSCl interacts with the unstable delithiated NMC622, leading to more pronounced chemical reactions. Self-discharge can also happen on the charged samples that Li moves back from LPSCl to NMC622, which causes reduction on charged NMC622 surface. Therefore, the difference in reduction layer thickness between 4.8V vs. Li^+/Li charged and discharged from 4.8V vs. Li^+/Li can attribute to the reversibility of the interfacial redox reaction, higher chemical reactivity of charged NMC622 than discharged and also the self-discharge at charged states.

At highly charged state like 4.8V vs. Li^+/Li, not only aforementioned electrochemical and chemical reaction between NMC622 and LPSCl, but the self-decomposition would also occur. To distinguish the interfacial redox reaction between NMC622 and LPSCl, the 4.8V vs. Li^+/Li charged NMC622 in a conventional liquid electrolyte was used to highlight the role of LPSCl in the interfacial reaction with NMC622.

7.4 Comparison of Solid Electrolyte and Liquid Electrolyte

NMC622 was charged to 4.8V vs. Li^+/Li in a half cell with a $LiPF_6$ in EC/DMC liquid electrolyte with the same charging rate C/20. The cathode was dried in vacuum before the TEM lamellae lift-out, the further sample preparation was carried out identically to the other NMC622/LPSCl lamellae. Figure 7.9a shows the ADF image of the NMC622 particle surrounded by carbon black. The EELS scan area is marked by the green box on the NMC622 particle. The EELS fine structure change and the corresponding quantification are plotted in Figure 7.9b and c.

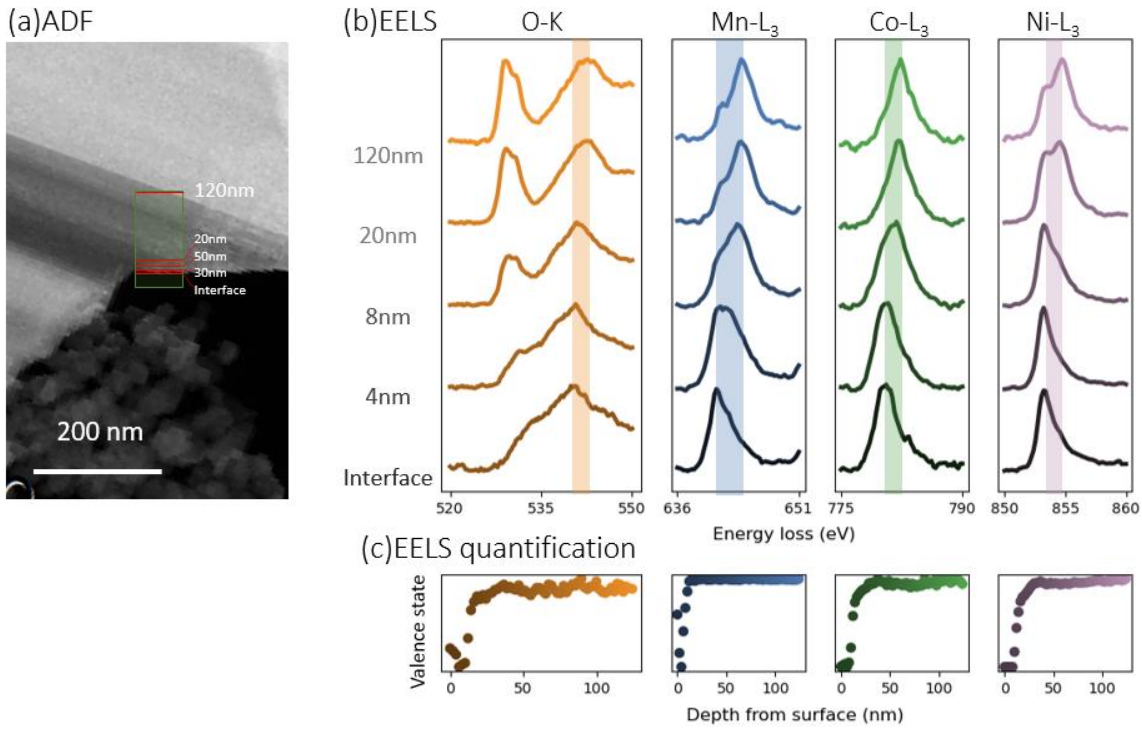


Figure 7.9: NMC622 charged with LiPF6 in EC/DMC to 4.8V vs. Li^+/Li: (a) ADF image, the spectrum area is marked in green, (b) EELS data at 120nm, 20nm, 8nm and 4nm from the interface and at the surface, (c) the EELS core-loss fine structure quantification at depths of 0-500nm from the surface with step size of 2nm. (The liquid cell running credit to Lijin An)

To compare the effect of SE and LE on the cathode surface reduction layer thickness, both the solid-state and liquid state cells were charged to the same charging voltage with the same charging rate. Another factor that needs to be considered for the comparison is the in-situ beam damage on the SE. Because the LE was not preserved due to the absence of cryo-transfer method, while SE was preserved through cryo-PFIB milling, the interaction of highly energised electron beam and SE generates heat in the vacuum chamber of TEM which is usually considered as a reducing environment, and can cause extra reduction on the cathode surface. Therefore, the EELS measurements should be made on bare NMC622 particles without contact with LE or SE to eliminate the difference in beam damage effect. The ADF image of Figure 7.10 (a) shows the EELS data was acquired in the area that is exposed to vacuum. It worth motioning that this

is different area but on the same particle of the 4.8V vs. Li^+/Li charged solid-state battery in Figure 7.6.

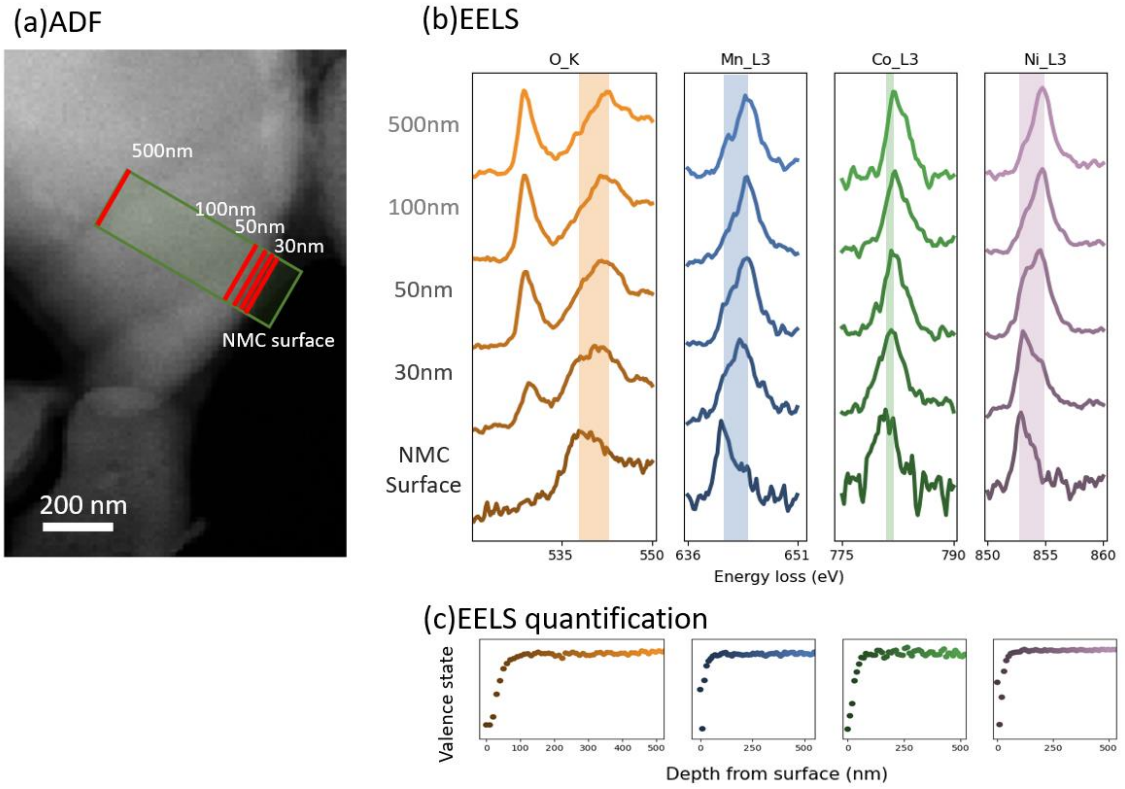


Figure 7.10: NMC622 charged with LPSCl to 4.8V vs. Li^+/Li: (a) ADF image, the spectrum area is marked in green, (b) EELS data at 500nm, 100nm, 50nm and 30nm from the interface and at the surface, (c) the EELS core-loss fine structure quantification at depths of 0-500nm from the surface with step size of 10nm.

Figure 7.11 shows the depth dependent valence state of O, Mn, Co and Ni from surface to bulk in solid-state LIB with LPSCl (bottom) and in the liquid electrolyte (top). Compared to the surface reduction layer of 110nm at 4.8V vs. Li^+/Li charged with contact with LPSCl in Figure 7.8, the reduction layer thickness has dropped to 74nm without the contact with LPSCl in Figure 7.11. This decrease of surface reduction layer from not having LPSCL in EELS scanning area confirms the in-situ beam damage on LSPCl. By comparing the reduction layer of bare NMC622 particles in solid- and liquid-state battery in Figure 7.11, the reduction depth of NMC622 is significantly deeper in solid-state battery than the conventional liquid cell.

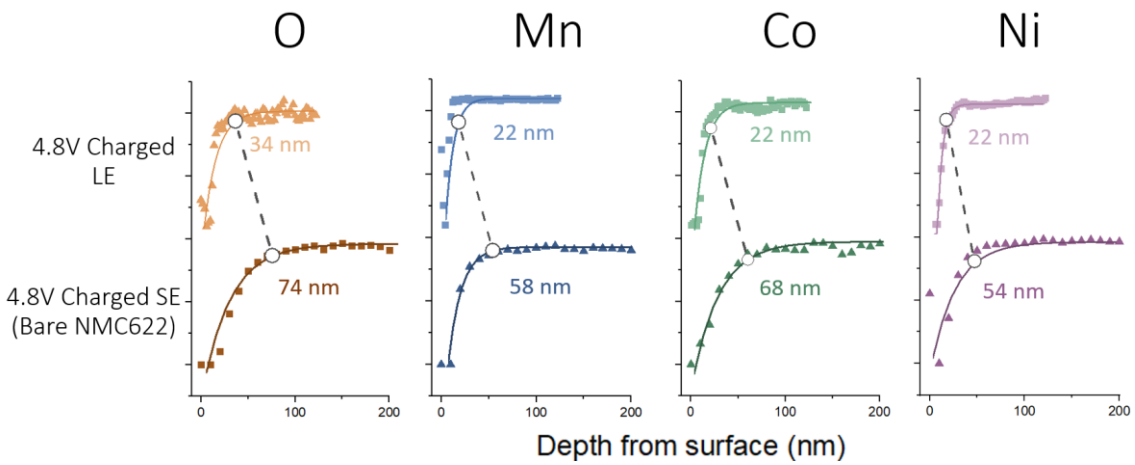


Figure 7.11: O, Mn, Co and Ni oxidation state change in liquid-state LIB with $LiPF_6$ in EC/DMC (top), solid-state LIB with argyrodite (bottom).

NMC622 in liquid-state battery shows merely 34nm of surface reduction layer at 4.8V vs. Li^+/Li charged state, which can be attributed to the redox reaction with liquid electrolyte and self-decomposition at high charging voltage such as O_2 release and structural degradation. Oxygen release from the layered $LiCoO_2$-type structure, has been intensively studied in conventional liquid batteries. [6, 24, 336, 337] Oxygen release from layered cathode materials, especially those containing Ni, is accompanied by a disorder in the crystal structure, leading to the formation of irreversible structure degradation characterized by spinel and/or rock-salt-type defects. [338]

In NMC622 charged with the sulphide solid electrolyte LPSCl, a much thicker reduction layer of 74nm can be observed. Apart from the same self-decomposition at high charging voltage, the comparison of the significantly deeper surface reduction layer can only be attributed to the parasitic reaction with LPSCl. To discuss the origin of the thick reduction layer caused by LPSCl, the elemental distribution across the interface has be studied through EDS quantification and will be discussed in the following section.

7.5 Element Migration at Interface

As plotted in Figure 7.6, the EELS still detected strong O-K edge from the argyrodite. The O signal is not from the overlapped NMC622 particle with LPSCl, because the absence of the pre-peak shows the O is not bonding with transition metals and the minimum signal of transitional metal ions suggests the O is no longer in NMC622 structure but migrated into the argyrodite.

Due to the limited spectral range in EELS, elemental quantification is performed using the simultaneously acquired EDS spectrum to trace the light element S, P, Cl from LPSCl. The EDS map and quantification are performed at the interface of 4.8V vs. Li^+/Li charged cell (Figure 7.12). In the elemental ratio quantification, a k factor was used for the Cliff-Lorimer method in EDS analysis to account for the atomic weight, ionisation cross section, fluorescent yield and the ratio of K_α line to the total K lines of a substance. However, the accuracy of k factor can be low when the sample consists of elements with greatly different atomic numbers, as is the case with the heavy elements in the cathode and the light elements in the electrolyte. Therefore, in this study, the elemental content derived from EDS quantification is not regarded as an absolute value. Instead, it is used to compare the distribution of elements across the scanned area.

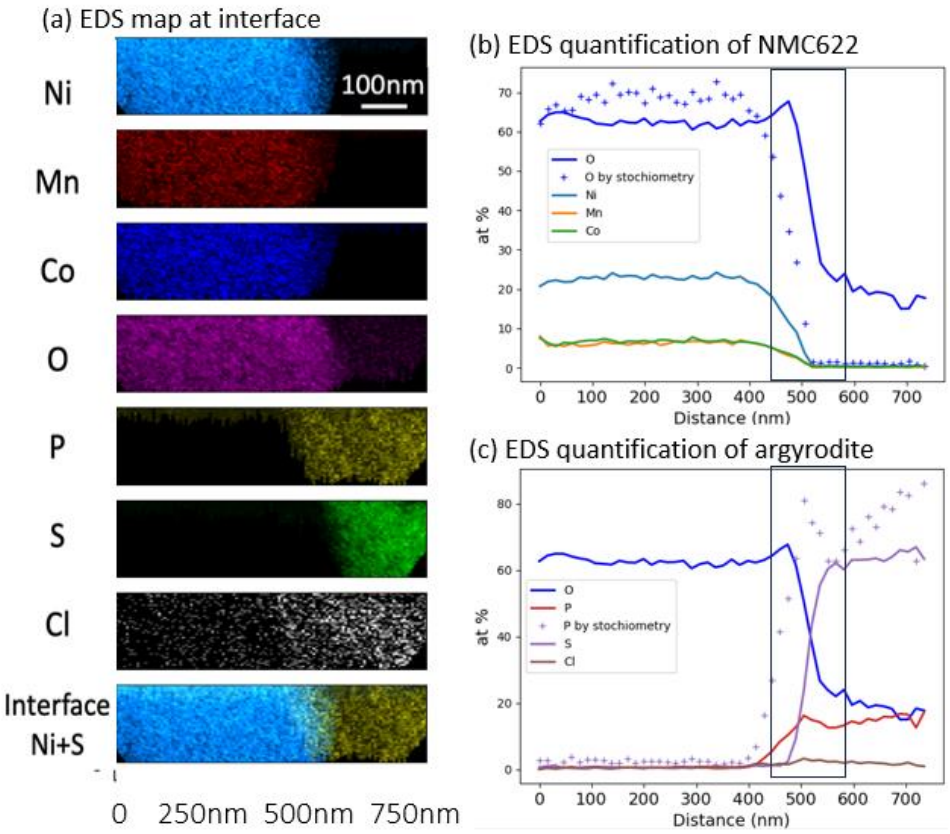


Figure 7.12 : (a) EDS map of Ni, Mn, Co, O, P, S, Cl and combined Ni & S; (b) elemental quantification of O, Mn, Co, Ni and calculated O content from Ni content-based stoichiometry; (c) elemental quantification of O, P, S, Cl and calculated S content from P content-based stoichiometry;

From the EDS map of O, Mn, Co and Ni in Figure 7.12a, which come from the cathode material, the Ni, Mn and Co show a similar distribution. However, the distribution of O does not follow the same trend. O expands across the interface into the LPSCl. As for the P, S and Cl elements from LPSCl, the distribution patterns are more complicated. To quantitively analyse the change in elemental distribution, the EDS map pixels are binned vertically to enhance the X-ray intensity for element quantification.

In the EDS quantification of O, Ni, Mn and Co in NMC622 in Figure 7.12b, the TM content remains stable in the bulk and all reduce to zero at distance of 500nm due to the thickness reduction at the particle surface. In contrast, the O enrichment is observed at the interface which doesn't follow the thickness profile. To highlight the migration of O, the O content is calculated based

on stoichiometry from the Ni content (plotted in blue '+') in the case of solely a thickness change. The comparison of experimental and calculated O content highlights the slight deficiency of O in the bulk of NMC622 and its segregation at the NMC622/LPSCl interface. Furthermore, there is a significant amount of O detected in the argyrodite phase, which suggests the cross-interface migration.

The O content is plotted together with P, S and Cl content in in Figure 7.12c. It is worth noting that in the interface region, at 400 - 500nm range on the EDS map, S content is significantly lower than P, suggesting S deficiency at interface. Interestingly, S deficiency happens in the same area as the O segregation. In addition, Cl deficiency can be observed on LPSCl. As the site disorder between Cl^- and S^{2-} anions gives rise to the good ionic conductivity of LPSCl, the Cl deficiency may suggest the low ionic conductivity of the interphase. Even though the bonding cannot be analysed directly in EDS, the result may suggest the P-O bond formation in LPSCl. Therefore, the deep penetration of the interfacial redox reaction between NMC622/LPSCl is suggested to be O segregation from NMC622 into LPSCl and formation of P-O bonds.

7.6 Conclusions

In summary, the spontaneous chemical reaction between NMC622/LPSCl has been confirmed using the comparison to pristine NMC622. The interfacial electrochemical reaction depth at 4 different charging states have been precisely measured for O, Mn, Co and Ni. The results show the penetration upon charging to 4.8V vs. Li^+/Li reached 110nm. Reversibility is also observed as the reduction layer depth reduces after discharge. Importantly, the redox reaction between cathode and sulphide solid electrolyte has been clearly differentiated from the self-decomposition by comparing to the NMC622 charged to the same voltage at same rate in a liquid electrolyte. The penetration of the reduction layer highlights that the sulphide solid electrolyte LPSCl induces significant interfacial parasitic reactions, especially in the charged state.

This phenomenon can be attributed to cross-interface O migration and S deficiency near the interface: the O in NMC622 migrates into argyrodite to replace the S in the PS_4^{3-} tetrahedra and form PO_4^{3-} which is energetically favourable. The O is more likely to leave the unstable delithiated layered structure which explains the growing interfacial redox reaction upon charging. For the future interfacial design, coating layer that allows Li ion mobility but forbids O ion migration would be beneficial to prevent the further penetration of interfacial reduction layer.

Chapter 8 Summary and Future Work

8.1 Summary

Improved interfacial design is critical in achieving better capacity retention and longer cycle life for SSLIBs. A detail characterisation method that can probe the near-nature state of interfacial redox reaction at high spatial and high energy resolution is essential to provide fundamental insight in the interfacial problems.

In this thesis, **chapter 4** detailed the development of an anaerobic transfer workflow from the glovebox to the TEM for the air-sensitive solid electrolyte LPSCl. This process was validated through studies on the effects of air exposure, where LPSCl was shown to undergo hydrolysis reactions with H2S gas release upon exposure to air, leading to a significant increase in oxygen content and a decrease in the S:P element ratio. EDS mapping demonstrated oxygen segregation on the particle surface and chlorine inhomogeneity post-exposure. Notable morphological changes were also observed, including the loss of clear contours and the formation of cavities in the particles. Additionally, the electron beam damage was studied on LPSCl which causes charge-induced particle tilting and amorphisation.

Chapter 5 compared different methods in preparing TEM lamellae for cathode/SE interface study and found PFIB milling is the optimal technique that provides precise site-specific control, ensuring uniformly thin, non-overlapping interface lamellae for detailed STEM analysis. Performing PFIB milling at cryogenic temperatures has proven beneficial in significantly minimising the ion beam-induced structural degradation to merely 2nm on pristine NMC622, as evidenced through atomic-resolution HAADF image. Furthermore, the highly beam-sensitive delithiated NMC622 was successfully preserved using the ambient-temperature lift-out and cryo-thinning procedure. Through EELS characterisation on the pristine, charged and discharged NMC622, Ni was found to take the main role of charge compensation, while some redox activity is also observed on Co. Mn, being the structure stabiliser, remains unchanged through cycling.

Chapter 6 focused on the quantification methodology of the EELS fine structure. A model-based quantification method of the ELNES has proven to be highly effective in capturing subtle changes in the fine structure of O and TMs and providing a comprehensive understanding of the valence state change. Additionally, the chapter highlighted an intriguing observation: a rising post-L edge broad peak from Mn to Co and Ni. This phenomenon correlates to a 14 eV shift in the partial cross section relative to the white line, as supported by Dirac-based GOS calculations. This finding prompts important question regarding the conventional data processing in aligning the partial cross section onset.

Chapter 7 conducted a systematic analysis of the interfacial redox reactions between NMC622 and LPSCl across various states of charge. Initially, the spontaneous redox reaction occurring between NMC622 and LPSCl was verified by comparison with pristine NMC622. As the charging voltage increased, the depth of the interfacial reduction layer on NMC622 continuously expanded, reaching up to 110nm at 4.8V vs. Li^+/Li. Notably, reversibility in these reactions was observed, with the reduction layer depth decreasing upon discharge. A crucial aspect of this study was to highlight the role of LPSCl in these interfacial reactions. This was achieved by comparing the NMC622 under identical charging conditions but in a liquid electrolyte, which exhibited only a 34nm deep reduction layer. The pronounced penetration of the reduction layer induced by LPSCl was attributed to the migration of oxygen across the interface, which replaces S in P-S bonds, leading to the formation of P-O bonds. Therefore, the future coating layer design should focus on prohibiting the O migration across interface while allowing Li ion mobility.

Overall, this thesis has established a comprehensive workflow for high-resolution imaging and spectroscopy to study the interfacial redox reactions in solid-state Li-ion battery materials. This workflow starts from anaerobic sample transfer, to TEM interface lamella lift-out, and finally tailored data processing methodology of EELS fine structure. Using this methodology, the evolution of the interfacial redox reactions between NMC622 and LPSCl has been precisely

characterised across various state of charge. Based on these systematic investigations, recommendations have been made for future interfacial designs, aimed at enhancing the performance and longevity of solid-state batteries.

8.2 Future work

Nano-beam characterisation of structural change at NMC622/LPSCl interface

Building on the systematic study of valence state changes and chemical distribution at the NMC622/LPSCl interface, future research should focus on the structural degradation to gain deeper insights into the mechanisms driving the penetration of the reduction layer on the cathode surface and its reversibility between charge and discharge cycles. However, this investigation presents several experimental challenges.

Firstly, nano-beam electron diffraction (NBED), which provides 2D mapping of crystallographic information, requires tilting to align with the zone axis. Electron backscatter diffraction (EBSD) can be used to identify the zone axis before lamella lift-out, but EBSD mapping requires high electron dose that can be detrimental to battery materials, particularly in charged states. Otherwise, if lift-out lamella is made without prior knowledge of the zone axis, the chance of having the optimal zone axis close to the incident beam direction is very low, especially given the limited tilting range of the TEM vacuum transfer holder. (Tilt X: -12˚ to 12˚, Tilt Y: -5˚ to 5 ˚)

Another challenge involves the differing optimal thickness requirements for NBED and EELS analysis. EELS requires exceptionally thin specimens to minimise multiple scattering effects, ideally thinner than the mean free path, whereas NBED benefits from a thicker specimen to

enhance the signal-to-noise ratio. Consequently, performing EELS and nano-beam diffraction on the same lamella may not be feasible due to these conflicting requirements.

The energy shift of partial cross section of Ni from metal to oxides

Further exploration into the energy shift of the partial cross section relative to the white line could significantly enhance our understanding of electron excitations in transition metals and improve the data analysis quality. As discussed in Chapter 6, the white line represents the 2p-3d excitation, whereas the partial cross section involves excitations to all other delocalized bands and vacant states, including the 4s orbital. Despite the complexity in calculating the TM-L edge ab initio due to the intricate alterations in the valence state electrons, notable progress can be made by examining the oxygen edge.

The O-K pre-peak is indicative of electron transitions to hybridised O 2p and TM 3d orbitals, while the main peak typically corresponds to transitions involving hybridised O 2p and Ni 4s orbitals and other states. Ab initio calculations of the O-K edge are feasible and can offer valuable insights. By comparing the computed O-K edge spectra of O^{2-} in an uncoordinated state with experimental data acquired from NiO, discrepancies can be attributed to hybridisation with Ni 4s orbitals and other delocalised states.

Additionally, XPS could provide a more detailed observation of the energy shifts in the partial cross section's onset energy, as it is more sensitive to the covalency than EELS and XAS. Therefore, integrating XPS into future studies is also proposed to deepen our understanding of these energy shifts and the underlying electron dynamics.

The effect of coating on the interfacial redox reaction

This thesis has outlined a comprehensive workflow from sample handling, TEM specimen preparation, data acquisition, and processing, all tailored to facilitate precise and

straightforward measurements of the interfacial redox reaction layer thickness. This established workflow allows for an efficient evaluation of different interfacial designs. Moreover, the versatility of this workflow extends beyond battery materials, offering significant benefits to the study of other solid-solid interfaces.

Reference

1. Goodenough, J.B. and K.-S. Park, *The Li-ion rechargeable battery: a perspective.* Journal of the American Chemical Society, 2013. **135**(4): p. 1167-1176.

2. Mizushima, K., et al., *LixCoO2 (0< x<-1): A new cathode material for batteries of high energy density.* Materials Research Bulletin, 1980. **15**(6): p. 783-789.

3. Wang, L., et al., *Reviving lithium cobalt oxide-based lithium secondary batteries-toward a higher energy density.* Chemical Society Reviews, 2018. **47**(17): p. 6505-6602.

4. Mendiboure, A., C. Delmas, and P. Hagenmuller, *New layered structure obtained by electrochemical deintercalation of the metastable LiCoO2 (O2) variety.* Materials research bulletin, 1984. **19**(10): p. 1383-1392.

5. Xia, H., et al., *Phase transitions and high-voltage electrochemical behavior of LiCoO2 thin films grown by pulsed laser deposition.* Journal of The Electrochemical Society, 2007. **154**(4): p. A337.

6. Chebiam, R., et al., *Comparison of the chemical stability of the high energy density cathodes of lithium-ion batteries.* Electrochemistry communications, 2001. **3**(11): p. 624-627.

7. Venkatraman, S., Y. Shin, and A. Manthiram, *Phase relationships and structural and chemical stabilities of charged Li1− x CoO2− δ and Li1− x Ni0. 85Co0. 15 O 2− δ cathodes.* Electrochemical and solid-state letters, 2002. **6**(1): p. A9.

8. Jiang, Y., et al., *Origins of capacity and voltage fading of LiCoO 2 upon high voltage cycling.* Journal of Materials Chemistry A, 2019. **7**(36): p. 20824-20831.

9. He, P., H. Yu, and H. Zhou, *Layered lithium transition metal oxide cathodes towards high energy lithium-ion batteries.* Journal of Materials Chemistry, 2012. **22**(9): p. 3680-3695.

10. Thackeray, M.M., et al., *Lithium insertion into manganese spinels.* Materials Research Bulletin, 1983. **18**(4): p. 461-472.

11. Yu, F., et al., *Spinel LiMn2O4 cathode materials in wide voltage window: Single-crystalline versus polycrystalline.* Crystals, 2022. **12**(3): p. 317.

12. Kim, H.-S., B.-W. Cho, and W.-I. Cho, *Cycling performance of LiFePO4 cathode material for lithium secondary batteries.* Journal of power sources, 2004. **132**(1-2): p. 235-239.

13. Nitta, N., et al., *Li-ion battery materials: present and future.* Materials today, 2015. **18**(5): p. 252-264.

14. Aurbach, D., et al., *On the capacity fading of LiCoO2 intercalation electrodes:: the effect of cycling, storage, temperature, and surface film forming additives.* Electrochimica Acta, 2002. **47**(27): p. 4291-4306.

15. Gauthier, M., et al., *Electrode–electrolyte interface in Li-ion batteries: current understanding and new insights.* The journal of physical chemistry letters, 2015. **6**(22): p. 4653-4672.

16. Cherkashinin, G., et al., *Electron spectroscopy study of Li [Ni, Co, Mn] O2/electrolyte interface: electronic structure, interface composition, and device implications.* Chemistry of Materials, 2015. **27**(8): p. 2875-2887.

17. Rougier, A., P. Gravereau, and C. Delmas, *Optimization of the composition of the Li1− z Ni1+ z O 2 electrode materials: structural, magnetic, and electrochemical studies.* Journal of The Electrochemical Society, 1996. **143**(4): p. 1168.

18. Arai, H., et al., *Thermal behavior of Li1− yNiO2 and the decomposition mechanism.* Solid State Ionics, 1998. **109**(3-4): p. 295-302.

19. Ohzuku, T. and Y. Makimura, *Layered lithium insertion material of LiCo1/3Ni1/3Mn1/3O2 for lithium-ion batteries.* Chemistry letters, 2001. **30**(7): p. 642-643.

20. Xu, J., et al., *A review of Ni-based layered oxides for rechargeable Li-ion batteries.* Journal of Materials Chemistry A, 2017. **5**(3): p. 874-901.

21. Kalyani, P. and N. Kalaiselvi, *Various aspects of LiNiO2 chemistry: A review.* Science and technology of advanced materials, 2005. **6**(6): p. 689.

22. Ngala, J.K., et al., *The synthesis, characterization and electrochemical behavior of the layered LiNi 0.4 Mn 0.4 Co 0.2 O 2 compound.* Journal of materials chemistry, 2004. **14**(2): p. 214-220.

23. Myung, S.-T., et al., *Nickel-rich layered cathode materials for automotive lithium-ion batteries: achievements and perspectives.* ACS Energy Letters, 2017. **2**(1): p. 196-223.

24. Jung, R., et al., *Oxygen release and its effect on the cycling stability of LiNixMnyCozO2 (NMC) cathode materials for Li-ion batteries.* Journal of The Electrochemical Society, 2017. **164**(7): p. A1361.

25. Chakraborty, A., et al., *Layered cathode materials for lithium-ion batteries: review of computational studies on LiNi1–x–y Co x Mn y O2 and LiNi1–x–y Co x Al y O2.* Chemistry of Materials, 2020. **32**(3): p. 915-952.

26. Zhang, S.S., *Problems and their origins of Ni-rich layered oxide cathode materials.* Energy Storage Materials, 2020. **24**: p. 247-254.

27. Tian, C., F. Lin, and M.M. Doeff, *Electrochemical characteristics of layered transition metal oxide cathode materials for lithium ion batteries: surface, bulk behavior, and thermal properties.* Accounts of chemical research, 2017. **51**(1): p. 89-96.

28. Goodenough, J.B. and Y. Kim, *Challenges for rechargeable Li batteries.* Chemistry of materials, 2010. **22**(3): p. 587-603.

29. Tarascon, J.-M. and M. Armand, *Issues and challenges facing rechargeable lithium batteries*, in *Materials for sustainable energy: a collection of peer-reviewed research and review articles from Nature Publishing Group*. 2011, World Scientific. p. 171-179.

30. Jeong, S.-K., et al., *Suppression of dendritic lithium formation by using concentrated electrolyte solutions.* Electrochemistry Communications, 2008. **10**(4): p. 635-638.

31. Camacho-Forero, L.E., T.W. Smith, and P.B. Balbuena, *Effects of high and low salt concentration in electrolytes at lithium–metal anode surfaces.* The Journal of Physical Chemistry C, 2017. **121**(1): p. 182-194.

32. Gong, C., et al., *Revealing the role of fluoride‐rich battery electrode interphases by operando transmission electron microscopy.* Advanced Energy Materials, 2021. **11**(10): p. 2003118.

33. Guo, J., et al., *Vinylene carbonate–LiNO3: a hybrid additive in carbonic ester electrolytes for SEI modification on Li metal anode.* Electrochemistry Communications, 2015. **51**: p. 59-63.

34. Janek, J. and W.G. Zeier, *A solid future for battery development.* Nature energy, 2016. **1**(9): p. 1-4.

35. Masquelier, C. and L. Croguennec, *Polyanionic (phosphates, silicates, sulfates) frameworks as electrode materials for rechargeable Li (or Na) batteries.* Chemical Reviews, 2013. **113**(8): p. 6552-6591.

36. Aono, H., et al., *Ionic conductivity of solid electrolytes based on lithium titanium phosphate.* Journal of the electrochemical society, 1990. **137**(4): p. 1023.

37. Yi, E., et al., *Materials that can replace liquid electrolytes in Li batteries: Superionic conductivities in Li1. 7Al0. 3Ti1. 7Si0. 4P2. 6O12. Processing combustion synthesized nanopowders to free standing thin films.* Journal of Power Sources, 2014. **269**: p. 577-588.

38. Arbi, K., et al., *High lithium ion conducting solid electrolytes based on NASICON Li1+ xAlxM2− x (PO4) 3 materials (M= Ti, Ge and 0 ⩽ x ⩽ 0.5).* Journal of the European Ceramic Society, 2015. **35**(5): p. 1477-1484.

39. Kotobuki, M. and M. Koishi, *Sol–gel synthesis of Li1. 5Al0. 5Ge1. 5 (PO4) 3 solid electrolyte.* Ceramics International, 2015. **41**(7): p. 8562-8567.

40. Tatsumisago, M., M. Nagao, and A. Hayashi, *Recent development of sulfide solid electrolytes and interfacial modification for all-solid-state rechargeable lithium batteries.* Journal of Asian Ceramic Societies, 2013. **1**(1): p. 17-25.

41. Bohnke, O., *The fast lithium-ion conducting oxides Li3xLa2/3− xTiO3 from fundamentals to application.* Solid State Ionics, 2008. **179**(1-6): p. 9-15.

42. Gao, X., et al., *Lithium atom and A-site vacancy distributions in lanthanum lithium titanate.* Chemistry of Materials, 2013. **25**(9): p. 1607-1614.

43. Li, Y., et al., *Optimizing Li+ conductivity in a garnet framework.* Journal of Materials Chemistry, 2012. **22**(30): p. 15357-15361.

44. Thangadurai, V., S. Narayanan, and D. Pinzaru, *Garnet-type solid-state fast Li ion conductors for Li batteries: critical review.* Chemical Society Reviews, 2014. **43**(13): p. 4714-4727.

45. Murugan, R., V. Thangadurai, and W. Weppner, *Fast lithium ion conduction in garnet-type Li7La3Zr2O12.* Angewandte Chemie International Edition, 2007. **46**(41): p. 7778-7781.

46. Awaka, J., et al., *Synthesis and structure analysis of tetragonal Li7La3Zr2O12 with the garnet-related type structure.* Journal of solid state chemistry, 2009. **182**(8): p. 2046-2052.

47. Geiger, C.A., et al., *Crystal chemistry and stability of "Li7La3Zr2O12" garnet: a fast lithium-ion conductor.* Inorganic chemistry, 2011. **50**(3): p. 1089-1097.

48. Allen, J.L., et al., *Effect of substitution (Ta, Al, Ga) on the conductivity of Li7La3Zr2O12.* Journal of Power Sources, 2012. **206**: p. 315-319.

49. Wolfenstine, J., et al., *Mechanical behavior of Li-ion-conducting crystalline oxide-based solid electrolytes: a brief review.* Ionics, 2018. **24**: p. 1271-1276.

50. Kanno, R. and M. Murayama, *Lithium ionic conductor thio-LISICON: the Li2 S GeS2 P 2 S 5 system.* Journal of the electrochemical society, 2001. **148**(7): p. A742.

51. Kamaya, N., et al., *A lithium superionic conductor.* Nature materials, 2011. **10**(9): p. 682-686.

52. Seino, Y., et al., *A sulphide lithium super ion conductor is superior to liquid ion conductors for use in rechargeable batteries.* Energy & Environmental Science, 2014. **7**(2): p. 627-631.

53. Zhang, S.S., *Liquid electrolyte lithium/sulfur battery: Fundamental chemistry, problems, and solutions.* Journal of Power Sources, 2013. **231**: p. 153-162.

54. Kraft, M.A., et al., *Influence of Lattice Polarizability on the Ionic Conductivity in the Lithium Superionic Argyrodites Li6PS5X (X = Cl, Br, I).* J Am Chem Soc, 2017. **139**(31): p. 10909-10918.

55. Deiseroth, H.J., et al., *Li6PS5X: a class of crystalline Li-rich solids with an unusually high Li+ mobility.* Angew Chem Int Ed Engl, 2008. **47**(4): p. 755-8.

56. Chen, H.M., C. Maohua, and S. Adams, *Stability and ionic mobility in argyrodite-related lithium-ion solid electrolytes.* Phys Chem Chem Phys, 2015. **17**(25): p. 16494-506.

57. De Klerk, N.J., I. Rosłoń, and M. Wagemaker, *Diffusion mechanism of Li argyrodite solid electrolytes for Li-ion batteries and prediction of optimized halogen doping: the effect of Li vacancies, halogens, and halogen disorder.* Chemistry of Materials, 2016. **28**(21): p. 7955-7963.

58. Auvergniot, J., et al., *Redox activity of argyrodite Li6PS5Cl electrolyte in all-solid-state Li-ion battery: an XPS study.* Solid State Ionics, 2017. **300**: p. 78-85.

59. Zhou, Y., et al., *Observation of interfacial degradation of Li6PS5Cl against lithium metal and LiCoO2 via in situ electrochemical Raman microscopy.* Batteries & supercaps, 2020. **3**(7): p. 647-652.

60. Kasemchainan, J., et al., *Critical stripping current leads to dendrite formation on plating in lithium anode solid electrolyte cells.* Nature materials, 2019. **18**(10): p. 1105-1111.

61. Chen, B., et al., *Insights into interfacial stability of Li6PS5Cl solid electrolytes with buffer layers.* Current Applied Physics, 2019. **19**(2): p. 149-154.

62. Chu, I.-H., et al., *Insights into the performance limits of the Li7P3S11 superionic conductor: a combined first-principles and experimental study.* ACS applied materials & interfaces, 2016. **8**(12): p. 7843-7853.

63. Lepley, N. and N. Holzwarth, *Modeling interfaces between solids: Application to Li battery materials.* Physical Review B, 2015. **92**(21): p. 214201.

64. Busche, M.R., et al., *Dynamic formation of a solid-liquid electrolyte interphase and its consequences for hybrid-battery concepts.* Nature chemistry, 2016. **8**(5): p. 426-434.

65. Mo, Y., S.P. Ong, and G. Ceder, *First principles study of the Li10GeP2S12 lithium super ionic conductor material.* Chemistry of Materials, 2012. **24**(1): p. 15-17.

66. Szu, S., M. Greenblatt, and L. Klein, *The effect of precursors on the ionic conductivity in lithium silicate gels.* Solid State Ionics, 1991. **46**(3-4): p. 291-297.

67. Richards, W.D., et al., *Interface stability in solid-state batteries.* Chemistry of Materials, 2016. **28**(1): p. 266-273.

68. Rea, J., et al., *High ionic conductivity in densified polycrystalline lithium nitride.* Materials Research Bulletin, 1979. **14**(6): p. 841-846.

69. Kim, S., et al., *A complex hydride lithium superionic conductor for high-energy-density all-solid-state lithium metal batteries.* Nature communications, 2019. **10**(1): p. 1081.

70. Tang, W.S., et al., *Stabilizing lithium and sodium fast-ion conduction in solid polyhedral-borate salts at device-relevant temperatures.* Energy Storage Materials, 2016. **4**: p. 79-83.

71. Tang, W.S., et al., *Stabilizing superionic-conducting structures via mixed-anion solid solutions of monocarba-closo-borate salts.* ACS Energy Letters, 2016. **1**(4): p. 659-664.

72. Matsuo, M., et al., *Lithium superionic conduction in lithium borohydride accompanied by structural transition.* Applied Physics Letters, 2007. **91**(22).

73. Duchêne, L., et al., *Status and prospects of hydroborate electrolytes for all-solid-state batteries.* Energy Storage Materials, 2020. **25**: p. 782-794.

74. Asano, T., et al., *Solid halide electrolytes with high lithium‐ion conductivity for application in 4 V class bulk‐type all‐solid‐state batteries.* Advanced Materials, 2018. **30**(44): p. 1803075.

75. Kwak, H., et al., *Emerging halide superionic conductors for all-solid-state batteries: Design, synthesis, and practical applications.* ACS Energy Letters, 2022. **7**(5): p. 1776-1805.

76. Muy, S., et al., *High-throughput screening of solid-state Li-ion conductors using lattice-dynamics descriptors.* Iscience, 2019. **16**: p. 270-282.

77. Wang, S., et al., *Lithium chlorides and bromides as promising solid‐state chemistries for fast ion conductors with good electrochemical stability.* Angewandte Chemie International Edition, 2019. **58**(24): p. 8039-8043.

78. Park, K.-H., et al., *High-voltage superionic halide solid electrolytes for all-solid-state Li-ion batteries.* ACS Energy Letters, 2020. **5**(2): p. 533-539.

79. Riegger, L.M., et al., *Lithium‐metal anode instability of the superionic halide solid electrolytes and the implications for solid‐state batteries.* Angewandte Chemie International Edition, 2021. **60**(12): p. 6718-6723.

80. Liang, J., et al., *Metal halide superionic conductors for all-solid-state batteries.* Accounts of Chemical Research, 2021. **54**(4): p. 1023-1033.

81. Lee, Y.-G., et al., *High-energy long-cycling all-solid-state lithium metal batteries enabled by silver–carbon composite anodes.* Nature Energy, 2020. **5**(4): p. 299-308.

82. Koç, T., et al., *In search of the best solid electrolyte-layered oxide pairing for assembling practical all-solid-state batteries.* ACS Applied Energy Materials, 2021. **4**(12): p. 13575-13585.

83. Arya, A. and A. Sharma, *Polymer electrolytes for lithium ion batteries: a critical study.* Ionics, 2017. **23**(3): p. 497-540.

84. Dias, F.B., L. Plomp, and J.B. Veldhuis, *Trends in polymer electrolytes for secondary lithium batteries.* Journal of Power Sources, 2000. **88**(2): p. 169-191.

85. Ramesh, S., T. Winie, and A. Arof, *Investigation of mechanical properties of polyvinyl chloride–polyethylene oxide (PVC–PEO) based polymer electrolytes for lithium polymer cells.* European polymer journal, 2007. **43**(5): p. 1963-1968.

86. Wu, F., et al., *Polymer electrolytes and interfaces toward solid-state batteries: Recent advances and prospects.* Energy Storage Materials, 2020. **33**: p. 26-54.

87. Venkatasetty, H. *Lithium-polymer electrolyte rechargeable batteries*. in *Fifteenth Annual Battery Conference on Applications and Advances (Cat. No. 00TH8490)*. 2000. IEEE.

88. Barai, P., K. Higa, and V. Srinivasan, *Lithium dendrite growth mechanisms in polymer electrolytes and prevention strategies.* Physical Chemistry Chemical Physics, 2017. **19**(31): p. 20493-20505.

89. Zhao, Q., et al., *Solid-state polymer electrolytes with in-built fast interfacial transport for secondary lithium batteries.* Nature Energy, 2019. **4**(5): p. 365-373.

90. Valøen, L.O. and J.N. Reimers, *Transport properties of LiPF6-based Li-ion battery electrolytes.* Journal of The Electrochemical Society, 2005. **152**(5): p. A882.

91. Li, Y., et al., *A lithium superionic conductor for millimeter-thick battery electrode.* Science, 2023. **381**(6653): p. 50-53.

92. Sakuda, A., A. Hayashi, and M. Tatsumisago, *Interfacial observation between LiCoO2 electrode and Li2S− P2S5 solid electrolytes of all-solid-state lithium secondary batteries using transmission electron microscopy.* Chemistry of Materials, 2010. **22**(3): p. 949-956.

93. Takada, K., *Progress and prospective of solid-state lithium batteries.* Acta Materialia, 2013. **61**(3): p. 759-770.

94. Takada, K., et al., *Interfacial phenomena in solid-state lithium battery with sulfide solid electrolyte.* Solid State Ionics, 2012. **225**: p. 594-597.

95. Koerver, R., et al., *Chemo-mechanical expansion of lithium electrode materials–on the route to mechanically optimized all-solid-state batteries.* Energy & Environmental Science, 2018. **11**(8): p. 2142-2158.

96. Zhu, Y., X. He, and Y. Mo, *First principles study on electrochemical and chemical stability of solid electrolyte–electrode interfaces in all-solid-state Li-ion batteries.* Journal of Materials Chemistry A, 2016. **4**(9): p. 3253-3266.

97. Xiao, Y., et al., *Understanding interface stability in solid-state batteries.* Nature Reviews Materials, 2020. **5**(2): p. 105-126.

98. Koerver, R., et al., *Capacity fade in solid-state batteries: interphase formation and chemomechanical processes in nickel-rich layered oxide cathodes and lithium thiophosphate solid electrolytes.* Chemistry of Materials, 2017. **29**(13): p. 5574-5582.

99. Oh, G., et al., *Bulk-type all solid-state batteries with 5 V class LiNi0. 5Mn1. 5O4 cathode and Li10GeP2S12 solid electrolyte.* Chemistry of Materials, 2016. **28**(8): p. 2634-2640.

100. Lacivita, V., et al., *Ab initio investigation of the stability of electrolyte/electrode interfaces in all-solid-state Na batteries.* Journal of Materials Chemistry A, 2019. **7**(14): p. 8144-8155.

101. Dean, J.A., *Lange's handbook of chemistry*. 1999: Citeseer.

102. Visbal, H., et al., *The effect of diamond-like carbon coating on LiNi0. 8Co0. 15Al0. 05O2 particles for all solid-state lithium-ion batteries based on Li2S–P2S5 glass-ceramics.* Journal of Power Sources, 2016. **314**: p. 85-92.

103. Culver, S.P., et al., *On the functionality of coatings for cathode active materials in thiophosphate‐based all‐solid‐state batteries.* Advanced Energy Materials, 2019. **9**(24): p. 1900626.

104. Sun, N., et al., *Surface‐to‐Bulk Synergistic Modification of Single Crystal Cathode Enables Stable Cycling of Sulfide‐Based All‐Solid‐State Batteries at 4.4 V.* Advanced Energy Materials, 2022. **12**(29): p. 2200682.

105. Fujii, Y., et al., *Reaction mechanism of FePS3 electrodes in all-solid-state lithium secondary batteries using sulfide-based solid electrolytes.* Journal of The Electrochemical Society, 2018. **165**(13): p. A2948.

106. Groh, M.F., et al., *Interface Instability in LiFePO4–Li3+ x P1–x Si x O4 All-Solid-State Batteries.* Chemistry of Materials, 2018. **30**(17): p. 5886-5895.

107. Vardar, G., et al., *Structure, chemistry, and charge transfer resistance of the interface between Li7La3Zr2O12 electrolyte and LiCoO2 cathode.* Chemistry of Materials, 2018. **30**(18): p. 6259-6276.

108. Rietveld, H.M., *A profile refinement method for nuclear and magnetic structures.* Journal of applied Crystallography, 1969. **2**(2): p. 65-71.

109. Suga, S., A. Sekiyama, and C. Tusche, *Photoelectron spectroscopy*. 2021: Springer.

110. Wang, C., et al., *Manipulating interfacial nanostructure to achieve high‐performance all‐solid‐state lithium‐ion batteries.* Small Methods, 2019. **3**(10): p. 1900261.

111. Okumura, T., et al., *Depth-resolved X-ray absorption spectroscopic study on nanoscale observation of the electrode–solid electrolyte interface for all solid state lithium ion batteries.* Journal of Materials Chemistry, 2011. **21**(27): p. 10051-10060.

112. Chen, K., et al., *Effect of introducing interlayers into electrode/electrolyte interface in all-solid-state battery using sulfide electrolyte.* Solid State Ionics, 2018. **327**: p. 150-156.

113. Li, X., et al., *Unravelling the chemistry and microstructure evolution of a cathodic interface in sulfide-based all-solid-state Li-ion batteries.* ACS Energy Letters, 2019. **4**(10): p. 2480-2488.

114. Zhou, H., et al., *Fast Lithium Intercalation Mechanism on Surface‐Modified Cathodes for Lithium‐Ion Batteries.* Advanced Energy Materials, 2023. **13**(44): p. 2302402.

115. Hirayama, M., et al., *Surface characterization of LiFePO4 epitaxial thin films by X-ray/neutron reflectometry.* Electrochemistry, 2010. **78**(5): p. 413-415.

116. Browning, J.F., et al., *In situ determination of the liquid/solid interface thickness and composition for the Li ion cathode LiMn1. 5Ni0. 5O4.* ACS applied materials & interfaces, 2014. **6**(21): p. 18569-18576.

117. Wang, H., et al., *In situ neutron techniques for studying lithium ion batteries*, in *Polymers for Energy Storage and Delivery: Polyelectrolytes for Batteries and Fuel Cells*. 2012, ACS Publications. p. 91-106.

118. Shimizu, R., et al., *Unraveling the Stable Cathode Electrolyte Interface in all Solid‐State Thin‐Film Battery Operating at 5 V.* Advanced Energy Materials, 2022. **12**(31): p. 2201119.

119. Zhang, Q., et al., *The surface triple-coupling on single crystalline cathode for lithium ion batteries.* Nano Energy, 2021. **86**: p. 106096.

120. Grey, C.P. and Y.J. Lee, *Lithium MAS NMR studies of cathode materials for lithium-ion batteries.* Solid State Sciences, 2003. **5**(6): p. 883-894.

121. Grey, C.P. and N. Dupré, *NMR studies of cathode materials for lithium-ion rechargeable batteries.* Chemical reviews, 2004. **104**(10): p. 4493-4512.

122. Yu, C., et al., *Accessing the bottleneck in all-solid state batteries, lithium-ion transport over the solid-electrolyte-electrode interface.* Nature communications, 2017. **8**(1): p. 1086.

123. Chien, P.-H., et al., *Li distribution heterogeneity in solid electrolyte Li10GeP2S12 upon electrochemical cycling probed by 7Li MRI.* The journal of physical chemistry letters, 2018. **9**(8): p. 1990-1998.

124. Chatham, J.C. and S.J. Blackband, *Nuclear magnetic resonance spectroscopy and imaging in animal research.* IlAR Journal, 2001. **42**(3): p. 189-208.

125. Williams, D.B. and C.B. Carter, *The transmission electron microscope*, in *Transmission electron microscopy*. 1996, Springer. p. 3-17.

126. Shim, J.-H., S. Lee, and S.S. Park, *Effects of MgO coating on the structural and electrochemical characteristics of LiCoO2 as cathode materials for lithium ion battery.* Chemistry of Materials, 2014. **26**(8): p. 2537-2543.

127. Luo, L., et al., *Atomic resolution study of reversible conversion reaction in metal oxide electrodes for lithium-ion battery.* Acs Nano, 2014. **8**(11): p. 11560-11566.

128. Mohanty, D., et al., *Investigating phase transformation in the Li 1.2 Co 0.1 Mn 0.55 Ni 0.15 O 2 lithium-ion battery cathode during high-voltage hold (4.5 V) via magnetic, X-ray diffraction and electron microscopy studies.* Journal of Materials Chemistry A, 2013. **1**(20): p. 6249-6261.

129. Sharma, Y., et al., *Nanophase ZnCo2O4 as a high performance anode material for Li-ion batteries.* Advanced Functional Materials, 2007. **17**(15): p. 2855-2861.

130. Das, B., et al., *Nanoflake CoN as a high capacity anode for Li-ion batteries.* Solid State Ionics, 2009. **180**(17-19): p. 1061-1068.

131. Chan, C.K., et al., *High-performance lithium battery anodes using silicon nanowires.* Nature nanotechnology, 2008. **3**(1): p. 31-35.

132. Zhu, Y., et al., *In situ atomic-scale imaging of phase boundary migration in FePO4 microparticles during electrochemical lithiation.* Advanced materials, 2013. **25**(38): p. 5461-5466.

133. Ryoo, H., et al., *Frenkel-Defect-Mediated Chemical Ordering Transition in a Li–Mn–Ni Spinel Oxide.* Angewandte Chemie International Edition, 2015. **54**(27): p. 7963-7967.

134. Humphreys, C., R. Sandstrom, and J. Spencer. *Contrast enhancement from single atoms and crystals using energy analysis*. in *Proceedings of the 6th Annual SEM Symposium*. 1973.

135. Crewe, A., J. Langmore, and M. Isaacson, *Techniques in Electron Microscopy and Microprobe Analysis*. 1975, John Wiley and Sons New York.

136. Treacy, M., A. Howie, and C. Wilson, *Z contrast of platinum and palladium catalysts.* Philosophical Magazine A, 1978. **38**(5): p. 569-585.

137. De Graef, M., *Introduction to conventional transmission electron microscopy*. 2003: Cambridge university press.

138. Crewe, A., J. Wall, and J. Langmore, *Visibility of single atoms.* Uspekhi Fizicheskikh Nauk, 1971. **104**(1): p. 162-166.

139. Genevois, C., et al., *Insight into the atomic structure of cycled lithium-rich layered oxide Li1. 20Mn0. 54Co0. 13Ni0. 13O2 using HAADF STEM and electron nanodiffraction.* The Journal of Physical Chemistry C, 2015. **119**(1): p. 75-83.

140. Yu, H., et al., *Direct atomic‐resolution observation of two phases in the Li1. 2Mn0. 567Ni0. 166Co0. 067O2 cathode material for lithium‐ion batteries.* Angewandte Chemie International Edition, 2013. **52**(23): p. 5969-5973.

141. Van Dyck, D. and M.O. De Beeck, *A simple intuitive theory for electron diffraction.* Ultramicroscopy, 1996. **64**(1-4): p. 99-107.

142. Gu, L., et al., *Direct observation of lithium staging in partially delithiated LiFePO4 at atomic resolution.* Journal of the American Chemical Society, 2011. **133**(13): p. 4661-4663.

143. Zhu, C., et al., *Size‐dependent staging and phase transition in LiFePO4/FePO4.* Advanced Functional Materials, 2014. **24**(3): p. 312-318.

144. McCalla, E., et al., *Visualization of O–O peroxo-like dimers in high-capacity layered oxides for Li-ion batteries.* Science, 2015. **350**(6267): p. 1516-1521.

145. McCalla, E., et al., *Reversible Li-intercalation through oxygen reactivity in Li-rich Li-Fe-Te oxide materials.* Journal of The Electrochemical Society, 2015. **162**(7): p. A1341.

146. Nayak, P.K., et al., *Al doping for mitigating the capacity fading and voltage decay of layered Li and Mn‐rich cathodes for Li‐Ion batteries.* Advanced Energy Materials, 2016. **6**(8): p. 1502398.

147. Li, T., et al., *Degradation mechanisms and mitigation strategies of nickel-rich NMC-based lithium-ion batteries.* Electrochemical Energy Reviews, 2020. **3**: p. 43-80.

148. Liu, H., et al., *Spatially resolved surface valence gradient and structural transformation of lithium transition metal oxides in lithium-ion batteries.* Physical Chemistry Chemical Physics, 2016. **18**(42): p. 29064-29075.

149. Lee, S.Y., et al., *Revisiting primary particles in layered lithium transition‐metal oxides and their impact on structural degradation.* Advanced Science, 2019. **6**(6): p. 1800843.

150. Ganesh, K., et al., *D-STEM: A parallel electron diffraction technique applied to nanomaterials.* Microscopy and Microanalysis, 2010. **16**(5): p. 614-621.

151. Thackeray, M., et al., *Comments on the structural complexity of lithium-rich Li1+ xM1− xO2 electrodes (M= Mn, Ni, Co) for lithium batteries.* Electrochemistry Communications, 2006. **8**(9): p. 1531-1538.

152. Susai, F.A., et al., *Stabilizing Ni-rich high energy cathodes for advanced lithium-ion batteries: the case of LiNi 0.9 Co 0.1 O 2.* Journal of Materials Chemistry A, 2023. **11**(24): p. 12958-12972.

153. Maiti, S., et al., *Modification of Li-and Mn-rich cathode materials via formation of the rock-salt and spinel surface layers for steady and high-rate electrochemical performances.* ACS applied materials & interfaces, 2020. **12**(29): p. 32698-32711.

154. Hughes, L., et al., *Correlative analysis of structure and chemistry of LixFePO4 platelets using 4D-STEM and X-ray ptychography.* Materials Today, 2022. **52**: p. 102-111.

155. O'Leary, C., et al., *Phase reconstruction using fast binary 4D STEM data.* Applied Physics Letters, 2020. **116**(12).

156. Lazić, I., E.G. Bosch, and S. Lazar, *Phase contrast STEM for thin samples: Integrated differential phase contrast.* Ultramicroscopy, 2016. **160**: p. 265-280.

157. Shibata, N., et al., *Direct visualization of local electromagnetic field structures by scanning transmission electron microscopy.* Accounts of chemical research, 2017. **50**(7): p. 1502-1512.

158. Wang, H., et al., *The development of iDPC-STEM and its application in electron beam sensitive materials.* Molecules, 2022. **27**(12): p. 3829.

159. Shen, B., et al., *Atomic spatial and temporal imaging of local structures and light elements inside zeolite frameworks.* Advanced Materials, 2020. **32**(4): p. 1906103.

160. Liu, B., et al., *Direct Observation of Li‐Ion Transport Heterogeneity Induced by Nanoscale Phase Separation in Li‐rich Cathodes of Solid‐State Batteries.* Angewandte Chemie International Edition, 2022. **61**(40): p. e202209626.

161. Wang, L., et al., *In-situ visualization of the space-charge-layer effect on interfacial lithium-ion transport in all-solid-state batteries.* Nature Communications, 2020. **11**(1): p. 5889.

162. Hoppe, W., *Beugung im inhomogenen primärstrahlwellenfeld. i. prinzip einer phasenmessung von elektronenbeungungsinterferenzen.* Acta Crystallographica Section A: Crystal Physics, Diffraction, Theoretical and General Crystallography, 1969. **25**(4): p. 495-501.

163. Lozano, J.G., et al., *Low-dose aberration-free imaging of Li-rich cathode materials at various states of charge using electron ptychography.* Nano letters, 2018. **18**(11): p. 6850-6855.

164. Yoon, D., et al., *Imaging Li Vacancies in a Li-Ion Battery Cathode Material by Depth Sectioning Multi-slice Electron Ptychographic Reconstructions*. 2023, Oxford University Press US.

165. Hu, X., et al., *Atomic scale imaging of structural variations in La (1-x)/3LixNbO3 (0 ⩽ x ⩽ 0.13) solid electrolytes.* Acta Materialia, 2017. **123**: p. 167-176.

166. Yang, P., et al., *Phosphorus enrichment as a new composition in the solid electrolyte interphase of high-voltage cathodes and its effects on battery cycling.* Chemistry of Materials, 2015. **27**(21): p. 7447-7451.

167. Ruthemann, G., *Direct energy Losses of Fast Electrons by Transmission Through Thin Sheets.* Naturwissenschaften, 1941. **29**: p. 648.

168. Mollenstedt, G., *Die elektrostatische Linse als hochauflosender Geschwindigkeitsanalysator.* Optik, 1949. **5**: p. 499-517.

169. Tiemeijer, P., et al., *Using a monochromator to improve the resolution in TEM to below 0.5 Å. Part I: Creating highly coherent monochromated illumination.* Ultramicroscopy, 2012. **114**: p. 72-81.

170. Brink, H., et al., *A sub-50 meV spectrometer and energy filter for use in combination with 200 kV monochromated (S) TEMs.* Ultramicroscopy, 2003. **96**(3-4): p. 367-384.

171. Freitag, B., et al., *Breaking the spherical and chromatic aberration barrier in transmission electron microscopy.* Ultramicroscopy, 2005. **102**(3): p. 209-214.

172. Rossouw, D. and G.A. Botton, *Plasmonic response of bent silver nanowires for nanophotonic subwavelength waveguiding.* Physical Review Letters, 2013. **110**(6): p. 066801.

173. Egoavil, R., et al., *Atomic resolution mapping of phonon excitations in STEM-EELS experiments.* Ultramicroscopy, 2014. **147**: p. 1-7.

174. Krivanek, O.L., et al., *Vibrational spectroscopy in the electron microscope.* Nature, 2014. **514**(7521): p. 209-212.

175. Qi, R., et al., *Measuring phonon dispersion at an interface.* Nature, 2021. **599**(7885): p. 399-403.

176. Gadre, C.A., et al., *Nanoscale imaging of phonon dynamics by electron microscopy.* Nature, 2022. **606**(7913): p. 292-297.

177. Lazar, S., et al., *Materials science applications of HREELS in near edge structure analysis and low-energy loss spectroscopy.* Ultramicroscopy, 2003. **96**(3-4): p. 535-546.

178. Erni, R. and N.D. Browning, *The impact of surface and retardation losses on valence electron energy-loss spectroscopy.* Ultramicroscopy, 2008. **108**(2): p. 84-99.

179. Bosman, M., et al., *Mapping surface plasmons at the nanometre scale with an electron beam.* Nanotechnology, 2007. **18**(16): p. 165505.

180. Raza, S., et al., *Blueshift of the surface plasmon resonance in silver nanoparticles studied with EELS.* Nanophotonics, 2013. **2**(2): p. 131-138.

181. Wu, Y., et al., *Infrared plasmonics: STEM-EELS characterization of Fabry-Pérot resonance damping in gold nanowires.* Physical Review B, 2020. **101**(8): p. 085409.

182. Hachtel, J.A., A.R. Lupini, and J.C. Idrobo, *Exploring the capabilities of monochromated electron energy loss spectroscopy in the infrared regime.* Scientific Reports, 2018. **8**(1): p. 5637.

183. Miyata, T., et al., *Measurement of vibrational spectrum of liquid using monochromated scanning transmission electron microscopy–electron energy loss spectroscopy.* Journal of Electron Microscopy, 2014. **63**(5): p. 377-382.

184. Sigle, W., et al., *Delithiation study of LiFePO4 crystals using electron energy-loss spectroscopy.* Electrochemical and Solid-State Letters, 2009. **12**(8): p. A151.

185. Schuster, M.E., et al., *Charging and discharging behavior of solvothermal LiFePO4 cathode material investigated by combined EELS/NEXAFS study.* Chemistry of Materials, 2014. **26**(2): p. 1040-1047.

186. Graetz, J., et al., *An electron energy-loss spectrometry study of charge compensation in LiNi0. 8Co0. 2O2.* The Journal of Physical Chemistry B, 2003. **107**(13): p. 2887-2891.

187. Huang, J.Y., et al., *In situ observation of the electrochemical lithiation of a single SnO2 nanowire electrode.* Science, 2010. **330**(6010): p. 1515-1520.

188. Liu, Y., et al., *In situ transmission electron microscopy observation of pulverization of aluminum nanowires and evolution of the thin surface Al2O3 layers during lithiation–delithiation cycles.* Nano letters, 2011. **11**(10): p. 4188-4194.

189. Wang, Z., et al., *In situ STEM-EELS observation of nanoscale interfacial phenomena in all-solid-state batteries.* Nano letters, 2016. **16**(6): p. 3760-3767.

190. Zhang, W., et al., *Kinetic pathways of ionic transport in fast-charging lithium titanate.* Science, 2020. **367**(6481): p. 1030-1034.

191. Gao, P., et al., *Atomic-scale tracking of a phase transition from spinel to rocksalt in lithium manganese oxide.* Chemistry of Materials, 2017. **29**(3): p. 1006-1013.

192. Han, B., et al., *Poor stability of Li2CO3 in the solid electrolyte interphase of a lithium‐metal anode revealed by cryo‐electron microscopy.* Advanced Materials, 2021. **33**(22): p. 2100404.

193. Yuan, Y., et al., *The application of in situ liquid cell TEM in advanced battery research.* 2023.

194. Gong, C., S. Pu, and A.W. Robertson, *In Situ Transmission Electron Microscopy for Studying Lithium-Ion Batteries.* Advances in Sustainable Energy: Policy, Materials and Devices, 2021: p. 545-569.

195. Brazier, A., et al., *First cross-section observation of an all solid-state lithium-ion "nanobattery" by transmission electron microscopy.* Chemistry of Materials, 2008. **20**(6): p. 2352-2359.

196. Santhanagopalan, D., et al., *Interface limited lithium transport in solid-state batteries.* The journal of physical chemistry letters, 2014. **5**(2): p. 298-303.

197. Morino, Y., H. Tsukasaki, and S. Mori, *Microscopic Degradation Mechanism of Argyrodite-Type Sulfide at the Solid Electrolyte–Cathode Interface.* ACS Applied Materials & Interfaces, 2023. **15**(19): p. 23051-23057.

198. Morino, Y. and S. Kanada, *Electrochemical and material analyses for sulfide-based solid electrolyte–cathode interface under high voltage.* Journal of Power Sources, 2021. **509**: p. 230376.

199. Morino, Y., *Degradation rate at the Solid–Solid interface of sulfide-based solid Electrolyte–Cathode active material.* Journal of Power Sources, 2022. **541**: p. 231672.

200. Zhu, Y., X. He, and Y. Mo, *Origin of outstanding stability in the lithium solid electrolyte materials: insights from thermodynamic analyses based on first-principles calculations.* ACS applied materials & interfaces, 2015. **7**(42): p. 23685-23693.

201. Tsukasaki, H., et al., *Deterioration process of argyrodite solid electrolytes during exposure to humidity-controlled air.* Journal of Power Sources, 2022. **524**: p. 231085.

202. Cliff, G. and G.W. Lorimer, *The quantitative analysis of thin specimens.* Journal of Microscopy, 1975. **103**(2): p. 203-207.

203. Goldstein, J.I., *Quantitative X-ray analysis in the electron microscope.* Scanning Electron Microscopy 1977, 1977. **1**: p. 315-324.

204. Egerton, R., P. Li, and M. Malac, *Radiation damage in the TEM and SEM.* Micron, 2004. **35**(6): p. 399-409.

205. Egerton, R.F., et al., *Basic questions related to electron-induced sputtering in the TEM.* Ultramicroscopy, 2010. **110**(8): p. 991-997.

206. Kohl, H. and L. Reimer, *Transmission electron microscopy: physics of image formation*. 2008: Springer.

207. Thomas, L., *Light-element analysis with electrons and X-rays in a high-resolution STEM.* Ultramicroscopy, 1985. **18**(1-4): p. 173-184.

208. Hayashida, M., et al., *Estimation of suitable condition for observing copper–phthalocyanine crystalline film by transmission electron microscopy.* Nuclear Instruments and Methods in Physics Research Section B: Beam Interactions with Materials and Atoms, 2006. **248**(2): p. 273-278.

209. Cazaux, J., *Correlations between ionization radiation damage and charging effects in transmission electron microscopy.* Ultramicroscopy, 1995. **60**(3): p. 411-425.

210. Glaeser, R.M., *Retrospective: radiation damage and its associated "information limitations".* J Struct Biol, 2008. **163**(3): p. 271-6.

211. Egerton, R., P. Crozier, and P. Rice, *Electron energy-loss spectroscopy and chemical change.* Ultramicroscopy, 1987. **23**(3-4): p. 305-312.

212. Lozano, J.G., et al., *Low-Dose Aberration-Free Imaging of Li-Rich Cathode Materials at Various States of Charge Using Electron Ptychography.* Nano Lett, 2018. **18**(11): p. 6850-6855.

213. Jones, L. *Absolute Integrator*. [cited 2020 May]; v1.6.4:[Available from: http://lewysjones.com/software/absolute-integrator/.

214. Pan, M. and P. Crozier, *Quantitative imaging and diffraction of zeolites using a slow-scan CCD camera.* Ultramicroscopy, 1993. **52**(3-4): p. 487-498.

215. Schäfer, P., et al., *Manipulation of plant innate immunity and gibberellin as factor of compatibility in the mutualistic association of barley roots with Piriformospora indica.* The Plant Journal, 2009. **59**(3): p. 461-474.

216. Henderson, R. and R.M. Glaeser, *Quantitative analysis of image contrast in electron micrographs of beam-sensitive crystals.* Ultramicroscopy, 1985. **16**(2): p. 139-150.

217. Egerton, R. and S. Cheng, *Measurement of local thickness by electron energy-loss spectroscopy.* Ultramicroscopy, 1987. **21**(3): p. 231-244.

218. Egerton, R.F., *Electron energy-loss spectroscopy in the electron microscope*. 2011: Springer Science & Business Media.

219. Isaacson, M. and D. Johnson, *The microanalysis of light elements using transmitted energy loss electrons.* Ultramicroscopy, 1975. **1**(1): p. 33-52.

220. Varlot, K., et al., *Towards sub-nanometer scale EELS analysis of polymers in the TEM.* Ultramicroscopy, 1997. **68**(2): p. 123-133.

221. Jiang, N. and J.C. Spence, *On the dose-rate threshold of beam damage in TEM.* Ultramicroscopy, 2012. **113**: p. 77-82.

222. Zan, R., et al., *Control of radiation damage in MoS2 by graphene encapsulation.* ACS nano, 2013. **7**(11): p. 10167-10174.

223. Henriksen, C., J.K. Mathiesen, and D.B. Ravnsbæk, *Improving capacity and rate capability of Li-ion cathode materials through ball milling and carbon coating–Best practice for research purposes.* Solid State Ionics, 2020. **344**: p. 115152.

224. Cronau, M., et al., *Ionic conductivity versus particle size of ball‐milled sulfide‐based solid electrolytes: strategy towards optimized composite cathode performance in all‐solid‐state batteries.* Batteries & Supercaps, 2022. **5**(6): p. e202200041.

225. Rajagopal, R., Y. Subramanian, and K.-S. Ryu, *Improving the electrochemical performance of cathode composites using different sized solid electrolytes for all solid-state lithium batteries.* RSC advances, 2021. **11**(52): p. 32981-32987.

226. Wang, D., et al., *High performance amorphous-Si@ SiOx/C composite anode materials for Li-ion batteries derived from ball-milling and in situ carbonization.* Journal of Power Sources, 2014. **256**: p. 190-199.

227. Hassoun, J., et al., *Ternary Sn–Co–C Li-ion battery electrode material prepared by high energy ball milling.* Electrochemistry communications, 2007. **9**(8): p. 2075-2081.

228. Melngailis, J., *Focused ion beam technology and applications.* Journal of Vacuum Science & Technology B: Microelectronics Processing and Phenomena, 1987. **5**(2): p. 469-495.

229. Assayag, G.B., et al., *Localized thinning of GaAs/GaAlAs nanostructures by a combined scanning electron micrograph/focus ion beam system for high‐quality cross‐sectional transmission electron microscopy samples.* Journal of Vacuum Science & Technology B: Microelectronics and Nanometer Structures Processing, Measurement, and Phenomena, 1993. **11**(3): p. 531-535.

230. Basile, D. *Specimen Preparation for Transmission Electron Microscopy of Materials-III*. in *Mater. Res. Soc. Symp. Proc.* 1992.

231. Dickson, N., et al. *Investigation into bake-reversible low-level ESD-induced leakage*. in *Microelectronics Manufacturing and Reliability*. 1993. SPIE.

232. Hull, R., et al., *Microscopic studies of semiconductor lasers utilizing a combination of transmission electron microscopy, electroluminescence imaging, and focused ion beam sputtering.* Applied physics letters, 1993. **62**(26): p. 3408-3410.

233. Kirk, E. *Cross-sectional transmission electron microscopy of precisely selected regions from semiconductor devices*. in *Microscopy of Semiconducting Materials Conference, Oxford, UK, 10-13 April 1989*. 1989.

234. Stevie, F., et al., *Applications of focused ion beams in microelectronics production, design and development.* Surface and interface analysis, 1995. **23**(2): p. 61-68.

235. Szot, J., et al., *Focused ion beam micromachining for transmission electron microscopy specimen preparation of semiconductor laser diodes.* Journal of Vacuum Science & Technology B: Microelectronics and Nanometer Structures Processing, Measurement, and Phenomena, 1992. **10**(2): p. 575-579.

236. Tarutani, M., Y. Takai, and R. Shimizu, *Application of the focused-ion-beam technique for preparing the cross-sectional sample of chemical vapor deposition diamond thin film for high-resolution transmission electron microscope observation.* Japanese Journal of Applied Physics Part 2 Letters, 1992. **31**: p. L1305-L1305.

237. Tomikawa, T.T.T. and S.-i.S.S.-i. Shikata, *Cross-sectional transmission electron microscopy observations and selected-area electron diffractions of interfaces of epitaxially grown diamond thin films on cubic boron nitride substrates.* Japanese journal of applied physics, 1993. **32**(9R): p. 3938.

238. Nakajima, K., et al., *Layer structure evaluation of multilayer x‐ray mirror by combination of focused ion beam etching and transmission electron microscopy.* Journal of Vacuum Science & Technology B: Microelectronics and Nanometer Structures Processing, Measurement, and Phenomena, 1993. **11**(6): p. 2127-2129.

239. Yamaguchi, A., M. Shibata, and T. Hashinaga, *Transmission electron microscopy specimen preparation technique using focused ion beam fabrication: Application to GaAs metal–semiconductor field effect transistors.* Journal of Vacuum Science & Technology B: Microelectronics and Nanometer Structures Processing, Measurement, and Phenomena, 1993. **11**(6): p. 2016-2020.

240. Merchan-Perez, A., et al., *Counting synapses using FIB/SEM microscopy: a true revolution for ultrastructural volume reconstruction.* Frontiers in neuroanatomy, 2009. **3**: p. 944.

241. Groeber, M.A., et al., *3D reconstruction and characterization of polycrystalline microstructures using a FIB–SEM system.* Materials characterization, 2006. **57**(4-5): p. 259-273.

242. Sivel, V., et al., *Application of the dual‐beam FIB/SEM to metals research.* Journal of Microscopy, 2004. **214**(3): p. 237-245.

243. Antoniou, N., et al. *Failure analysis of electronic material using cryogenic FIB-SEM*. in *Conference Proceedings from the 38th International Symposium for Testing and Failure Analysis, Phoenix, AR*. 2012.

244. Bassim, N., K. Scott, and L.A. Giannuzzi, *Recent advances in focused ion beam technology and applications.* Mrs Bulletin, 2014. **39**(4): p. 317-325.

245. Zhong, X., et al., *Comparing Xe+ pFIB and Ga+ FIB for TEM sample preparation of Al alloys: Minimising FIB‐induced artefacts.* Journal of Microscopy, 2021. **282**(2): p. 101-112.

246. Kelley, R., et al., *Xe+ FIB milling and measurement of amorphous silicon damage.* Microscopy and Microanalysis, 2013. **19**(S2): p. 862-863.

247. Giannuzzi, L.A., *Introduction to focused ion beams: instrumentation, theory, techniques and practice*. 2004: Springer Science & Business Media.

248. Overwijk, M., F. Van den Heuvel, and C. Bulle‐Lieuwma, *Novel scheme for the preparation of transmission electron microscopy specimens with a focused ion beam.* Journal of Vacuum Science & Technology B: Microelectronics and Nanometer Structures Processing, Measurement, and Phenomena, 1993. **11**(6): p. 2021-2024.

249. Calpa, M., et al., *Chemical stability of Li4PS4I solid electrolyte against hydrolysis.* Applied materials today, 2021. **22**: p. 100918.

250. Singer, C., et al., *Hydrolysis of Argyrodite Sulfide-Based Separator Sheets for Industrial All-Solid-State Battery Production.* ACS Applied Materials & Interfaces, 2022. **14**(21): p. 24245-24254.

251. Chen, Y.-T., et al., *Investigating dry room compatibility of sulfide solid-state electrolytes for scalable manufacturing.* Journal of Materials Chemistry A, 2022. **10**(13): p. 7155-7164.

252. Christensen, C.K., et al., *Beam damage in operando X-ray diffraction studies of Li-ion batteries.* Journal of Synchrotron Radiation, 2023. **30**(3).

253. Lin, F., et al., *Chemical and structural stability of lithium-ion battery electrode materials under electron beam.* Scientific Reports, 2014. **4**(1): p. 5694.

254. Wang, J., et al., *Improving cyclability of Li metal batteries at elevated temperatures and its origin revealed by cryo-electron microscopy.* Nature Energy, 2019. **4**(8): p. 664-670.

255. Zheng, H., J. Cui, and K. He, *A new cryo-FIB-TEM approach for damage-free characterization of garnet electrolytes in solid-state batteries.* Microscopy and Microanalysis, 2020. **26**(S2): p. 2784-2785.

256. Li, Y., et al., *Atomic structure of sensitive battery materials and interfaces revealed by cryo–electron microscopy.* Science, 2017. **358**(6362): p. 506-510.

257. Cheng, D., et al., *Unveiling the stable nature of the solid electrolyte interphase between lithium metal and LiPON via cryogenic electron microscopy.* Joule, 2020. **4**(11): p. 2484-2500.

258. Klumpe, S., et al., *Recent advances in gas injection system-free cryo-FIB lift-out transfer for cryo-electron tomography of multicellular organisms and tissues.* Microscopy Today, 2022. **30**(1): p. 42-47.

259. Kang, Y.-S., et al., *Revealing the structural degradation mechanism of the Ni-rich cathode surface: How thick is the surface?* Journal of power sources, 2021. **490**: p. 229542.

260. Hwang, S., et al., *Investigation of changes in the surface structure of Li x Ni0. 8Co0. 15Al0. 05O2 cathode materials induced by the initial charge.* Chemistry of Materials, 2014. **26**(2): p. 1084-1092.

261. Ruan, Y., et al., *Structural evolution and capacity degradation mechanism of LiNi0. 6Mn0. 2Co0. 2O2 cathode materials.* Journal of Power Sources, 2018. **400**: p. 539-548.

262. Li, T., et al., *Degradation mechanisms and mitigation strategies of nickel-rich NMC-based lithium-ion batteries.* Electrochemical Energy Reviews, 2020. **3**(1): p. 43-80.

263. Tornheim, A., et al., *Effect of electrolyte composition on rock salt surface degradation in NMC cathodes during high-voltage potentiostatic holds.* Nano Energy, 2019. **55**: p. 216-225.

264. Björklund, E., et al., *Cycle-Induced Interfacial Degradation and Transition-Metal Cross-Over in LiNi0. 8Mn0. 1Co0. 1O2–Graphite Cells.* Chemistry of Materials, 2022. **34**(5): p. 2034-2048.

265. Jung, S.K., et al., *Understanding the degradation mechanisms of LiNi0. 5Co0. 2Mn0. 3O2 cathode material in lithium ion batteries.* Advanced Energy Materials, 2014. **4**(1): p. 1300787.

266. Lin, F., et al., *Surface reconstruction and chemical evolution of stoichiometric layered cathode materials for lithium-ion batteries.* Nature communications, 2014. **5**(1): p. 3529.

267. Zhang, H., et al., *Oxygen loss in layered oxide cathodes for Li-ion batteries: Mechanisms, effects, and mitigation.* Chemical reviews, 2022. **122**(6): p. 5641-5681.

268. Hu, Z., et al., *Hole Distribution between the Ni 3 d and O 2 p Orbitals in Nd 2− x Sr x NiO 4− δ.* Physical Review B, 2000. **61**(5): p. 3739.

269. Yoon, W.-S., et al., *Investigation of the charge compensation mechanism on the electrochemically Li-Ion deintercalated Li1-x Co1/3Ni1/3Mn1/3O2 electrode system by combination of soft and hard X-ray absorption spectroscopy.* Journal of the American Chemical Society, 2005. **127**(49): p. 17479-17487.

270. Gilbert, B., et al., *Multiple scattering calculations of bonding and X-ray absorption spectroscopy of manganese oxides.* The Journal of Physical Chemistry A, 2003. **107**(16): p. 2839-2847.

271. Rask, J.H., B.A. Miner, and P.R. Buseck, *Determination of manganese oxidation states in solids by electron energy-loss spectroscopy.* Ultramicroscopy, 1987. **21**(4): p. 321-326.

272. Daulton, T.L. and B.J. Little, *Determination of chromium valence over the range Cr (0)–Cr (VI) by electron energy loss spectroscopy.* Ultramicroscopy, 2006. **106**(7): p. 561-573.

273. Tian, C., et al., *Depth-dependent redox behavior of LiNi0. 6Mn0. 2Co0. 2O2.* Journal of the Electrochemical society, 2018. **165**(3): p. A696-A704.

274. Hwang, S., et al., *Using real-time electron microscopy to explore the effects of transition-metal composition on the local thermal stability in charged Li x Ni y Mn z Co1–y–z O2 cathode materials.* Chemistry of Materials, 2015. **27**(11): p. 3927-3935.

275. CAUCHOIS, Y., *La spectroscopie X.* Zeitschrift für Kristallographie-Crystalline Materials, 1964. **120**(1-6): p. 182-211.

276. Su, D.S., et al., *High resolution EELS using monochromator and high performance spectrometer: comparison of V2O5 ELNES with NEXAFS and band structure calculations.* Micron, 2003. **34**(3-5): p. 235-238.

277. Mitterbauer, C., et al., *Electron energy loss-near edge structure as a fingerprint for identifying chromium nitrides.* Solid state communications, 2004. **130**(3-4): p. 209-213.

278. Brydson, R., et al., *EELS as a fingerprint of the chemical co-ordination of light elements.* Microscopy Microanalysis Microstructures, 1991. **2**(2-3): p. 159-169.

279. Sauer, H., et al., *Determination of coordinations and coordination-specific site occupancies by electron energy-loss spectroscopy: An investigation of boron—oxygen compounds.* Ultramicroscopy, 1993. **49**(1-4): p. 198-209.

280. Schmid, H.K., *Phase identification in carbon and BN systems by EELS.* Microscopy Microanalysis Microstructures, 1995. **6**(1): p. 99-111.

281. Brydson, R., et al., *Co-ordination fingerprints in electron loss near-edge structures: Determination of the local site symmetry of aluminium and beryllium in ultrafine minerals.* Journal of the Chemical Society, Chemical Communications, 1989(15): p. 1010-1012.

282. Alamgir, F.M., et al., *The structure of a metallic glass system using EXELFS and EXAFS as complementary probes.* Micron, 2003. **34**(8): p. 433-439.

283. Qian, M., M. Sarikaya, and E.A. Stern, *Development of the EXELFS technique for high accuracy structural information.* Ultramicroscopy, 1995. **59**(1-4): p. 137-147.

284. Tabira, Y., *Local structure around oxygen atoms in CaMgSi2O6 glass by O K-edge EXELFS.* Materials Science and Engineering: B, 1996. **41**(1): p. 63-66.

285. Otten, M.T., et al., *The determination of Ti, Mn and Fe oxidation states in minerals by electron energy-loss spectroscopy.* Ultramicroscopy, 1985. **18**(1-4): p. 285-289.

286. Paterson, J.H. and O.L. Krivanek, *ELNES of 3d transition-metal oxides: II. Variations with oxidation state and crystal structure.* Ultramicroscopy, 1990. **32**(4): p. 319-325.

287. Garvie, L.A., A.J. Craven, and R. Brydson, *Use of electron-energy loss near-edge fine structure in the study of minerals.* American Mineralogist, 1994. **79**(5-6): p. 411-425.

288. Wold, S., K. Esbensen, and P. Geladi, *Principal component analysis.* Chemometrics and intelligent laboratory systems, 1987. **2**(1-3): p. 37-52.

289. Manoubi, T., et al., *Curve fitting methods for quantitative analysis in electron energy loss spectroscopy.* Microscopy Microanalysis Microstructures, 1990. **1**(1): p. 23-39.

290. Verbeeck, J. and S. Van Aert, *Model based quantification of EELS spectra.* Ultramicroscopy, 2004. **101**(2-4): p. 207-224.

291. Wang, F., R.F. Egerton, and M. Malac, *Interpretation of the postpeak in iron fluorides and oxides.* Ultramicroscopy, 2006. **106**(10): p. 925-932.

292. van Aken, P.A. and B. Liebscher, *Quantification of ferrous/ferric ratios in minerals: new evaluation schemes of Fe L 23 electron energy-loss near-edge spectra.* Physics and Chemistry of Minerals, 2002. **29**: p. 188-200.

293. Pearson, D., B. Fultz, and C. Ahn, *Measurements of 3 d state occupancy in transition metals using electron energy loss spectrometry.* Applied physics letters, 1988. **53**(15): p. 1405-1407.

294. Egerton, R., *Improvement of the hydrogenic model to give more accurate values of K-shell ionization cross sections.* Ultramicroscopy, 1996. **63**(1): p. 11-13.

295. Rez, P., *Cross-sections for energy loss spectrometry.* Ultramicroscopy, 1982. **9**(3): p. 283-287.

296. Bethe, H., *Zur theorie des durchgangs schneller korpuskularstrahlen durch materie.* Annalen der Physik, 1930. **397**(3): p. 325-400.

297. Egerton, R., *K-shell ionization cross-sections for use in microanalysis.* Ultramicroscopy, 1979. **4**(2): p. 169-179.

298. Leapman, R., P. Rez, and D. Mayers, *K, L, and M shell generalized oscillator strengths and ionization cross sections for fast electron collisions.* The Journal of chemical physics, 1980. **72**(2): p. 1232-1243.

299. Schmid, H. and W. Mader, *Oxidation states of Mn and Fe in various compound oxide systems.* Micron, 2006. **37**(5): p. 426-432.

300. Varela, M., et al., *Atomic-resolution imaging of oxidation states in manganites.* Physical Review B, 2009. **79**(8): p. 085117.

301. Tan, H., et al., *Oxidation state and chemical shift investigation in transition metal oxides by EELS.* Ultramicroscopy, 2012. **116**: p. 24-33.

302. Hanson, H., et al., *HFS atomic scattering factors.* Acta Crystallographica, 1964. **17**(8): p. 1040-1044.

303. Pines, D., *Elementary excitations in solids*. 2018: CRC Press.

304. Cromer, D.T. and J.T. Waber, *Scattering factors computed from relativistic Dirac–Slater wave functions.* Acta Crystallographica, 1965. **18**(1): p. 104-109.

305. Liberman, D., J. Waber, and D.T. Cromer, *Self-consistent-field Dirac-Slater wave functions for atoms and ions. I. Comparison with previous calculations.* Physical Review, 1965. **137**(1A): p. A27.

306. Leapman, R. and C. Swyt, *Separation of overlapping core edges in electron energy loss spectra by multiple-least-squares fitting.* Ultramicroscopy, 1988. **26**(4): p. 393-403.

307. Shuman, H. and A. Somlyo, *Electron energy loss analysis of near-trace-element concentrations of calcium.* Ultramicroscopy, 1987. **21**(1): p. 23-32.

308. Arenal, R., et al., *Extending the analysis of EELS spectrum-imaging data, from elemental to bond mapping in complex nanostructures.* Ultramicroscopy, 2008. **109**(1): p. 32-38.

309. Mendis, B., M. MacKenzie, and A. Craven, *A new analytical method for characterising the bonding environment at rough interfaces in high-k gate stacks using electron energy loss spectroscopy.* Ultramicroscopy, 2010. **110**(2): p. 105-117.

310. van Aken, P., *Use of Fe L2, 3-edge electron energy-loss spectroscopy to characterize multiple valence states of iron in minerals: a new probe for mineralogical and geochemical research. Ber DMG.* Beih Eur J Mineral, 1995. **7**: p. 255.

311. Van Aken, P., B. Liebscher, and V. Styrsa, *Quantitative determination of iron oxidation states in minerals using Fe L 2, 3-edge electron energy-loss near-edge structure spectroscopy.* Physics and Chemistry of Minerals, 1998. **25**: p. 323-327.

312. Peña, F.d.l., et al., *hyperspy/hyperspy: v1.6.5*. 2021: Zenodo.

313. Leapman, R. and L. Grunes, *Anomalous L 3 L 2 White-Line Ratios in the 3 d Transition Metals.* Physical review letters, 1980. **45**(5): p. 397.

314. Zaluzec, N.J., *An electron energy loss spectral library.* Ultramicroscopy, 1982. **9**(3): p. 319-323.

315. Leapman, R.D., L. Grunes, and P. Fejes, *Study of the L 23 edges in the 3 d transition metals and their oxides by electron-energy-loss spectroscopy with comparisons to theory.* Physical Review B, 1982. **26**(2): p. 614.

316. Sparrow, T., et al., *L3/L2 white-line intensity ratios in the electron energy-loss spectra of 3d transition-metal oxides.* Chemical Physics Letters, 1984. **108**(6): p. 547-550.

317. Van der Laan, G. and I. Kirkman, *The 2p absorption spectra of 3d transition metal compounds in tetrahedral and octahedral symmetry.* Journal of Physics: Condensed Matter, 1992. **4**(16): p. 4189.

318. Waddington, W., et al., *White lines in the L 2, 3 electron-energy-loss and x-ray absorption spectra of 3d transition metals.* Physical Review B, 1986. **34**(3): p. 1467.

319. Qiu, B., et al., *Gas–solid interfacial modification of oxygen activity in layered oxide cathodes for lithium-ion batteries.* Nature communications, 2016. **7**(1): p. 12108.

320. Liu, J., et al., *Rare earth single-atom catalysts for nitrogen and carbon dioxide reduction.* ACS nano, 2020. **14**(1): p. 1093-1101.

321. Chen, J., et al., *Co–Fe–Cr (oxy) hydroxides as efficient oxygen evolution reaction catalysts.* Advanced Energy Materials, 2021. **11**(11): p. 2003412.

322. Wang, J., et al., *Lithium‐and manganese‐rich oxide cathode materials for high‐energy lithium ion batteries.* Advanced Energy Materials, 2016. **6**(21): p. 1600906.

323. Goode, A.E., et al., *Correlative electron and X-ray microscopy: probing chemistry and bonding with high spatial resolution.* Nanoscale, 2015. **7**(5): p. 1534-1548.

324. Sode, J., *Spectroscopy and modelling of catalyst nanoparticles using STEM-EELS*. 2020, University of Oxford.

325. Zezhong Zhang, I.L., Hamish Brown, Daen Jannis, Johan Verbeeck, Sandra Van Aert, Peter Nellist, *Generalised oscillator strength for core-shell electron excitation by fast electrons based on Dirac solutions 1.2 [Data set]* Zenodo, 2023.

326. Kanda, H., et al., *Cluster calculation of oxygen K-edge electron-energy-loss near-edge structure of NiO.* Physical Review B, 1998. **58**(15): p. 9693.

327. De Groot, F., et al., *Oxygen 1s x-ray-absorption edges of transition-metal oxides.* Physical Review B, 1989. **40**(8): p. 5715.

328. Kuiper, P., et al., *Character of holes in Li x Ni 1− x O and their magnetic behavior.* Physical review letters, 1989. **62**(2): p. 221.

329. Pedio, M., et al., *Covalency in oxygen chemisorption as probed by x-ray absorption.* Physical Review B, 1989. **40**(11): p. 7924.

330. Auvergniot, J., et al., *Interface stability of argyrodite Li6PS5Cl toward LiCoO2, LiNi1/3Co1/3Mn1/3O2, and LiMn2O4 in bulk all-solid-state batteries.* Chemistry of Materials, 2017. **29**(9): p. 3883-3890.

331. Walther, F., et al., *Visualization of the interfacial decomposition of composite cathodes in argyrodite-based all-solid-state batteries using time-of-flight secondary-ion mass spectrometry.* Chemistry of materials, 2019. **31**(10): p. 3745-3755.

332. Jung, S.-K., et al., *Understanding the effects of chemical reactions at the cathode–electrolyte interface in sulfide based all-solid-state batteries.* Journal of materials chemistry A, 2019. **7**(40): p. 22967-22976.

333. Luo, K., et al., *Charge-compensation in 3 d-transition-metal-oxide intercalation cathodes through the generation of localized electron holes on oxygen.* Nature chemistry, 2016. **8**(7): p. 684-691.

334. Li, J., et al., *Study of the failure mechanisms of LiNi0. 8Mn0. 1Co0. 1O2 cathode material for lithium ion batteries.* Journal of The Electrochemical Society, 2015. **162**(7): p. A1401.

335. Tan, D.H., et al., *Elucidating reversible electrochemical redox of Li6PS5Cl solid electrolyte.* ACS Energy Letters, 2019. **4**(10): p. 2418-2427.

336. Armstrong, A.R., et al., *Demonstrating oxygen loss and associated structural reorganization in the lithium battery cathode Li [Ni0. 2Li0. 2Mn0. 6] O2.* Journal of the American Chemical Society, 2006. **128**(26): p. 8694-8698.

337. Sharifi‐Asl, S., et al., *Oxygen release degradation in Li‐ion battery cathode materials: mechanisms and mitigating approaches.* Advanced Energy Materials, 2019. **9**(22): p. 1900551.

338. Kobayashi, S., et al., *Atomic-Scale Observations of Oxygen Release Degradation in Sulfide-Based All-Solid-State Batteries with Layered Oxide Cathodes.* ACS Applied Materials & Interfaces, 2022. **14**(34): p. 39459-39466.